

Impact of boronizations on impurity sources and performance in Wendelstein 7-X

Inaugural dissertation

for the attainment of the title of doctor
in the Faculty of Mathematics and Natural Sciences
at the Heinrich Heine University Düsseldorf

presented by
Stepan Sereda
from Ivano-Frankivska

Düsseldorf, May 2021

from the institute for Laser and Plasma Physics
at the Heinrich Heine University Düsseldorf

Published by permission of the
Faculty of Mathematics and Natural Sciences at
Heinrich Heine University Düsseldorf

Supervisor: Prof. Yunfeng Liang
Co-supervisor: Prof. Georg Pretzler

Date of the oral examination: 28.04.2021

Dedicated to my parents Nadiia and Vasyl, who gave me the initial momentum into the world of physics and mathematics.

Acknowledgements

I would like to firstly acknowledge my supervisor Prof. Dr. Yunfeng Liang for giving me possibility to start my journey into the experimental plasma physics as an internship student in Forschungszentrum Jülich what continued as a masters thesis and then this doctoral work. I am also thankful to Prof. Dr. Georg Pretzler for being my second supervisor at the Heinrich-Heine-Universität Düsseldorf and supporting my work.

A very intensive support has been given by Dr. Sebastijan Brezinsek both during the experimental phase at Wendelstein 7-X and the following discussions early mornings in Jülich. I have been given required directions and boosts when it was needed.

Numerous discussions with Dr. Philipp Drews and Dr. Alexander Knieps on organization and numerical questions were extremely useful for my overall progress.

Dr. Erhui Wang, with whom I spent lots of hours in the control room of Wendelstein 7-X and in our laboratory downstairs, directed me and transferred needed knowledge as my scientific advisor.

Dr. Peter Denner, Dr. Thobias Schlummer and Dr. Bernd Schweer put significant time into supporting me with the initial work with the PSI-2 device during my masters thesis phase.

An enormous amount of hours have been spent in the workshop with Dr. Guntram Czymbek, Thomas Krings, Horst Toni Lamberzt and Guruparan Satheeswaran while working with the endoscopes. Before the experimental campaign it took even late nights in the darkness lightened by an Ulbricht sphere and only sounds of rotating filter wheels could be heard.

The strong technical support from Dr. Maciej Krychowiak and Dr. Dirk Rondeshagen has been given in Greifswald. The moral support of Dr. Rondeshagen was of even greater values: "Stepan, work harder - you can do it!" has always been a motivator to keep pushing through emerging obstacles during the research and thesis writing phases.

In addition to the mentioned persons I would also like to acknowledge the Bonn-Cologne Graduate School of Physics and Astronomy for granting me a scholarship as an excellent student for my master studies at the University of Bonn. Forschungszentrum Jülich has also provided excellent conditions for my further work. The EUROfusion funding made possible my long stay at Wendelstein 7-X for the complete experimental campaign OP1.2b and additional visits.

I am also thankful to Prof. Dr. Volodymyr Kapustianyk, who supervised my early research work at the Ivan Franko University of Lviv.

Lastly, this wouldn't be possible without encouragement of my way into science and giving me opportunity to study at the Lviv Physics and Mathematics Lyceum.

Abstract

The Wendelstein 7-X (W7-X) stellarator has recently successfully completed its experimental campaign with the passively cooled test divertor unit (TDU) made of graphite. TDU is the plasma facing component where the most intensive plasma-surface interactions take place in a controlled manner and it provides particle and heat exhaust. In addition to TDU the plasma vessel also consisted of other elements made of carbon and the stainless steel wall. Still impurity influx into the plasma due to the plasma-surface interactions is unavoidable. In addition the recessed areas can be also sources of impurities. Specifically, the low-Z oxygen and carbon were the main plasma impurities at W7-X.

To tackle this issue boronization was applied – plasma-chemical in-situ deposition of amorphous boron-containing hydrogen films on all plasma-facing components in a helium glow discharge with 10% B₂H₆ [1]. The application of boronization has led to one of the main achievements of the campaign: plasma operation at high core densities of more than 10^{20} m^{-3} due to the reduced radiation-induced density limit. This work mainly focuses on full characterization of the change of impurity influx at TDU, the corresponding effects of boronization on the performance of W7-X and the underlying mechanism.

Photon influx spectroscopy of line emission of the atoms and ions of carbon, oxygen, boron and hydrogen allowed to deduce normalized (divided by hydrogen flux) influx of oxygen, carbon and boron. Those measurements were conducted with the overview spectrometer system during the complete experimental campaign. The photon emission spectroscopy data was supported by a number of other diagnostics provided at W7-X.

In total three boronizations were applied during the second part of the TDU campaign. After the first boronization the oxygen to hydrogen flux ratio (normalized influx of oxygen) at the divertor substantially decreased by a factor of 10 and the carbon to hydrogen flux ratio (normalized influx of carbon) decreased by a factor of 4 as obtained from spectroscopy. In the same time, boron emission appeared in the spectra. Between the boronizations oxygen and carbon normalized influxes increased but never reached the pre-boronization values. With each subsequent boronization the oxygen level decreased even more, reaching the lowest values after the third boronization which were more than a factor of 100 lower than before the first boronization and the boron level was increasing simultaneously.

Such a decrease in low-Z impurity concentration significantly extended the operation window of W7-X in terms of line-integrated electron density (from $4 \cdot 10^{19} \text{ m}^{-2}$ to more than $1 \cdot 10^{20} \text{ m}^{-2}$) and diamagnetic energy (from 330 kJ up to 510 kJ). Z_{eff} decreased from 4.5 down to values close to 1.2 as obtained from bremsstrahlung measurements. The above mentioned changes in the line-integrated electron density, diamagnetic energy and Z_{eff} are given for the two reference discharges before and after boronization. Plasma conditions did not significantly deteriorate between boronizations allowing device operation without glow-discharge cleaning.

The decrease in impurity influx can be explained in terms of effective oxygen gettering by boron in the remote plasma-facing components of W7-X, while at the strike line area it is quickly eroded. Not only the freshly available boron plays an important role in this processes, but also redeposited layers provide newly available boron atoms.

This thesis demonstrates boronization effects on the high performance of W7-X and answers question about the underlying mechanisms. These findings are discussed in the view of the future steady-state experimental campaign of W7-X, when steady-state discharges of up-to 30 min duration are planned.

Table of Contents

Abstract	i
List of publications	v
List of Figures	vii
List of Tables	xiii
1 Introduction	1
1.1 Magnetic confinement fusion: tokamaks and stellarators	1
1.2 Particle and energy exhaust: divertor	4
1.3 Wendelstein 7-X stellarator	6
1.4 Plasma-surface interactions	9
1.5 Low-Z oxygen and carbon impurities	12
1.6 Wall conditioning in fusion devices	14
1.7 Boronization	16
1.8 This thesis	21
2 Edge and divertor diagnostics for impurity characterization at Wendelstein 7-X	23
2.1 Endoscope system at Wendelstein 7-X	23
2.1.1 Optical layout	25
2.1.2 Detector system	30
2.1.3 Endoscope image correction and resolution	35
2.1.4 UV-VIS-NIR overview spectroscopy	39
2.1.5 Endoscope calibration	41
2.2 Edge particle and photon flux measurements	44
2.2.1 Divertor Langmuir probes	44
2.2.2 Midplane multipurpose manipulator	46
2.2.3 Filterscopes	47
2.3 Core impurity measurements	48
2.3.1 HEXOS	48
2.3.2 Bolometry	49
2.3.3 Dispersion interferometry	50
3 Spectroscopy at the divertor region of Wendelstein 7-X	53
3.1 Photon influx spectroscopy	53
3.2 Helium-beam emission spectroscopy	55
3.3 Identified spectra	60
3.4 2D tomographic reconstruction of emission profiles	65

TABLE OF CONTENTS

4	Wall conditioning at Wendelstein 7-X equipped with the passively cooled divertor	71
4.1	Baking	73
4.2	Glow discharge cleaning	74
4.3	Electron cyclotron wall conditioning	76
4.4	Boronization set-up	77
4.5	Strategy to assess boronization at Wendelstein 7-X	78
5	Effects of boronization	83
5.1	Electron temperature and density profiles	83
5.2	Radiation of the low-Z impurities: carbon and oxygen	85
5.3	Power loads on the divertor	87
5.4	Morphology and chemical composition of the divertor surface	89
5.5	Difference of short and long-term boronizations effects	91
6	Summary, conclusions and outlook	97
	References	99

List of publications

1. The author of this thesis is also the corresponding author of the following article. This work is the main result of the research and was adapted mainly for Chapter 5 of this thesis. The author was responsible for impurity influx characterization at the divertor target of W7-X with the help of photon influx spectroscopy. The corresponding experimental set-up (the overview spectrometer system) was prepared and exploited during the experimental campaign OP1.2b by the author. Additional diagnostic data was used for analysis provided by the corresponding responsible scientists.
S. Sereda, S. Brezinsek, E. Wang, T. Barbui, R. Brakel, B. Buttenschön, A. Gorjaev, U. Hergenbahn, U. Höfel, M. Jakubowski, A. Knieps, R. König, M. Krychowiak, S. Kwak, Y. Liang, D. Naujoks, A. Pavone, M. Rasinski, L. Rudischhauser, M. Ślęczka, J. Svensson, H. Viebke, T. Wauters, Y. Wei, V. Winters, D. Zhang, and the W7-X team. “Impact of Boronizations on Impurity Sources and Performance in Wendelstein 7-X”. In: *Nuclear Fusion* 60.8 (2020), p. 086007. ISSN: 0029-5515, 1741-4326. DOI: 10.1088/1741-4326/ab937b
2. The author of this thesis provided spatial resolution test for the article, though in this thesis a more sophisticated results are presented by the author.
O. Neubauer, A. Charl, G. Czymek, Y. Gao, M. Knaup, R. König, M. Krychowiak, H.-T. Lambertz, M. Lennartz, C. Linsmeier, G. Satheeswaran, B. Schweer, M. Schülke, and S. Sereda. “Endoscopes for Observation of Plasma-Wall Interactions in the Divertor of Wendelstein 7-X”. In: *Fusion Engineering and Design* 146 (2019), pp. 19–22. ISSN: 09203796. DOI: 10.1016/j.fusengdes.2018.11.009
3. The author of this thesis provided data from the overview spectrometer system.
E. Wang, S. Brezinsek, S. Sereda, B. Buttenschön, T. Barbui, C. P. Dhard, M. Endler, O. Ford, E. Flom, K. C. Hammond, M. Jakubowski, M. Krychowiak, P. Kornejew, R. König, Y. Liang, M. Mayer, D. Naujoks, O. Neubauer, J. Oelmann, M. Rasinski, V. R. Winters, A. Gorjaev, T. Wauters, Y. Wei, D. Zhang, and The W7-X team. “Impurity Sources and Fluxes in W7-X: From the Plasma-Facing Components to the Edge Layer”. In: *Physica Scripta* T171 (2020), p. 014040. ISSN: 0031-8949, 1402-4896. DOI: 10.1088/1402-4896/ab4c04
4. The author of this thesis participated in development and calibration of the first version of the overview spectrometer system before the research conducted in the frame of this thesis.
Y. Wei, E. Wang, Y. Liang, S. Brezinsek, B. Schweer, M. Krychowiak, O. Neubauer, R. König, S. Sereda, Ch. Linsmeier, and W7-X Team. “An Ultraviolet-Visible-near Infrared Overview Spectroscopy for Divertor Plasma Diagnosis on Wendelstein 7-X”. In: *AIP Advances* 8.8 (2018), p. 085011. ISSN: 2158-3226. DOI: 10.1063/1.5033371

List of Figures

1.1	Deuterium-tritium fusion reaction.	1
1.2	Tokamak field (taken from [11]). \vec{B}_t , \vec{B}_p , $\vec{B}_t + \vec{B}_p$ - toroidal, poloidal and the resulting helical magnetic field; I_p - plasma current.	3
1.3	Poloidal divertor concept for a tokamak: a) Plasma cross section in a tokamak with a poloidal divertor; b) A close-up look at the divertor target region.	5
1.4	Schematic view of the Wendelstein 7-X stellarator (taken from [13]). A set of 4 nested magnetic flux surfaces is shown inside the magnetic field coils. The magnetic field lines shown correspond to the green surface. Planar magnetic coils are shown in brown, non-planar coils in grey and trim coils in yellow.	7
1.5	Schematic view of the ECRH system at Wendelstein 7-X stellarator (taken from [18]). 5 out of 10 gyrotrons are shown in module 1 of W7-X. P1 and P2 are the polarizers; SBS and MBS stand for single-beam and multi-beam sections; M5-M11 - multibeam mirrors.	8
1.6	Physical sputtering yield of D for different materials of the surface (Be, C and W) as function of the projectile impact energy E_0 . The scale bar in the right corner shows that the uncertainty can reach up to a factor of 2 depending on the surface roughness and other parameters (taken from [19]).	10
1.7	Chemical yield Y_{chemical} of C by H for different energies of the impinging H^+ ion: methane only (upper part) and the total value including higher carbohydrates (bottom part), (taken from [21]).	11
1.8	Plasma-surface interactions. In addition to the main processes of our interest - physical and chemical sputtering, a number of other processes are present in fusion devices (inspired by a talk by Dr. S. Brezinsek).	12
1.9	Radiation loss function R for low-Z C and O which were the main impurities in W7-X. In addition Fe and W are also shown, but their radiation was not a problem for W7-X, since no W materials were in the plasma vessel and the stainless steel walls did not cause Fe influx in the plasma (taken from [19]).	13
1.10	Scheme of the oxygen recycling in W7-X (modified [22]).	14
1.11	Reaction yield of CO formation for different materials during 3 keV O^+ bombardment. The oxygen flux was at the order of 10^{18} m^{-2} for all cases. The most relevant materials are EK98 (graphite) and a-C/B:H, which show difference in the CO yield of more than 10 times (taken from [36]).	18
1.12	Thermal desorption spectra of CO and CO_2 molecules for different materials, with the most important graphite EK98 and the a-C/B:H layer. The energy of the O^+ ion was 3 keV and the oxygen fluence $1 \cdot 10^{21} \text{ m}^{-2}$ (taken from [36]).	19

LIST OF FIGURES

1.13	XPS spectra of the 1s core level of B for different samples and conditions. II stands for B flushing, III for boronization - in both cases graphite sample was considered. Al-target shows the case of an aluminium sample after boronization. The bottom part shows spectra for the graphite sample after boronization without exposure to plasma (taken from [37]).	20
2.1	Edge diagnostics to study synergy between the 3D edge topology and the PSI processes on W7-X (taken from [38]). The right top corner shows the 3 poloidal cross-section where the endoscope system (green and blue) and MPM (red) are located. The connection of the diagnostics is shown with a magnetic field line (magenta) starting at the MPM position for the standard magnetic configuration of W7-X.	24
2.2	Endoscope location scheme.	25
2.3	Poincaré maps of the 4 main magnetic configuration of W7-X used in OP1.2b: a)standard; b)high-mirror; c)low- ι ; d)high- ι . LCFS is denoted in red, while magnetic flux surfaces of the main plasma and the islands are shown in blue. The black lines correspond to the solid surfaces.	27
2.4	Connection length L_c of the 4 main magnetic configuration of W7-X: a)standard; b)high-mirror; c)low- ι ; d)high- ι ; e)colorbar for the (a-d) plots.	28
2.5	CAD scheme of the endoscope (taken from [41]).	29
2.6	Optical scheme of the J endoscope obtained with the ZEMAX software package.	30
2.7	Detector box of the endoscope. 1.1, 2.1 - dichroic beam splitters deflecting the UV range; 1.2, 2.2 - dichroic beam splitters deflecting the Vis range; 1.a, 1.b, 2.a, 2.b - intensity beam splitters; UV 1.a.1, UV 2.a.1, VIS 1.b.1, VIS 1.b.2, VIS 2.b.1 - CCD cameras in the corresponding wavelength ranges; IR2 - the IR camera; UV 1.a.2, IR1, UV 2.a.2, VIS 2.b.2 - fibre bundles for spectroscopy in the corresponding wavelength range (taken from [41] and modified). UV: [350 - 550] nm, VIS: [550 - 950] nm, IR: [950 - 7000] nm.	31
2.8	MCP scheme (taken from [43]).	32
2.9	Measured gain of the image intensifiers at the cameras UV 1.a.1 and UV 2.a.1 (as shown in Figure 2.7).	33
2.10	Schematic view of the filter camera module (FCM). The 2 filter wheels are shown in blue. The other important elements are denoted in the figure [produced by A. Charl].	34
2.11	Usage of the OpenCV library to correct image distortions: a) The uncorrected chess-board pattern together with the identified black squares intersections (in color); b) The corrected image.	36
2.12	Illustration of the slanted-edge method of MTF calculation.	38
2.13	Values of the MTF function of the AEJ51 endoscope for the visible camera (VIS 2.b.1) without interference filters (polychromatic). The results of Zemax calculation are shown for the point in the center of the image in the wavelength range from 350 nm to 550 nm for both sagittal and tangential components. The values obtained with <i>MTF Mapper</i> were chosen from the location on the image close to the optical axis and are shown for both sagittal and tangential components. The values obtained with the slit approach are shown too.	39

2.14	Desktop mount of 5 Avantes AVASPEC-ULC2048L-USB2-RM spectrometers with the power supply and the USB2 hub. Arrows point at the 5 SMA connectors for each channel (spectrometer). 5 free slots could be used for additional spectrometers.	40
2.15	Field of view of the overview spectrometer (green) for the standard magnetic configuration of W7-X. The strike-line location is shown only for the magnetic island in the field of view (red, “vacuum” case). The Poincaré map is depicted in blue. Positions of the TDU Langmuir probes are shown in yellow dots. Horizontal and vertical divertor target plates are shown in grey [2].	41
2.16	Setup of the endoscope for radiometric calibration in the Torus hall of W7-X. The AEJ endoscope can be seen on the left. The complete optical path (including the optical fibers leading to the laboratory) were completely the same as during the experiment. The Ulbricht sphere can be seen on the right and its opening is located in the focal plane of the endoscope.	42
2.17	$s(\lambda_0)$ - spectral response of the AEJ51 endoscope for all cameras and all narrow band interference filters mounted during OP1.2b of W7-X.	43
2.18	TDU probe system at W7-X: a)Image from an infrared camera showing the 3rd and the 4th finger of the horizontal part of TDU where the probes are located. The strike lines are shown in orange; b)Photo of the TDU fingers with the probe tips (taken from [53] and [54]).	45
2.19	Location of the multi-purpose manipulator (MPM) with the combined probe (left). Top view of the combined probe with all the pins numbered. Number of the Langmuir pins are P2 and P4 (modified [55]).	46
2.20	Field of view of the filterscope system and the corresponding Poincaré plots for the standard magnetic configuration (taken from [60]).	47
2.21	Field of view of the HEXOS VUV spectrometer used for the higher ionization stages of the impurities studies (taken from [63]).	49
2.22	Field of view of the bolometry system (taken from [64]). Horizontal bolometer camera (HBC) - left, vertical bolometer camera (VBC) - right.	50
2.23	Dispersion interferometer scheme (taken from [66]).	51
3.1	Scan of the ratios of the S/XB coefficients around $\langle T_e \rangle = 75$ eV and $\langle n_e \rangle = 7.6 \cdot 10^{18} \text{ m}^{-3}$: a)BII/ H_γ , b)CII/ H_γ , c)OI/ H_γ	55
3.2	He levels for $n \in [1 - 4]$ together with the 3 transitions used in He-BES.	57
3.3	Emissivity ratios calculated with the updated version of the CR model in the work of Zholobenko et al. The results are shown for the not metastable resolved case. The solid line corresponds to R_{T_e} and the dashed line to R_{n_e} . The red mark illustrates result of minimization of 3.14 and the corresponding values of T_e and n_e (taken from [69]).	58
3.4	Comparison of the artificial camera image of a simultaneous helium puff from the all 5 divertor nozzles in the M51 module of W7-X with the measured helium puff during the 20181010.021 discharge of W7-X.	59
3.5	Emission spectra of different ionization stages of N together with the expected ranges of the molecular bands. The spectra were obtained with the overview spectrometer for the 20180920.050 discharge of W7-X in the standard magnetic configuration. N_2 was injected from the divertor nozzles (number 4 and 2) in the M51 module. The spectra without N_2 puffing was subtracted from the one during puffing to obtain only the lines and bands of interest.	60

LIST OF FIGURES

3.6	Emission spectra of Ne obtained with the overview spectrometer for the 20180920.040 discharge of W7-X. Ne was injected from the divertor nozzles in the M51 module. The spectra without Ne puffing was subtracted from the one during puffing to obtain only the Ne lines.	62
3.7	Emission spectra of C obtained with the overview spectrometer for the 20180920.013 discharge of W7-X. CH ₄ was injected from the divertor nozzles in the M51 module. The spectra without methane puffing was subtracted from the one during puffing to obtain only the C lines.	63
3.8	Emission spectra of He, H and O obtained with the overview spectrometer for the 20180801.022 and 20181010.022 discharges of W7-X. The He spectrum (black part) was obtained by injection from the divertor nozzles in the M51 module. The spectra without He puffing was subtracted from the one during puffing to obtain only the He lines. The complete spectrum for 20180801.022 was added afterwards.	64
3.9	Main basics of the tomographic reconstruction: a) Brightness of the image pixels \mathbf{I} as product of the transfer matrix \mathbf{T} and the emissivity profile \mathbf{g} , view in the toroidal cross section, b) Additional fields of view due to the rotation of the first mirror of the J and L 51 endoscopes, poloidal cross section view.	66
3.10	Test emission profile as a sum of 2 Gaussian distributions with the centers at the O-points of the magnetic islands in the standard magnetic configuration in the M51 module of W7-X (further adoption of [77]).	68
3.11	a) Fields of view of 2 endoscopes in the M51 module of W7-X for 5 different positions of the first mirror (J - green, L - cyan); b) Result of reconstruction with 2 endoscopes in the module M51; c) Fields of view of 4 endoscopes in the M30 module of W7-X (J - blue, L - red) and in the module M51 for 5 different positions of the first mirror; d) Result of reconstruction with 4 endoscopes in the modules M30 and M51 (further adoption of [77]).	69
3.12	Simulated emissivity of He being injected with 1 (top left) and 4 (bottom left) nozzles at the divertor target in the module M51 of W7-X. The results of reconstruction are shown to the right of the corresponding initial profiles.	70
4.1	Temperature of the divertor module 1v of the upper divertor target M51 of W7-X (left axis) and partial pressure of CO, CO ₂ and H ₂ O (right axis) on the last day before boronization 20180801 (Sereda et al. [2]).	72
4.2	Description of the target modules naming convention. The thermocouples used in this work were located in the module TM1v. Figure produced by Marco Krause.	73
4.3	Quadrupole mass spectra of the Wendelstein 7-X plasma vessel outgassing before and after baking in both test divertor units campaigns of Wendelstein 7-X OP1.2a (2017) and OP1.2b (2018). The mass to charge ratio constitutes the x-axis and the spectra signal is given in arbitrary units (taken from [79]).	74
4.4	QMS spectrometry of the cumulative H ₂ -GDC during OP1.2a of W7-X. The red dashed lines correspond to the days with ECRH operation. The black dashed lines show the time envelopes. m16 - CH ₄ , m18 - H ₂ O, m28 - CO, m40 - Ar and m44 - CO ₂ (taken from [81]).	75

4.5	QMS spectrometry of the ECWC discharge in hydrogen (20160209.004, left) and the ECWC in helium (20160209.005, right) with a 'train' of plasma pulses during OP1.1 of W7-X. The red dashed lines correspond to the days with ECWC operation. The black dashed lines show the time envelopes. m2 - H ₂ , m4 - He, m16 - CH ₄ , m28 - CO and m44 - CO ₂ (taken from [84]).	76
4.6	Scheme of the boronization set-up during OP1.2b of W7-X.	77
4.7	Plasma-facing components of W7-X (Sereda et al. [2]).	79
4.8	Strategy for the first boronization assessment: (a) - impurity levels and composition, (b) - radiation induced density limit.	79
4.9	Heat flux distributions for the main magnetic configurations on the divertor targets of W7-X, as calculated for the "vacuum" case (Sereda et al. [2]).	80
5.1	T _e and n _e edge profiles measured with the combined probe mounted on the multi-purpose manipulator. The data was available for the standard magnetic configuration in OP1.2a (20171026.027, P _{ECRH} = 1.8 MW) as a reference for the pre-boronization conditions and OP1.2b (20180807.017, P _{ECRH} = 2.5 MW) for the post-boronization characterization.	84
5.2	n _e profiles obtained with the Thomson scattering diagnostic for the reference discharges (left). Core values of n _e as function of the line integrated n _e divided by the integration length for the reference discharges before and after the first boronization (right).	85
5.3	Emission spectra measured at the divertor before (red, discharge 20180801.021) and after (green, discharge 20180807.011) the first boronization of W7-X a) in the range of 350 nm – 1000 nm and b) in the vicinity of CII, BII and OI lines (Sereda et al. [2]).	85
5.4	Emission spectra in the range 2.6 – 160 nm obtained with HEXOS before (red dashed) and after (green) the first boronization (Sereda et al. [2]).	86
5.5	Normalized influx of low-Z O and C together with introduced B. Two discharges are shown on the plot: 20180801.036 before the first boronization (red background) and 20180807.013 after (green background) (Sereda et al. [2]).	87
5.6	Diamagnetic energy, Z _{eff} and radiation fraction of the plasma f _{rad} as a function of the line integrated electron density before boronization (red, 20180807.013) and after (green, 20180801.036) boronization (Sereda et al. [2]).	87
5.7	Power loads on the divertor P _{div} before (20180808.021, top image) and after (20180807.011, middle image) boronization. The plot of P _{div} on the bottom figure is along the axis shown in magenta in the upper two images.	88
5.8	Heuristic explanation of the new detachment mechanism after boronization. For the details please follow the text (taken from [88]).	89
5.9	a) Scanning electron microscope (SEM) image of a re-deposition zone on the TM2h6 A008 element of the divertor (its location is shown in orange in Figure 2.15), blue line is the axis of the EDX scan. The red dashed line corresponds to the interface between preceding and the last experimental phases; b) Concentration profiles of carbon, oxygen, boron and iron (Sereda et al. [2]).	90

LIST OF FIGURES

5.10	Boronization mechanism. The coating a-B/C:H layer is shown in yellow. Oxygen gettered due to the boronization is shown in red, while the blue color shows oxygen gettered due to re-deposition.	91
5.11	a) B and C normalized influx as a function of a discharge number on the first day after boronization. b) Ratio of C to B fluxes for the same operational day of W7-X. Standard magnetic configuration (Sereda et al. [2]).	92
5.12	Time evolution of the main low Z impurities O and C as well as B: a) normalized influx, b) intensity of OVI, CVI and BV lines normalized to the line integrated density. The values are plotted as a function of the total plasma exposure time in all magnetic configurations normalized by the values before boronization. The vertical blue lines show boronization occurrences (Sereda et al. [2]).	93
5.13	Time evolution of CIII (465.4 nm) and OII (441.9 nm) photon flux obtained with the filterscope system normalized to the values before boronization as a function of total plasma exposure time (Sereda et al. [2]).	94
5.14	Mass spectrometry results for CO and CO ₂ before (20180808.021, higher values) and after the first (20180807.011, lower values) boronization (Sereda et al. [2]).	94
5.15	Field of view of the used line of sight of the filterscope system at: a) AEK10 port (toroidal angle $\phi = [-4.8^\circ, -10.1^\circ]$) looking at the carbon shield and at b) AEL30 port ($\phi = [126.5^\circ, 130.8^\circ]$) looking at the stainless steel wall (Sereda et al. [2]).	95

List of Tables

1.1	Main parameters of W7-X during the divertor campaign OP1.2. * - at 2 MW heating power [16].	7
2.1	Relevant properties of the image intensifiers used.	32
2.2	List of the interference filters installed on the AEJ51 endoscope during the experimental phase OP1.2b. λ_{CW} - central wavelength, FWHM - full width at half maximum.	34
2.3	Position of the interference filters installed on the AEJ51 endoscope during the experimental phase OP1.2b in the corresponding filter wheels. Numbers after lines are λ_{CW} in [nm]	35
3.1	List of the identified N lines in the H plasma of W7-X in OP1.2b during a N injection.	61
3.2	List of the identified Ne in the H plasma of Wendelstein 7-X in OP1.2b during a Ne injection.	62
3.3	List of the identified intrinsic lines in the H plasma of W7-X in OP1.2b before boronization.	64
4.1	Statistics of the GDC usage in the experimental phases OP1.2a and OP1.2b. * - the GDC duration before boronization application, after its application the values are negligible [79].	72
4.2	List proving the date, the duration and the used amount of the diborane gas for each boronization during OP1.2b of W7-X. Nl stands for normal liter.	78
4.3	Statistics of the plasma exposure time for the OP1.2b experimental campaign of W7-X, 'f' corresponds to forward and 'r' to reversed magnetic configurations (Sereda et al. [2]).	80
4.4	List of the discharges used for long-time characterization of the influence of the boronizations on the performance of W7-X. * - for the TDU data a similar discharge 20171207.013 was used.	81

1

Introduction

1.1 Magnetic confinement fusion: tokamaks and stellarators

The thermonuclear fusion is a prospective source of energy for the future. The most promising concept is the magnetic confinement thermonuclear fusion in which the hot plasma is contained with the help of magnetic field. At the moment the most advanced experiment is the ITER tokamak, which is supposed to start deuterium-tritium (DT) operation in 2035. It's most important goals are [6]:

1. Demonstrate significant fusion power production $P_{\text{fus}} \approx 500$ MW for ≈ 7 minutes.
2. This fusion power should be produced while the plasma heating is mainly provided by α -particles.

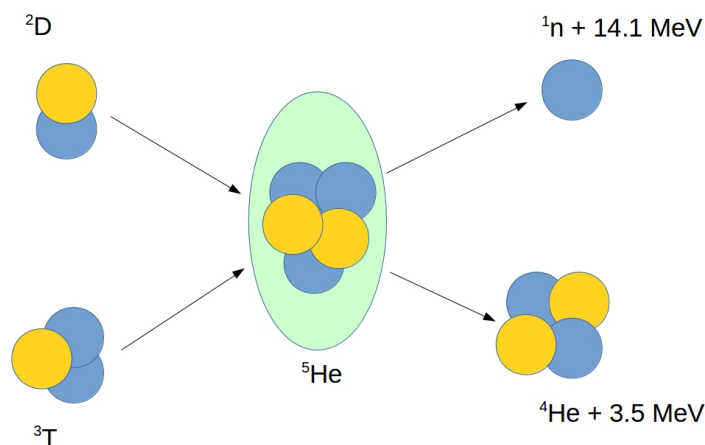


Figure 1.1: Deuterium-tritium fusion reaction.

After the successful achievement of ITER's goals the next step is the development of the DEMO test reactor. This machine is supposed to be mostly based on the

1. Introduction

technical achievements of ITER. Its most important goal is to demonstrate net electricity production of [300 - 500] MW [6].

In ITERs case it is important to demonstrate plasma ignition for the case of DT fusion - the α particles are fully compensating the power losses from the plasma (see Figure 1.1 for the reaction). This requirement leads to the so-called triple product condition (or Lawson criteria [7]):

$$n_{DT}k_B T_i \tau_E > 3 \cdot 10^{21} \text{ keV} \cdot \text{s} \cdot \text{m}^{-3} \quad (1.1)$$

where: n_{DT} - density of the DT fuel (ion density), k_B - Boltzmann constant, T_i - ion temperature, τ_E - global energy confinement time. τ_E is defined as $\frac{E_{plasma}}{P_{heat}}$ with E_{plasma} - kinetic energy of the plasma and P_{heat} - heating power absorbed in the plasma. Such a condition would require $T_i \approx [10 - 20]$ keV, $n_{DT} \approx 10^{20} \text{ m}^{-3}$ and τ_E of a couple of seconds.

From Equation 1.1 it is clear that the ion temperature and the fuel density are very important parameters. Therefore, it is important to prevent presence of impurities in the plasma, which causes fuel dilution. In case of the presence of the impurity with the atomic number Z and density n_z the fuel density becomes:

$$n_{DT} = n_e - \sum Z n_z \quad (1.2)$$

In addition, the impurities radiate plasma energy causing its cooling. Therefore, avoiding impurities in the core plasma is one of the most important challenges in the field of fusion and is discussed in detail in the corresponding chapter.

Another important basic characteristic is the energy amplification factor:

$$Q = \frac{P_{fus}}{P_{ext}}, \quad (1.3)$$

which is the ratio between the fusion power P_{fus} and the external heating P_{ext} . Taking into account that in the future fusion power plants part of the produced electricity will be used for plasma heating, the net produced electricity $P_{el,net}$ can be written as [6]:

$$P_{el,net} \sim \eta_{el} P_{therm} - \frac{P_{ext}}{\eta_{ext}} \sim P_{therm} \left(\eta_{el} - \frac{1}{\eta_{ext} Q} \right) \quad (1.4)$$

where η_{el} is the efficiency of heat to electricity production and η_{ext} is the efficiency of the plasma heating. A net electricity production become possible when $Q > 10$ - the so-called 'break-even' condition. For DEMO this value must be much higher $Q \gg 10$.

Recently to the above mentioned approach in ITER for demonstrating plasma burning conditions a new one has been added. It has been proposed by the MIT Plasma Science and Fusion Center in cooperation with Commonwealth Fusion Systems to exploit the recent developments in the high temperature superconductors to significantly accelerate demonstration of $Q > 1$ [8]. It was proposed to build a mid-size tokamak with $B_0 = 12.2$ T (magnetic field on axis) in contrast to $B_0 \approx 5.8$ T in ITER. Such an increase in magnetic field would be possible by production of the toroidal magnetic field coils made of rare earth barium copper oxide (REBCO), while ITERs coils used an older low temperature superconductor material (Nb_3Sn). A successful demonstration of $Q = 2$ (the very conservative estimate) with up to $Q = 11$ would push the situation towards development of the first demonstration fusion power plant ARC, providing strong arguments for commercialization of fusion power production.

The SPARC (Soonest/Smallest Private-Funded Affordable Robust Compact) tokamak will have $R_0 = 1.85$ m, $a = 0.57$ m, $\langle n_e \rangle = 3 \cdot 10^{20} \text{ m}^{-3}$, $\langle T_e \rangle = 7$ keV and being able to produce H-mode (the high confinement mode) discharges with DT plasma burning conditions for 10 s at the flat top part of the discharge. The high values of $P_{\text{fusion}} = 140$ MW [9] will produce significant power loads on the divertor targets, with heat fluxes $P_{\text{div}} \approx 250 \frac{\text{MW}}{\text{m}^2}$. Although the final material has not been selected yet, 2 options are considered: carbon and tungsten [10].

In both cases the extremely high values of P_{div} together with the importance of keeping the low concentration of the impurities in the main plasma are putting PSI processes and wall conditioning in the highest priority. It is planned to apply boronization at SPARC as one of the tools for low impurity content in the main plasma. In addition, a suitable set of diagnostic tools will be required for the PSI studies and plasma conditions control. Both questions are studied in this work for the case of the Wendelstein 7-X (W7-X) stellarator and their importance is once again highlighted in the view of introduction of the SPARC tokamak.

The most promising concept for fusion is magnetic confinement fusion. Specifically, toroidal magnetic confinement system of the tokamak type has been selected for ITER design. In this approach toroidal magnetic field (\vec{B}_t) is created with a set of toroidal magnetic field coils. Just a toroidal field is not sufficient to confine plasma because the inhomogeneity of the magnetic field would cause lose of the particles via drifts.

To counteract this problem a poloidal field component (\vec{B}_p) can be added resulting in a helical field $\vec{B}_t + \vec{B}_p$ (see Figure 1.2). In a tokamak \vec{B}_p is created by induction of plasma current I_p . The central solenoid is used as the primary winding and the plasma itself as a secondary winding of a transformer. In addition, poloidal field coils are used to generate magnetic field which together with I_p generates radially inward $\vec{j} \times \vec{B}$ force to cancel the radially outward forces [6].

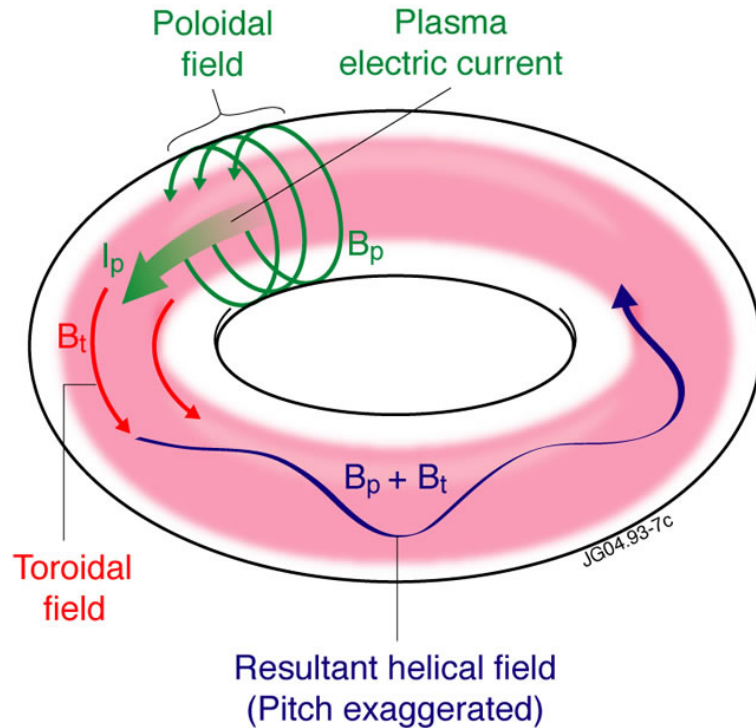


Figure 1.2: Tokamak field (taken from [11]). \vec{B}_t , \vec{B}_p , $\vec{B}_t + \vec{B}_p$ - toroidal, poloidal and the resulting helical magnetic field; I_p - plasma current.

1. Introduction

In general, two basic parameters are used in tokamaks and stellarators (see subsection 1.3) to describe rotational transform of magnetic field lines. In a case of tokamak it is called *safety factor* q , which is a toroidal angle the magnetic field line has to rotate to make one full rotation in poloidal angle and is defined as:

$$q = \frac{\Delta\phi}{2\pi} \quad (1.5)$$

For stellarators the corresponding parameter is called *rotational transform* ι , which is angle of poloidal rotation of the magnetic field line after one toroidal rotation. The relation between q and ι is:

$$\iota = \frac{2\pi}{q} \quad (1.6)$$

Most of the magnetic field lines do not close-up on themselves, but form a complete toroidal surface - *magnetic flux surface*. That means that

$$q = \frac{m}{n}, \quad (1.7)$$

where m and n are the numbers of toroidal and poloidal rotations when the magnetic field line closes on itself if q is rational. In this case the surface is called rational magnetic flux surface. If q is irrational then the magnetic flux surface is called irrational. All these surfaces are forming a set of nested magnetic flux surfaces with different q value. Plasma pressure and current density for tokamaks is constant on the same magnetic flux surfaces.

The field lines which do not cross the wall elements are called *closed magnetic field lines*. The outermost magnetic flux surface formed by a closed magnetic field line is called *last closed magnetic flux* (LCMF) surface or LCFS (*last closed flux surface*). In general the magnetic field lines outside of LCFS are called *open magnetic field lines* and cross the wall.

In a tokamak the inboard side of the toroid is characterized by a higher magnetic field due to the higher density of the toroidal magnetic field coils and, therefore, is called *high field side* (HFS). The outer side is correspondingly called *low field side* (LFS). These terms are also applied to a stellarator.

1.2 Particle and energy exhaust: divertor

Even though the plasma is magnetically confined it's impossible to completely avoid PSI processes. In addition, plasma particle and energy exhaust must be managed too. To provide such a function a specific configuration of the magnetic field at the edge together with special wall areas are used.

One of the most advanced approaches is the poloidal divertor concept. In this case the magnetic field at the edge is diverted with a help of external divertor coils and short cut the open magnetic field lines to the specific wall elements - divertor targets. The divertor targets can be located in a remote area from the main plasma reducing transport of the impurities from the PSI zone into the main plasma (see Figure 1.3.a). LCFS passes through the X-point, where $B_\theta = 0$. Due to the cross-field transport of particles and energy there is also so called private plasma region outside of separatrix and below the X-point.

As is shown in Figures 1.3.a and 1.3.b particles from the main plasma cross LCFS and then are rapidly transported along the open magnetic field lines to the divertor

targets, which constitute plasma sink action. This layer outside of LCFS where the rapid transport takes place is called the scrape-off layer (SOL). The sink action is caused by sticking of the charged particles to the solid surface. Those particles then recombine at the surface and are released back into the plasma as neutrals. Therefore, the divertor targets act as particle source if there is no external fuelling. The released neutrals are again ionized and transported back to the divertor targets resulting in the recycling process.

The plasma transport inside LCFS is radially outward and described as [12]:

$$\Gamma_{\perp} = -D_{\perp} \frac{dn}{dr} - v_{\text{pinch}} n \quad (1.8)$$

where: Γ_{\perp} - particle flux density, D_{\perp} - cross field transport coefficient, v_{pinch} - outward drift velocity and n - density. Once the particles cross LCFS they are quickly transported to the divertor targets with the plasma flow speed $v = c_s = \sqrt{\frac{k(T_i + T_e)}{m_i}}$. The resulting force acting on the plasma is the pressure gradient force F :

$$F = -\frac{d(p_e + p_i)}{dx} \quad (1.9)$$

As a result most of the PSI processes are happening at the divertor target in the area called strike line.

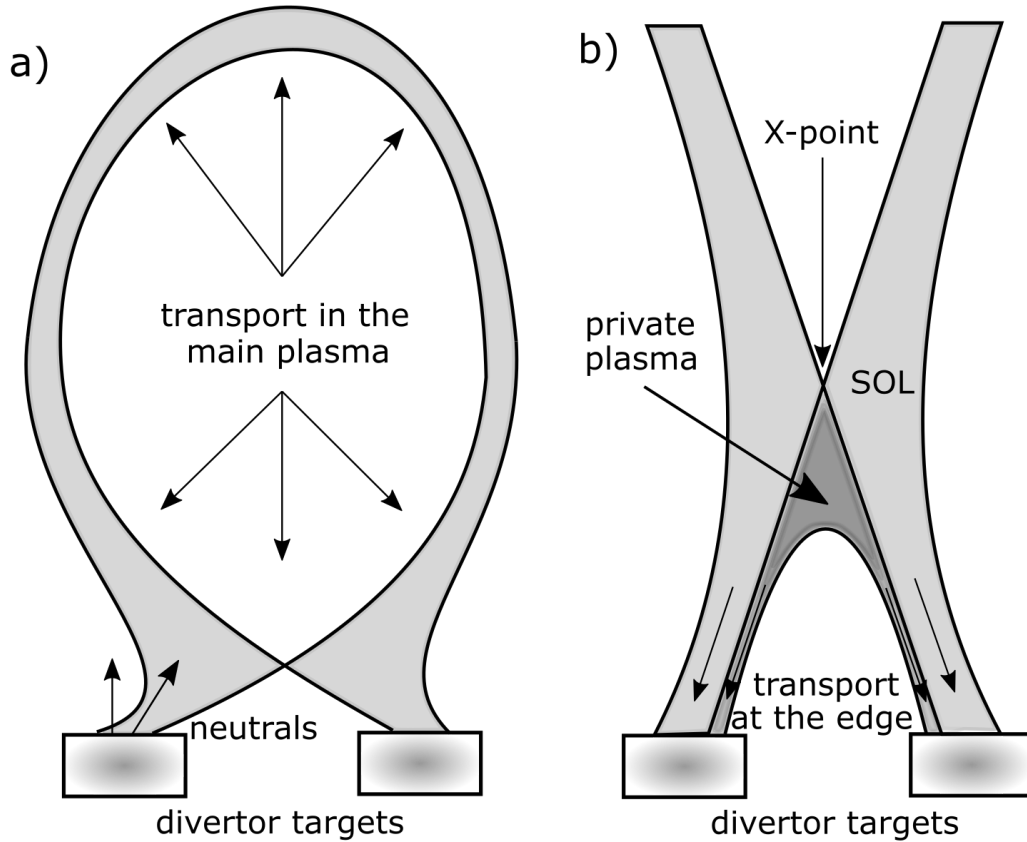


Figure 1.3: Poloidal divertor concept for a tokamak: a) Plasma cross section in a tokamak with a poloidal divertor; b) A close-up look at the divertor target region.

A more advanced concept is the island divertor concept used at W7-X. In this concept a chain of magnetic islands exists outside of LCFS and is interrupted by the divertor targets.

In order to obtain an island chain two conditions has to be fulfilled: a resonate magnetic flux surface of a low-order ι and a Fourier component of the magnetic field with n (toroidal mode number) and m (poloidal mode number) corresponding to $\iota = \frac{n}{m}$ [13]. In the case of Wendelstein 7-X $\iota=1$ is obtained at the LCFS and a Fourier component of the magnetic field matches ι with $n = m = 5$ for the standard magnetic configuration. This results in a chain of 5 islands surrounding the main plasma. For the other magnetic configurations of W7-X ι can vary from $n/m=5/6$ (low ι) to $5/4$ (high ι) with different poloidal mode number m .

The Fourier components of the magnetic field with $n = [1-4]$ are called error fields and should be avoided. They cause a break of the symmetry and asymmetric heat loads onto the divertor targets [13]. To cut this unwanted component of the magnetic field 5 'trim' coils (4 of them are shown in yellow on Figure 1.4) were used. The most challenging technical issues were planar and non-planar magnetic coils (shown in brown and grey in Figure 1.4) with the tolerance of 1 mm. Even small deformation of these coils causes a significant shift (a couple of cm) of the islands and has to be corrected in the calculations.

1.3 Wendelstein 7-X stellarator

In contrast to tokamaks, in stellarators the helical component of the magnetic field is created with the aid of external magnetic field coils. The concept has been proposed by Spitzer in 1958 [14]. This fact differs stellarators in terms of their positive features:

1. Without the need to generate toroidal plasma current with a transformer action stellarators can operate in a steady-state regime.
2. The absence of the toroidal plasma current also puts away problems with the related plasma disruptions.

Naturally, there are also related disadvantages:

1. Advanced stellarators require complicated modular 3D magnetic field coils, what is a true engineering challenge. This was specifically shown for the Wendelstein 7-X stellarator.
2. The complicated 3D magnetic coils cause absence of the toroidal symmetry, making stellarator magnetic topology inherently 3D and complex.

Those two factors had been keeping stellarator line of machines technologically behind tokamaks. In the recent time these two disadvantages were successfully approached due to significant progress both in theory and computational power and now could be considered as manageable challenges. This has been proven as the Wendelstein 7-X stellarator has been successfully commissioned and its magnetic topology has been confirmed with the precision 1:100 000 [13].

This result became possible due to the stellarator optimization. The early stellarators had a problem with particle confinement due to strong particle drifts. The main reasons were inhomogeneity of the magnetic field ($\text{grad}B$ drift) and its curvature (curvature drift). These challenges were not present in the case of tokamaks, were due to the toroidal

symmetry of the magnetic field the drifts were averaged and didn't cause significant issues. W7-AS was the first 'partially optimized' stellarator to prove the concept [15]. The full effect of the optimization will be shown in W7-X, where a complicated set of superconducting magnetic field coils together with improved heating and other properties will allow W7-X to operate at the parameters close to those of a future fusion power plant.

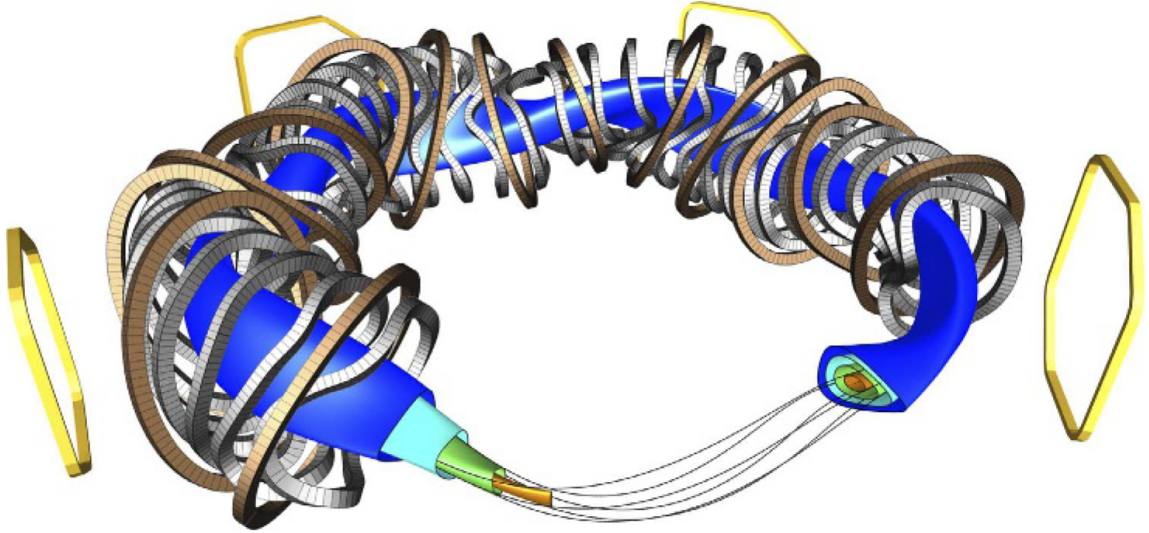


Figure 1.4: Schematic view of the Wendelstein 7-X stellarator (taken from [13]). A set of 4 nested magnetic flux surfaces is shown inside the magnetic field coils. The magnetic field lines shown correspond to the green surface. Planar magnetic coils are shown in brown, non-planar coils in grey and trim coils in yellow.

Parameter	Value	Unit
Plasma volume	30	m ³
Major radius R	5.5	m
Minor radius a	0.5	m
Magnetic field	2.5	T
ι	2π	[5/6 - 5/4]
ECRH power	8.5	MW
Maximum pulse length	100*	s

Table 1.1: Main parameters of W7-X during the divertor campaign OP1.2. * - at 2 MW heating power [16].

W7-X consists of a set of complicated superconducting magnetic field coils. 20 planar and 50 non-planar coils are operating at 3.4 K and are located on the cryostat between the outer and the plasma vessel [16] and are used to generate the main magnetic field. In addition 5 trim coils outside of the outer vessel are used to cancel error fields of the unwanted modes. A thermal shield is actively cooled at 70 K and it contains the plasma vessel, the outer vessel and the superconducting coils.

In the last experimental campaign OP1.2b with the passively cooled divertor an electron-cyclotron resonance heating (ECRH) was mainly used to heat the plasma. It consisted of 10 gyrotrons working at 140 GHz both in X2 and O2 heating modes. These gyrotrons were capable of providing heating power of up-to 8 MW. In the future

1. Introduction

operation campaigns their capabilities should be extended to 15 MW. Neutral beam injection (NBI) system was also available with heating power 3.5 MW. In the future campaigns it will be extended to 20 MW. Ion cyclotron resonance heating (ICRH) is planned to be commissioned in the future providing 3.5 MW of heating power [17]. In this work only the ECRH system was applied during the dedicated experiments.

In the last passively cooled divertor campaign the input energy limit was 200 MJ. This resulted in the longest pulse of 100 s with the reduced heating power of 2 MW. Most of the discharges were 20-30 s long but with higher heating power. Once the actively cooled divertor is installed the input power will be extended up-to 18 GJ with duration of 1800 s, what is the goal of W7-X [16].

The 10 gyrotrons of W7-X are divided into 2 groups with 5 gyrotrons in each group. In Figure 1.5 the 5 gyrotrons of M1 are shown together with their quasi-optical transmission path. The generated beams from each gyrotron path two polarizers P1 and P2 allowing introduction of the phase shift to switch between the polarizations. After this single-beam section (SBS) beams are going through the multi-beam section (MBS) between the M5 and M11 mirrors. After this the beams are separated again and are directed into the plasma via 2 launchers with 3 beam lines with steering mirrors each. In total there are 18 mirrors in each module. Such a configuration allows flexibility regarding polarization and deposition region of power into the plasma.

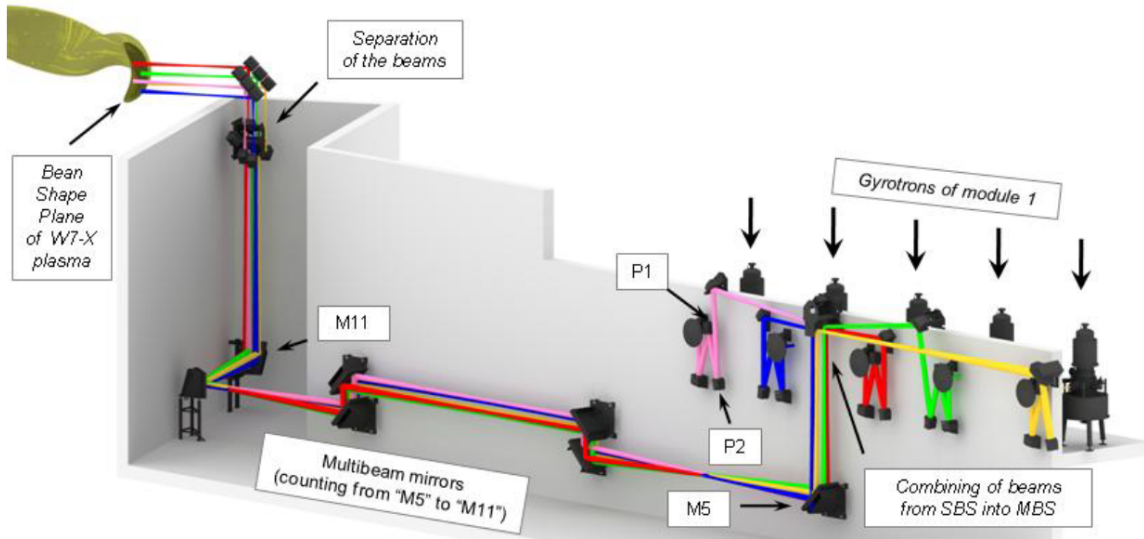


Figure 1.5: Schematic view of the ECRH system at Wendelstein 7-X stellarator (taken from [18]). 5 out of 10 gyrotrons are shown in module 1 of W7-X. P1 and P2 are the polarizers; SBS and MBS stand for single-beam and multi-beam sections; M5-M11 - multibeam mirrors.

ECRH is based on the resonance coupling of the microwave energy to electrons at their second harmonic frequency at 140 GHz. That means that high collisionality between electrons and ions is required for energy transfer from electrons to ions. This collisionality increases with density. For the densities $< 1.2 \cdot 10^{20} \text{ m}^{-3}$ (cut-off frequency) the X2 polarization in the second harmonic can be used. For the densities between $1.2 \cdot 10^{20} \text{ m}^{-3}$ and $1.8 \cdot 10^{20} \text{ m}^{-3}$ the O2 polarization was used. The physical cut-off frequency $2.4 \cdot 10^{20} \text{ m}^{-3}$ of the O2 regime is not achievable due to technical reasons.

The deposition zone has size of 5 mm in the radial direction and 12 cm in the vertical direction on-axis. Absorption in the X2 regime approaches 100% with 1 pass through the plasma. In the O2 regime this value is only 70%. This requires a multi-path

absorption scheme, which was achieved by introduction of a molybdenum tiles covered with tungsten at the high field side of W7-X to reflect the first path beam back into the plasma. The second reflection was provided by a polished stainless steel tile. By passing center of the plasma 3 times absorption of 90% was achieved.

Another usage of the ECRH system is wall conditioning. This question is discussed in the corresponding subchapter 1.6.

In addition, the ECRH system can be used to drive current in the plasma. The so called electron cyclotron current drive (ECCD) has been successfully used to mitigate the toroidal plasma current I_{tor} . Two approaches are possible. The first one is to drive an electric current with the same amplitude as I_{tor} , but with the opposite direction. This approach requires steady state ECCD of up-to 50 kA on-axis. The second approach is to drive current only during the start-up phase of a discharge in the direction parallel to I_{tor} , but with a proper modulation to stop development of I_{tor} . Though this approach is more favourable due to lower current and short duration, it has drawbacks in a form of instabilities. To tackle the instability issue decreasing current density might be needed.

1.4 Plasma-surface interactions

Plasma-surface interactions (PSI) are inevitable in a fusion device. Therefore, it is important to understand all the physical processes to be able to control and optimize them. There are 3 basic scenarios when an ion or an atom approaches a solid state surface (more details can be found in [19]):

1. The particle is reflected or back-scattered into the plasma with some energy loss.
2. The particle can be also implemented in the near surface, thermalized and then released as a thermal particle.
3. The particle can also be trapped in the near surface for a longer period of time and then again released as a thermal particle.

Since the most important elements in Wendelstein 7-X are carbon, hydrogen and oxygen, the further discussion will be focused on the processes related to these atoms and ions. All the ions in the plasma sooner or later reach the sinks and interact with the plasma-facing components. In the case of W7-X those are C for the heat resistant components and Fe for the remote surfaces. The projectiles are H^0 and H^+ as the plasma fuel. Unfortunately, in addition to the plasma fuel there are intrinsic impurities present in the plasma: C^0 , C^+ , O^0 and O^+ .

When an atom or an ion of H, C or O reaches the surface it most likely gets neutralized and the initial charge is not important. If the energy of the projectile is high enough it can cause a momentum transfer to the atoms of the lattice of the plasma facing component (PFC) material and cause its release from the surface. This process related to momentum transfer is called *physical sputtering*.

Typically, the projectile experiences 2 collision in the lattice: the first one in the deeper atomic layers which changes the direction of the projectile back to the surface and the second one in the near surface layers causing the lattice atom to leave the material [19]. This imposes that there should be some minimum threshold energy of the projectile E_{th} . Related values can be found in [19],[20]. For carbon as a substrate E_{th} is: $E_{th}(\text{H}) = 27.3$ eV. The values for D and O are $E_{th}(\text{D}) = 24.3$ eV, $E_{th}(\text{O}) = 100$ eV. In the case of W substrate and H projectiles the value is $E_{th}(\text{H}) = 480$ eV. Obviously, the heavier the substrate material is more resistant it is against physical sputtering.

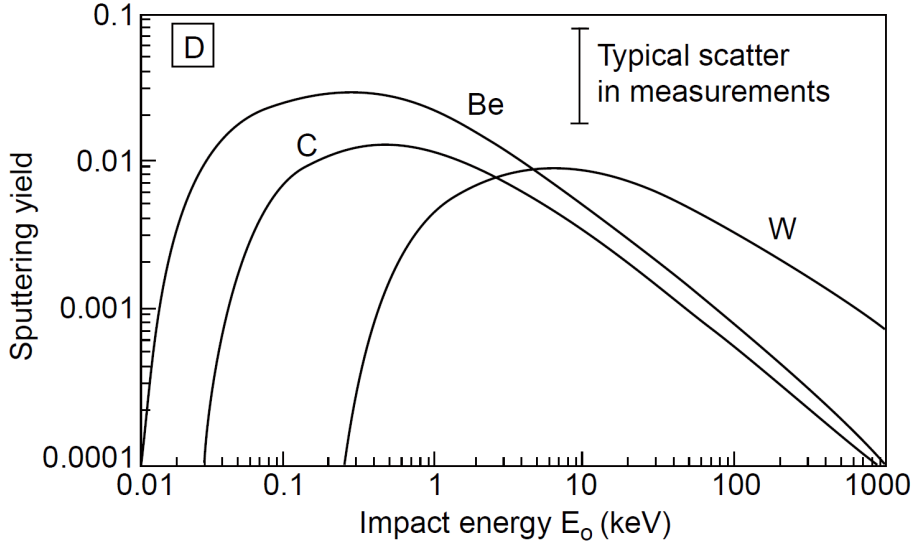


Figure 1.6: Physical sputtering yield of D for different materials of the surface (Be, C and W) as function of the projectile impact energy E_0 . The scale bar in the right corner shows that the uncertainty can reach up to a factor of 2 depending on the surface roughness and other parameters (taken from [19]).

It is straightforward seen that keeping the temperature of the projectiles low is profitable to decrease physical sputtering. In addition, decreasing that temperature below E_{th} could eliminate the problem altogether, though the projectiles are not monoenergetic and there is always the high energetic tail in their distribution allowing those energetic particles to sputter the substrate. Moreover, self-sputtering of the material with the same projectile is very effective due to the equality of their masses.

In addition to the physical sputtering where the momentum transfer is the basis, there is another sputtering mechanism where chemical potential of the particles play the role - *chemical sputtering*. In this case even thermal particles can cause a chemical reaction with the substrate and subsequent release of volatile molecules. Specifically, O^0 and O^+ are extremely challenging in a machine with carbon PFCs, since they easily react with C by breaking the C-C bonds in the lattice and forming CO and CO_2 molecules which are released in the plasma. This process is described in the dedicated subchapter 1.5, since it played the main role in impurity formation in OP1.2 of W7-X. The *yield* Y of such processes is close to 1, where Y is defined as:

$$Y = \frac{\text{number of atoms or molecules ejected}}{\text{number of impacting particles}} \quad (1.10)$$

In addition to O, H is also effectively interacts with C what results in C_xH_y formation and its release into the plasma.

Sputtering yield in general depends on the impinging particle energy, angle and the type of the particles involved. The surface roughness can alter the value significantly too. Energetic dependence of physical sputtering is more pronounced, though the yield of chemical sputtering also increases with the impinging energy. Self-sputtering yields can even be higher than 1 and should be avoided.

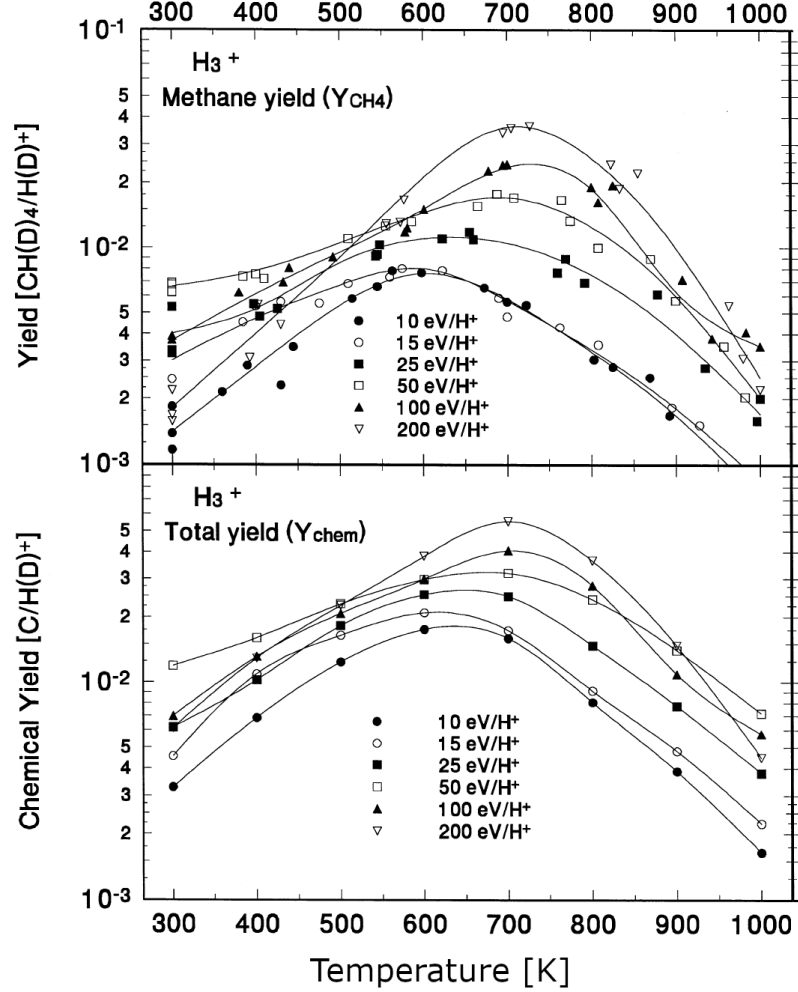


Figure 1.7: Chemical yield Y_{chemical} of C by H for different energies of the impinging H^+ ion: methane only (upper part) and the total value including higher carbohydrates (bottom part), (taken from [21]).

Chemical sputtering also shows dependence on the temperature of the material. The total chemical sputtering yield of C by H together with the methane channel as function of material temperature is shown in Figure 1.7 for different energies of the impinging hydrogen ions. It is clear that yield shows maximum at temperatures in the [600 - 700] K range. In the case of the lowest H^+ energy of 10 eV $Y_{\text{chemical}} \approx 0.01$. For the high energetic H^+ at 200 eV it increases to $Y_{\text{chemical}} \approx 0.03$. The most significant contribution to the total chemical yield comes from methane. For the above two cases this fraction is >0.5 . In addition to CH_4 higher carbohydrates are present and the most significant channels of the reaction are [19]:



The corresponding yield of physical sputtering Y_{phys} of Be, C and W as function of the impact energy is shown in Figure 1.6. For the low impact energies <50 eV physical sputtering is negligible to chemical sputtering for D hitting C. In the range of [50 - 200] eV Y_{phys} increases from 0.001 to 0.01 and reaches those of Y_{chemical} for D on C.

In W7-X the highly loaded C materials get hot during the plasma operation and get into the temperature range $\approx [500 - 1000]$ K and are susceptible to chemical erosion by hydrogen. Therefore, the interplay between these two processes is very complicated to

1. Introduction

model and predict. The only way is to use emission spectroscopy as will be discussed in Chapter 3.

In addition to the above described processes the co-deposition plays an important role - it is a processes when the wall material is eroded and redeposited at a different location. During redeposition it can also bury fuel with itself - so fuel is co-deposited. It is one of the main mechanisms of D and T retention in devices with C walls. Chemical sputtering is also possible, when a molecule is formed as an ejected formation.

In addition different defects can be present in PFC, like vacancies and voids. Fuel (in this case hydrogen) can diffuse in the material, saturate of the surface, get trapped or permutations can happen.

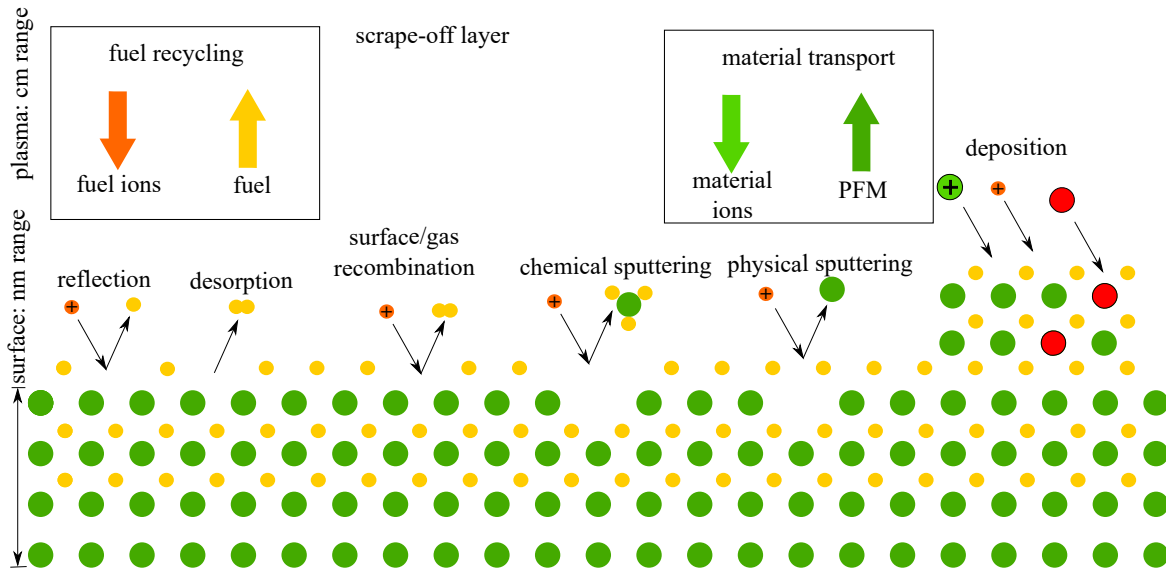


Figure 1.8: Plasma-surface interactions. In addition to the main processes of our interest - physical and chemical sputtering, a number of other processes are present in fusion devices (inspired by a talk by Dr. S. Brezinsek).

1.5 Low-Z oxygen and carbon impurities

The radiation loss R and the mean effective charge \bar{Z} for oxygen, carbon, tungsten and iron are shown in Figure 1.9 as function of electron temperature. From this picture it is clear that line radiation of O and C plays an important role for the electron temperatures $T_e < 500$ eV. For temperatures higher than that both elements are fully ionized and only Bremsstrahlung contributes to R . It might at first glance make an impression that those two species radiate only at the edge of the plasma and do not cause much problems from the point of view of energy loss. This will be shown to be false in the further subsections and Chapter 3.

Tungsten and iron do not get fully ionized even for $T_e > 1$ keV and significantly cool the plasma. In addition, Bremsstrahlung depends on Z as Z^2 and makes it even stronger plasma power radiator.

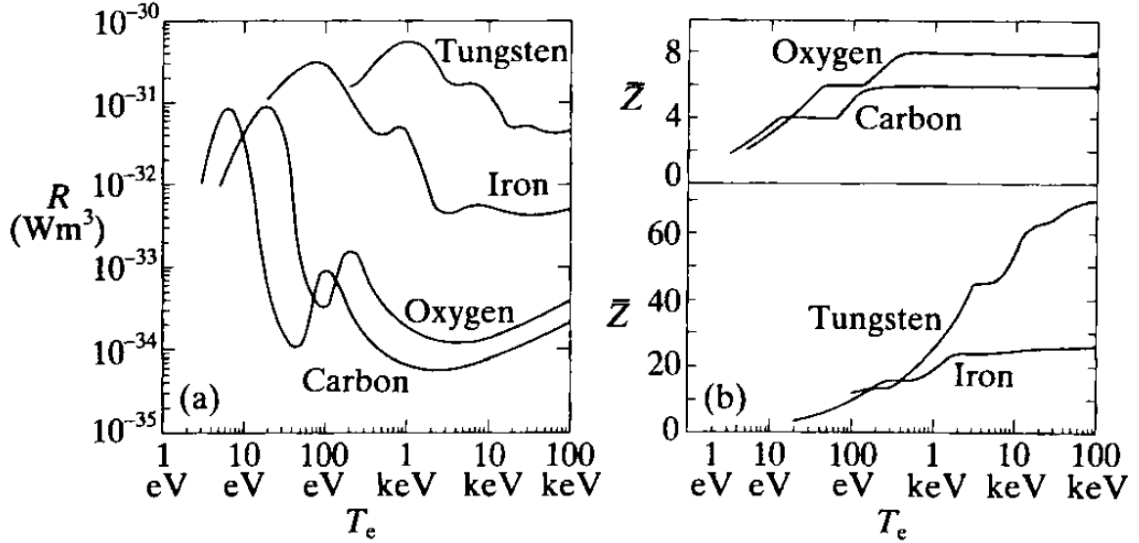


Figure 1.9: Radiation loss function R for low-Z C and O which were the main impurities in W7-X. In addition Fe and W are also shown, but their radiation was not a problem for W7-X, since no W materials were in the plasma vessel and the stainless steel walls did not cause Fe influx in the plasma (taken from [19]).

The second harmful effect of plasma impurities is their dilution of the fuel. Assuming that impurities are completely ionized, their atomic number being Z and concentration c_Z they lead to a decrease in fusion power ΔP_α [19]:

$$\Delta P_\alpha = P_\alpha(1 - Zc_Z)^2 \quad (1.12)$$

Assuming $c_Z = 3\%$, for oxygen this reduction would be 42% and for carbon 33%.

The impurities released from the wall can penetrate deeply into the plasma. Eventually, they are transported back to the sink, but they can accelerate and gain much more energy causing increased physical sputtering. Therefore, it is important to prevent influx of the impurities in the plasma.

It is a well known problem that oxygen is the main impurity problem in machines with carbon wall materials. Baking and H_2 -GDC (the glow discharge cleaning in hydrogen) have shown not to be effective against this issue (see subchapter 1.6). Another solution was found by J. Winter and it is well described in the overview work [22]. The solution was to cover all the machine surfaces with a boron layer to getter oxygen. The further description is based on [22] with additional references and appropriate tailoring to the W7-X case.

Water molecules located in the remote locations of the machine on the stainless steel walls and are also absorbed in the graphite divertor of W7-X. During a plasma discharge those molecules would be removed from the surface, ionized, dissociated and the oxygen ions would be transported to the carbon divertor. Oxygen is easily desorbed from the stainless steel walls because the atomic hydrogen reacts on the surface with the metal oxides forming water molecules:



On the surface of the divertor 1 oxygen atom was implanted per 4 carbon atoms. Due to high chemical reactivity of oxygen with carbon they would be subsequently emitted in the form of CO and CO_2 molecules. The recycling coefficient of O with CO and CO_2

1. Introduction

formation was almost 1 [22]. Those 2 molecules have good chances to penetrate into the plasma, get ionized, dissociated and repeat the cycle. This process is schematically shown in Figure 1.10.

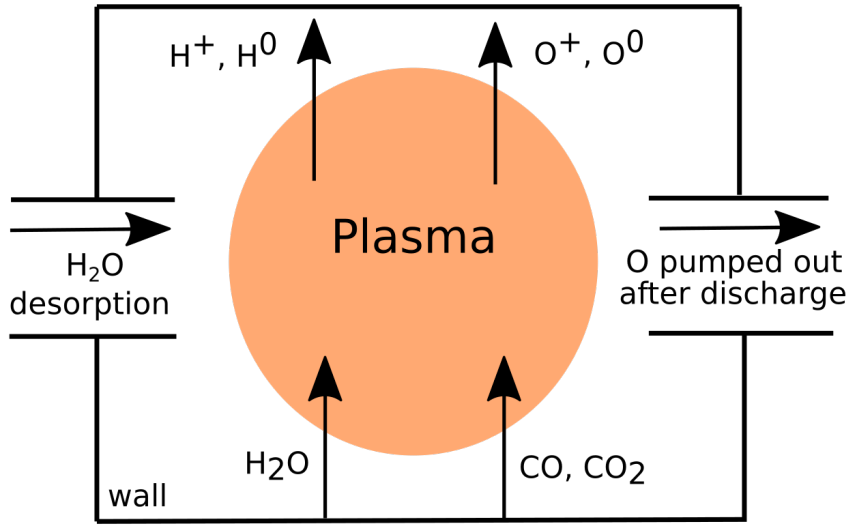


Figure 1.10: Scheme of the oxygen recycling in W7-X (modified [22]).

1.6 Wall conditioning in fusion devices

The problem of low- Z oxygen and carbon impurities is approached with the help of different wall conditioning techniques. In addition to the oxygen and carbon problem (for devices with carbon walls) those techniques are also dealing with the problem of recycling for plasma density control. Moreover, the tritium retention is the common issue for the future fusion power plants.

This subsection is devoted to the techniques intensively used recently in fusion devices and the planned techniques with the focus on W7-X, since this device has already incorporated and it will additionally have the most important techniques. Since all prospective devices will be equipped with superconducting magnetic field coils it is important to distinguish between the techniques applicable when the magnetic field is off:

- Baking
- Glow discharge cleaning
- Coverage of the wall surfaces with a low- Z material

and techniques applicable only with the presence of the magnetic field [23]:

- Radio frequency approaches
- Diverted magnetic configurations with nested flux surfaces

Baking is the wall conditioning technique based on the thermal detrapping of the particles at the PFCs. Not only those at the surface, but also particles from the material bulk can diffuse through the surface and then recombine into volatile molecules and be pumped out of the device. This procedure is the first one after the venting of a machine

and its mainly aimed at water and hydrocarbon molecules. In addition it can also tackle the hydrogen or tritium retention problem. Baking typically lasts for a couple of days and the temperature of the surfaces is 150° C for W7-X, 200 - 300° C for JT-60SA and 240 - 350° for ITER [23].

Baking is not sufficient to provide the required low pressure in the plasma vessel. It was shown in [23] that the neutral pressure P follows the next time dependence:

$$p \propto t^{-0.7} \quad (1.14)$$

The relative change of the plasma pressure is therefore:

$$\frac{\Delta P}{P} = \propto t^{-1} \quad (1.15)$$

This gives that effectiveness of baking quickly drops with time and another method should be applied for further decrease in pressure.

The next step is typically the glow discharge cleaning (GDC). In this case a low temperature $T_e \approx 10$ eV and low density $n_e \approx 10^{16} \text{ m}^{-3}$ plasmas are generated in a hollow cathode discharge [23]. A set of anodes is located around the machine and the wall is grounded and acts as a cathode. A voltage of [100 - 400] V emerges and due to the secondary electron emission the electrons from anodes are accelerated in the sheath and ionize the neutral gas molecules and atoms. Mostly hydrogen and helium are used. In ITER 7 anodes will be used and the 1000 m² wall will act as a cathode.

Those ionized molecules and atoms are accelerated to the surface were due to the chemical or physical sputtering they deabsorb impurities and the plasma fuel from the surface. The effectiveness of this process depends both on the homogeneity of the discharge and the ion current. Those two parameters can be tuned by an appropriate number of anodes around the torus (10 for W7-X), voltage and neutral gas pressure. More details can be found in [24].

H₂-GDC is used to deplete the surface from mainly water and hydrocarbons. In contrast, He-GDC is frequently used to deplete the surface from the retained hydrogen either from a H₂-GDC or a normal plasma discharge in hydrogen to decrease fuel release from the walls and make density control possible. In the case of a He-GDC the process is well described in [23], where the neutral pressure of He and H₂ is described by a set of neutral pressure balance equations for the Wendelstein 7-X case:

$$\dot{p}_{\text{He}} \approx Q_{\text{He}} - p_{\text{He}} \frac{S_{\text{He}}}{V} - (1 - R_{\text{He}^+}) p_{\text{He}} k_{\text{He}}^i n_e, \quad (1.16)$$

$$\dot{p}_{\text{H}_2} \approx -p_{\text{H}_2} \frac{S_{\text{H}_2}}{V} + c(t) Y_{\text{He}^+} p_{\text{He}} k_{\text{He}}^i n_e - (1 - R_{\text{H}_2^+}) p_{\text{H}_2} k_{\text{H}_2}^i n_e, \quad (1.17)$$

where $k_{\text{He},\text{H}_2}^i$ are ionization rates, Q_{He} gas flow of He from external source, S_{He,H_2} vacuum pumping rate, $R_{\text{He}^+,\text{H}_2^+}$ recycling coefficient and Y_{He^+} removing yield of H₂ by a helium ion.

It is therefore important to optimize GDC discharges in a way that re-deposition and retention are minimized. This is achieved by application of a pulsed scenario when a ≈ 10 s pulse is followed by a break to pump out the released particles and avoid the above mentioned processes.

The low- Z coverage of the wall surfaces has been recently done mainly with boron and is discussed in depth in the following subchapter 1.7, since it was the main focus of this work.

With the presence of magnetic field radio frequency approaches are used. The first method is the electron cyclotron resonance heating (ECRH) conditioning. In this case the electron cyclotron resonance or its second harmonic is used to locally absorb power in a currentless discharge.

This immediately directs to the difference between ECRH conditioning in stellarators and tokamaks. In a stellarator an ECRH conditioning discharge inherently has nested magnetic field line structure and follows an experimental magnetic configuration. The most intensive interaction area is also located at the divertor. To optimize wall conditioning a cleaning discharge is typically pulsed and is referred as an ECRH pulse 'train'. An ECRH train consists typically of ≈ 20 pulses of 3 s duration and ≈ 35 s period (as for W7-X [23]).

For the case of a tokamak absence of current infers absence of nested magnetic flux surfaces. The deposition zones is controlled by the poloidal field coils. Its also important to shorten the break down phase to minimize influence of the straight radiation onto the wall.

For both stellarators and tokamaks mostly ECRH conditioning discharges in helium are used to desaturate the wall from hydrogen. To decrease other impurities ion cyclotron resonance heating and boronization are used.

The ion cyclotron resonance heating (ICRH) conditioning is foreseen for ITER as the main wall conditioning mechanism with magnetic field. In this case power is absorbed in the ion resonance. This method will be also used at W7-X [17].

1.7 Boronization

Plasma impurities have a significant influence on the plasma performance because they radiate the energy of the plasma causing the radiative induced collapse and because they dilute fuel in the main plasma. The most important source of impurities are plasma-surface interaction processes. Therefore, it is important to control the influx of impurities in the plasma together with the fuel recycling.

Among other wall conditioning techniques, coverage of the surfaces with low-Z materials like boron proved to be very efficient to tackle the issue of low-Z oxygen and carbon impurities. These low-Z species are specifically problematic for the machines with carbon divertor targets and metallic walls [22].

Boronization was firstly performed at the TEXTOR tokamak [1] and showed significant improvement in the machine performance. After that it was adopted by another devices: ASDEX [25], Tore Supra [26], JT-60U [27], DIII-D [28], NSTX [29], TFTR [30], MAST [31], Alcator C-Mod [32], TCA [33], W7-AS [34], REPUTE-1 [35] and other devices. Lower impurity concentration will allow ICRH heating scenarios. This subsection is devoted to the in-detail description of boronization mechanisms.

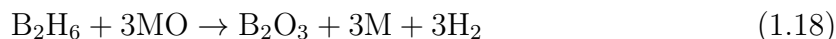
To cut this vicious cycle gettering of oxygen on the surface could be a solution. That mean this surface had to be covered with an element which effectively getters oxygen. In addition, it had to be a low-Z element to prevent plasma power loss and fuel dilution, as explained previously. The most suitable element was boron with $Z=5$.

The boronization is a plasma-assisted chemical vapour deposition of thin films during a glow discharge in either hydrogen or helium. Typically helium is used as a carrier to provide lower hydrogen content in the deposited film. To the carrier gas a boron-containing gas is added like B_2H_6 (diborane) or $B_{10}H_{14}$ (decaborane). Carbon containing options like $B(CH_3)_3$ or $C_2B_{10}H_{12}$ are less favourable since the deposited layers are more susceptible to carbon erosion. The diborane and decaborane gases are highly toxic and

explosive so serious precaution measures have to be applied. As a result coverage of the surface is not uniform depending on the GDC pattern in the machine. The specific procedure in the case of Wendelstein 7-X is described in detail in Chapter 4.

As a result of a boronization the machine walls are covered with an amorphous a-B/H film. The freshly deposited B on the walls effectively getters O. In addition, the chemical erosion of C was shown to be smaller in this case. Obviously, once O is gettered by B the chemical erosion of C by O is strongly suppressed. In addition to the newly deposited layer, the re-deposited layer produces fresh B layers to getter more O. This is also discussed in detail in Chapter 5 for the Wendelstein 7-X case.

It was shown in [22] with the X-ray-induced photoelectron spectroscopy (XPS) method that B_2O_3 molecules are formed. It was also discussed that the diborane gas can react with the metal oxides during boronization:



These processes decrease water release from the metallic wall.

Off course, if boronization is performed with the aid of a GDC it is necessary to switch off the magnetic field of the machine. In the case of superconducting machines like W7-X it was not the problem in the TDU campaign. In the future it might be required to decrease the number of switching on and off the magnetic field to keep the superconducting coils safe. As an alternative to the GDC scenario other techniques could be used, like boron particle dropper or diborane puff during a discharge. The first option seems to not be effective and the second one requires special safety measures. Most probably boronization will be still performed in a helium GDC.

In the work of Refke et al. [36] a set of experiments was performed to study the effect of boronization on the CO and CO₂ reemission under energetic oxygen (O^+) ion bombardment onto different materials. Those materials were: pure graphite (EK98), graphite with different B concentration (3%, 15% and 20%), graphite sprayed with a B₄C layer and the a-C/B:H layer on graphite after boronization. The emitted species were detected with the help of residual gas analysis (RGA) at 45° to the incident O^+ beam.

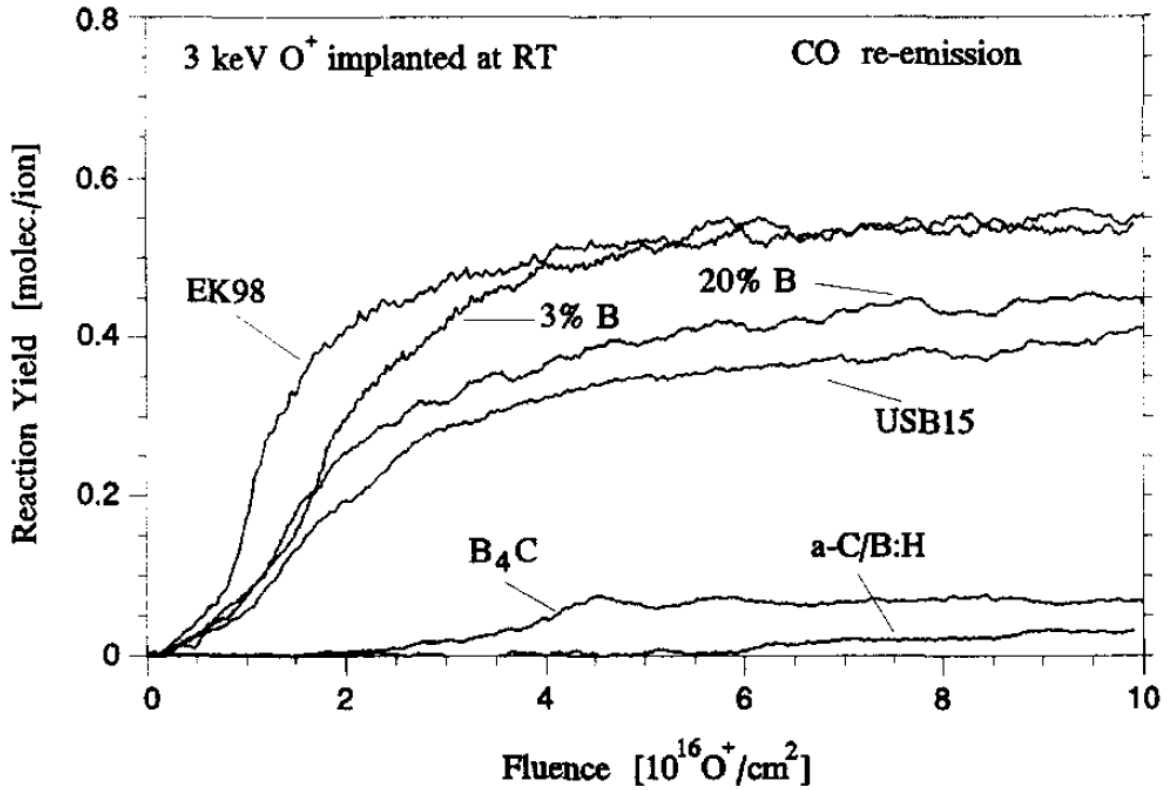


Figure 1.11: Reaction yield of CO formation for different materials during 3 keV O^+ bombardment. The oxygen flux was at the order of 10^{18} m^{-2} for all cases. The most relevant materials are EK98 (graphite) and a-C/B:H, which show difference in the CO yield of more than 10 times (taken from [36]).

The resulting CO yield is shown in Figure 1.11. In this figure only the yield of CO is shown, but the yield of CO_2 follows the same behaviour with the values lower by a factor of ≈ 6 . The yield of boron oxides is very low and was not detected in the mentioned studies.

As the O^+ fluence increases the reaction yield in Figure 1.11 increases until reaching saturation at different values for different materials. For the case of pure graphite (EK98) and the B doped materials it happens at $\approx 3 \cdot 10^{20} \text{ m}^{-2}$. Before saturation oxygen is trapped up-to concentrations of 1 oxygen ion per 4 carbon atoms. After saturation total CO and CO_2 yield is ≈ 0.7 . The pure graphite and boron doped graphite show only a small difference in the total reaction yield and prove to be very challenging materials in terms of O recycling.

In contrast, the pure graphite sprayed with B_4C and the pure graphite covered with a-C/B:H film after boronization show a significant reduction of CO and CO_2 yield. In the case of boronization the deposited film is capable of oxygen retention of up-to $\approx 6 \cdot 10^{20} \text{ m}^{-2}$. After this it starts to re-emit CO and CO_2 at the yields of more than 1 order of magnitude lower than in the case of pure graphite. This proves that boronization is the most effective method to tackle the oxygen problem in a machine with graphite divertor targets and baffles, like Wendelstein 7-X.

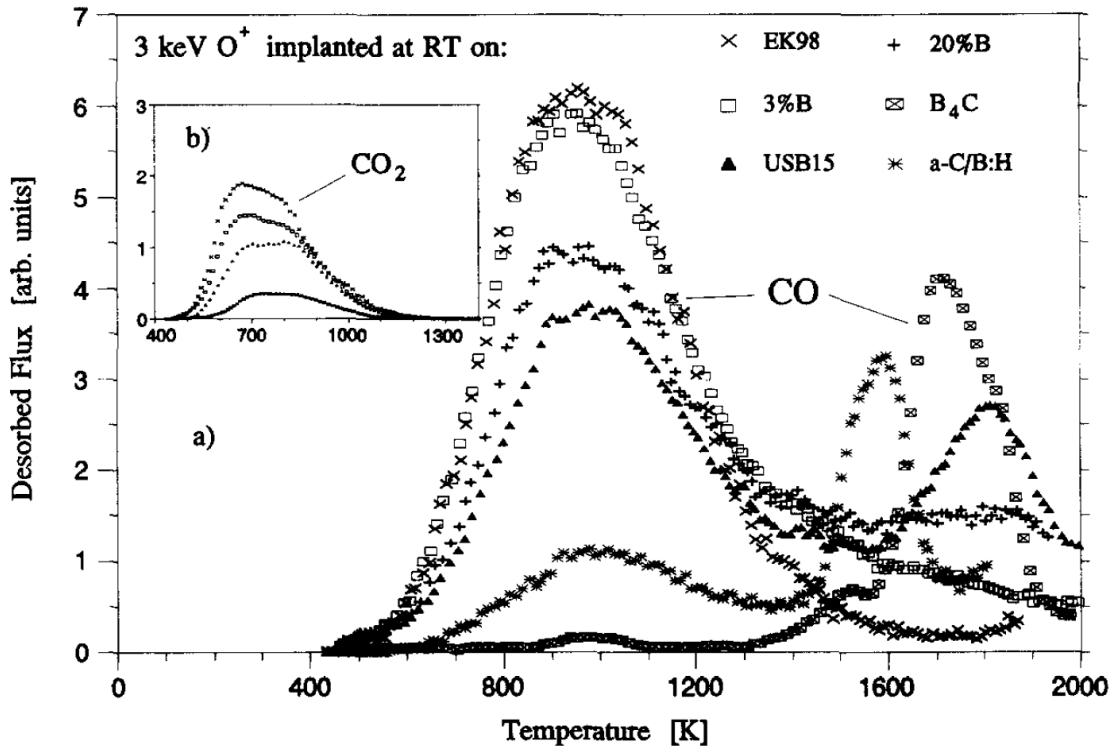


Figure 1.12: Thermal desorption spectra of CO and CO₂ molecules for different materials, with the most important graphite EK98 and the a-C/B:H layer. The energy of the O⁺ ion was 3 keV and the oxygen fluence $1 \cdot 10^{21} \text{m}^{-2}$ (taken from [36]).

In addition to the oxygen ion bombardment studies the thermal desorption spectra (TDS) provides more information. Figure 1.12 shows these spectra in the range of temperatures up-to 2000 K where all the mentioned samples were heated with the speed of 11.5 K/s. The main part shows the CO desorbed flux and the in-built part shows the CO₂ case. The energy of O⁺ was 3 keV and implantation was done at room temperature.

In the case of pure graphite the CO spectra shows one peak at ≈ 850 K and the CO₂ one peaks at ≈ 700 K. The sample with the a-C/B:H film shows a significantly smaller (by ≈ 6 times) peak at this temperature, but in this case an additional peak appears at ≈ 1600 K. The appearance of the additional peak was explained in terms of increased BO, BO₂, B₂O₂, B₂O₃ decomposition at these high energies. Due to the complicated chemical processes the released oxygen reacts with carbon causing the second peak. There is no second peak for CO₂ since this molecule is not stable at these high temperatures.

It is obvious that the positive action of the deposited a:C/B-H film can be compromised if the film is heated to the temperatures higher than 1600 K. Nevertheless, this is not the problem since all the PFC components of Wendelstein 7-X will be much cooler. The divertor targets, specifically the strike line, are not the main O gettingting surface anyway, as is shown in Chapter 5. Therefore, this second peak does not impose any problem for the future Wendelstein 7-X operation in the sense of the boronization film oxygen gettingting.

To conclude the study of Refke et al. [36], the positive impact of boronization was caused by two reasons. Those two reasons are:

1. Increase in the O retention by gettingting with the formation of boron oxides.
2. Decrease of CO and CO₂ formation.

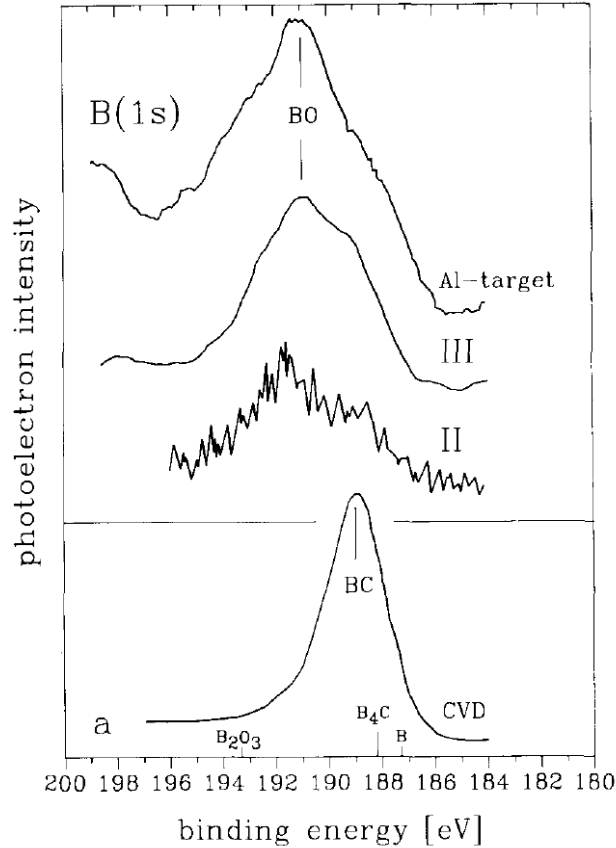


Figure 1.13: XPS spectra of the 1s core level of B for different samples and conditions. II stands for B flushing, III for boronization - in both cases graphite sample was considered. Al-target shows the case of an aluminium sample after boronization. The bottom part shows spectra for the graphite sample after boronization without exposure to plasma (taken from [37]).

The mechanism of gettering by boron oxides formation was studied in detail by Wienhold et al. [37] after application of boronization in TEXTOR. An empirical equation based on collection experiment was deduced to express oxygen retention $O(r)$ [37]:

$$O(r) = S(r)OI + GB(r) + (AD(r) = 0), \quad (1.19)$$

where $S(r)OI$ describes ion sticking of oxygen based on the measurement of the OI line emission at specific position, r - radial position in the SOL and $S(r)$ ion sticking coefficient. The second term describes oxygen gettering by boron, with gettering coefficient G and boron rate $B(r)$. The last term stands for oxygen absorption from air and is not point of interest, since all measurements were done before plasma vessel opening.

It was shown that the gettering part had the biggest contribution in the equation and the sticking part is negligible. The sample was analyzed with the help of the X-ray photoelectron spectroscopy (XPS) for the core level 1s of B and is shown in Figure 1.13. The upper part corresponds to the samples after boronization. II stands for B flushing and III for ordinary boronization. In the case of II and III graphite samples were used. Al-target was measured after ordinary boronization. The bottom part shows spectra for a graphite sample after boronization which had not been exposed to plasma, so only covered with a-B/C:H layer.

The bottom spectra shows a covalent B-C bound at ≈ 189 eV. The top curves clearly show an addition of a B-O nonstoichiometric bound at ≈ 191 eV. The B-O bound is very

stable and forms once free B atoms are available. Therefore, redeposition processes play an important role in oxygen gettering providing fresh boron atoms, which is shown in Chapter 5.

1.8 This thesis

This work is focused on the impact of boronizations on impurity sources, performance in Wendelstein 7-X and the underlying mechanisms. The boronizations were performed during the last experimental campaign with the passively cooled graphite test divertor unit (OP1.2b, July - October 2018). The boronizations allowed a significantly extended operation window of W7-X with high core plasma densities and low impurity content. Understanding effects of boronizations is essential in the view of the future experimental campaigns which will have discharges of up-to 30 minutes length.

Chapter 2 is devoted to the edge and divertor diagnostics for impurity characterization at W7-X. It begins with the subchapter devoted to the endoscope system, aiming at plasma-surface interaction studies, UV-VIS-IR spectroscopy and tomography at the plasma edge. The full description is given, including its optical layout, detector system and the UV-VIS-NIR spectroscopy part. The specific contribution of the author of this thesis (the author) was:

- Characterization of the imaging part in the sense of spatial resolution to meet the experimental requirements.
- Application of a computer vision technique was used by the author to correct image distortions present due to the assembly imperfections.
- Support of the assembly team, including the ZEMAX optical software procedures.
- Absolute calibration of the overview spectrometer system, the VIS and UV filter cameras including the image intensifiers for the UV branch.

Additionally various diagnostics data were used to support the photon influx spectroscopy results. The author either used the data from the repository server or coordinated with the responsible scientists. The main diagnostics are described here: edge particle and photon flux data was used from the divertor Langmuir probes, midplane multipurpose manipulator and filterscopes. To understand influence of boronization on the impurity levels in the core of the plasma the high efficiency extreme ultraviolet observation system (HEXOS), bolometry and dispersion interferometry systems were used too.

Chapter 3 describes spectroscopy methods used in this work. Photon influx spectroscopy was the main method to obtain normalized influx of boron, oxygen and carbon before and after boronization. Helium beam emission spectroscopy together with 2D tomography reconstruction is foreseen to obtain 2D T_e and n_e profiles at the divertor region of W7-X. The current status of available collisional radiative models is given and a line-integrated image measured experimentally is compared to the synthetic picture obtained by modelling. Next a 2D tomographic method based on singular value decomposition is applied to test synthetic images by forward and reverse reconstruction.

1. Introduction

A detailed overview of observed atomic, ionic and molecular spectra is given. Original contribution of the author in this chapter is:

- Application of the photon influx spectroscopy to the divertor plasma of W7-X for B, C, H and O for the TDU campaign results.
- Application of the SVD reconstruction method for 2D emission profiles of He injected at TDU.
- A detailed overview of atomic and ionic line spectra of N, Ne, C, He, H, O together with molecular bands of N_2^+ , NH^+ , CN, CH, C_2 , C_3 , CO_2 at divertor plasma as observed by the overview spectroscopy system.

Chapter 4 is focused on the wall conditioning methods applied to W7-X before boronization during OP1.2b. Baking, glow discharge cleaning, electron cyclotron wall conditioning had been applied prior to boronization. Nevertheless, after decrease of impurity levels low-Z oxygen and carbon prevented W7-X to operate at high core plasma density. The boronization set-up is described together with the strategy used by the author to study boronization effects on W7-X.

Chapter 5 is the most important part describing effects of the boronizations on the impurity sources and performance in W7-X. This part originally produced by the author and partly published in [2]. The photon influx spectroscopy measurements were performed by the author with the help of the overview spectroscopy system. Additional data were provided by the responsible scientists. Firstly electron temperature and density profiles are compared before and after boronization. Then the change in low-Z impurities carbon and oxygen radiation is characterized. Power loads on the divertor follow the discussion. Morphology and chemical composition of the divertor surface were studied to provide more information on the boronization mechanisms in W7-X. Lastly difference of short and long-term boronizations effects are discussed.

Chapter 6 summarizes this work. Conclusions are made and an outlook is given. Boronization has proven to be an effective method against the low-Z impurities oxygen and carbon during the passively cooled test divertor unit campaign of W7-X. In this campaign discharges of maximum duration 100 s in different magnetic configuration were used providing frequent change of the strike line location which was favourable for redeposition of boron. In the future campaign of W7-X an actively cooled divertor will be installed aiming at a steady state discharge of up-to 1800 s duration in one magnetic configuration. These new conditions will require further investigation for application of boronization.

2

Edge and divertor diagnostics for impurity characterization at Wendelstein 7-X

2.1 Endoscope system at Wendelstein 7-X

W7-X is aiming for a steady-state operation with high plasma performance. Therefore, the question of plasma-surface interaction is of high importance because of the negative effect of the impurities on the plasma performance due to divertor target erosion, cooling of the main plasma and fuel dilution. There are also positive side of the externally introduced impurities to radiate power in SOL or near the boundary of the main plasma to reduce heat loads on the divertor target. In addition, puffing of He can produce important information on the edge T_e and n_e profiles.

The 3D magnetic topology of W7-X significantly influences the PSI processes and, therefore, this synergy between the 3D edge physics and PSI is an important field of research. The magnetic topology significantly depends on the plasma effects like bootstrap currents. This changes the impurity transport, the impurity sources on the divertor and recycling.

To study these aspects a diagnostic set-up together with modelling have been developed [38],[3]. It is important to be able to get edge impurity profiles together with the corresponding plasma parameters. These parameters will be obtained with an endoscope system - 2 sets of 2 endoscopes with the nearly perpendicular field of view allowing 2D tomographic reconstruction of impurity line radiation. Each endoscope will employ: filtered cameras for UV and VIS range; high resolution and overview spectrometers in IR, VIS and UV range; IR camera for infrared thermography. A gas injection system consisting of 5 nozzles is located in the field of view of the endoscopes. The endoscope system is described in detail in the next subsections.

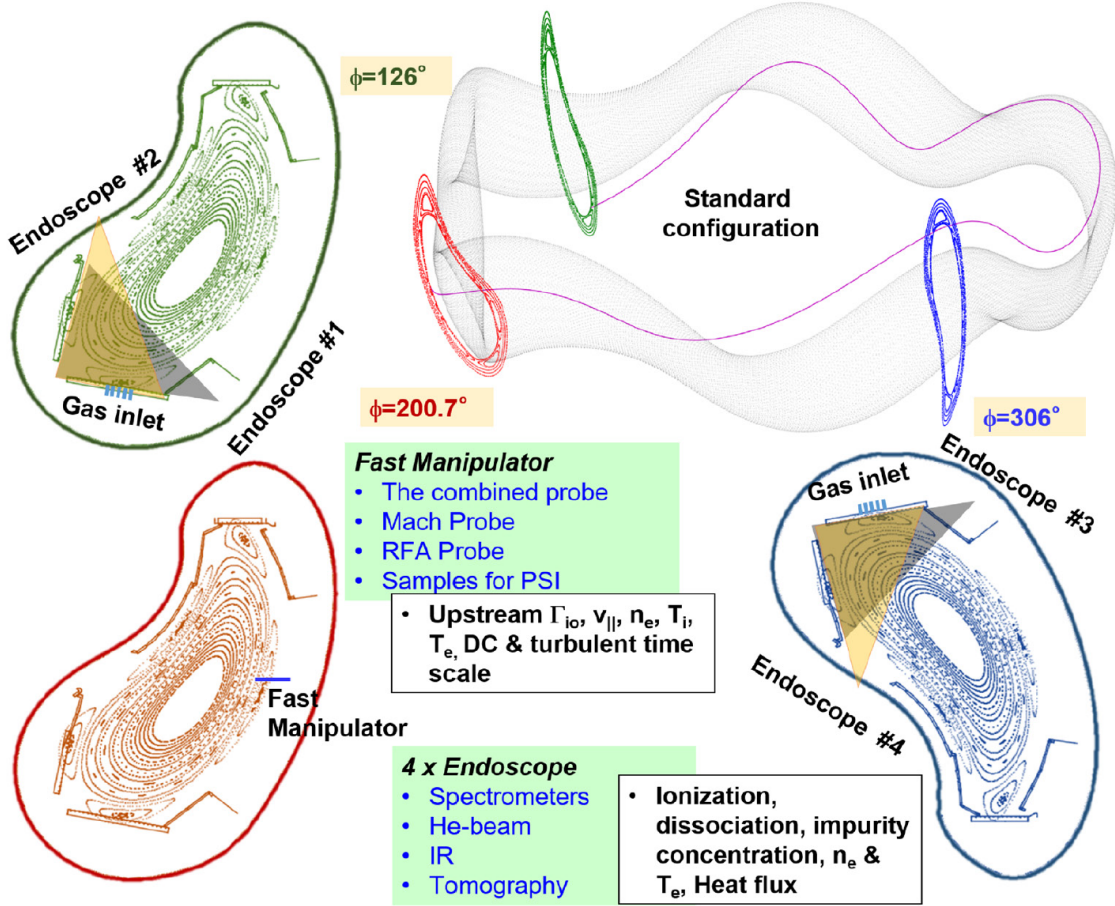
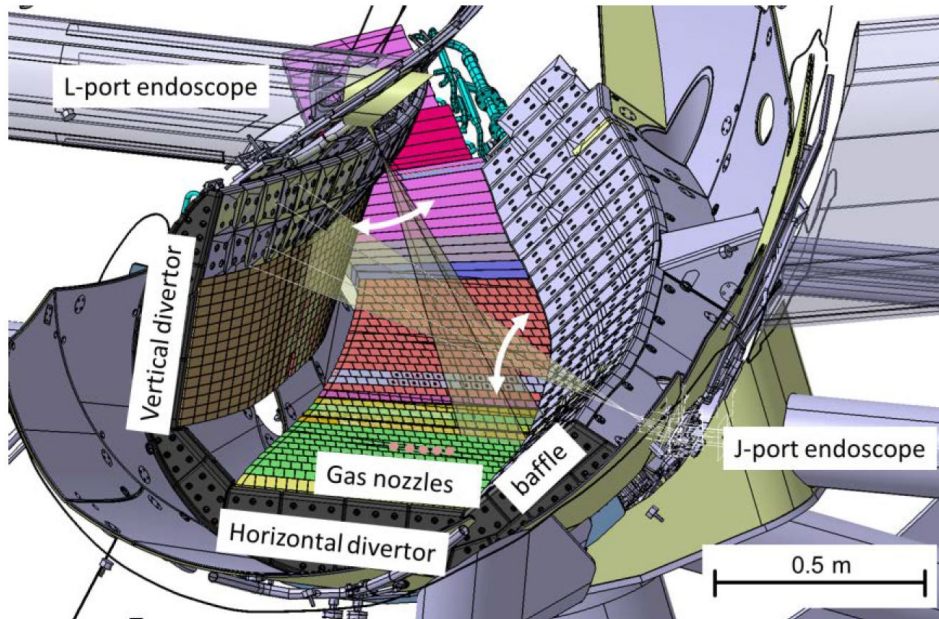


Figure 2.1: Edge diagnostics to study synergy between the 3D edge topology and the PSI processes on W7-X (taken from [38]). The right top corner shows the 3 poloidal cross-section where the endoscope system (green and blue) and MPM (red) are located. The connection of the diagnostics is shown with a magnetic field line (magenta) starting at the MPM position for the standard magnetic configuration of W7-X.

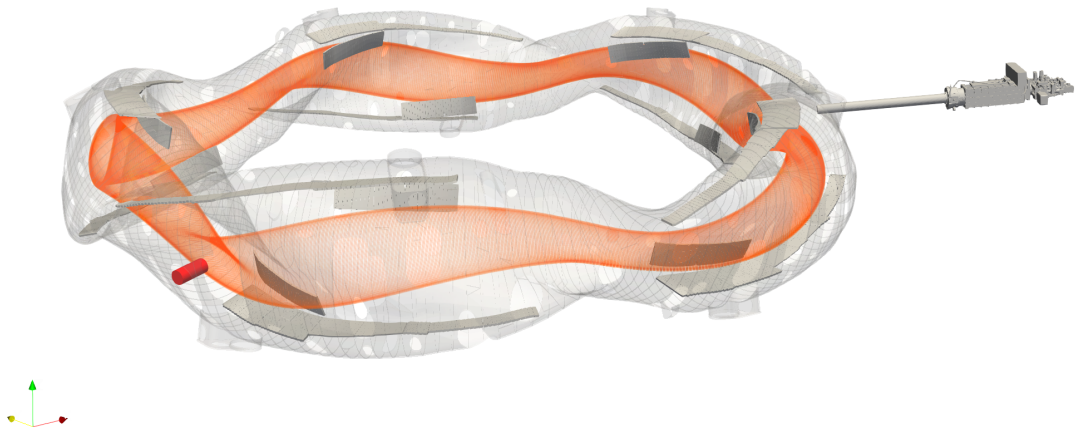
The upstream plasma parameters can be measured with a multi-purpose manipulator which can be equipped with different probe heads to measure T_e , n_e , T_i , for example with the Forschungszentrum Jülich (FZJ) combined probe [39]. It is also capable of carrying samples for PSI studies or to inject gases for fueling or impurity transport studies [40]. In the standard magnetic configuration of W7-X all the mentioned diagnostics are connected along magnetic field lines allowing projection of all of them in one poloidal cross-section for plasma parameters cross-usage.

The above described system is shown in Figure 2.1. In the top right corner a Poincaré map of the standard magnetic configuration is shown. The line in magenta shows an example of a magnetic field line connecting all diagnostics. The corresponding Poincaré maps are shown in red, green and blue. The red cross-section corresponds to the location of the multi-purpose manipulator and its plunge distance is shown in blue. The green and the blue cross-sections show the location of the endoscopes and their field of views are shown in the top left and the bottom right corners. The corresponding toroidal angles ϕ are given for each location.

2.1.1 Optical layout



(a) M30 module of W7-X. A set of 2 endoscopes in the J- and L-ports allows observation of the edge plasma with nearly perpendicular fields of view. The rotation of the first mirror of the endoscopes allows scanning of in the poloidal direction (30°). In addition a sequence of 5 gas nozzles is mounted in the horizontal divertor target (taken from [41]).



(b) The first installed endoscope during the OP1.2b TDU campaign (July - October 2018) of W7-X was at the AEJ51 port and is shown in grey on the right. A closed magnetic flux surface is shown in orange together with the combined probe position shown in red. The machine components are semi-transparent grey.

Figure 2.2: Endoscope location scheme.

The main 4 magnetic configurations exploited during the experimental campaign OP1.2b with the passively cooled graphite divertor at W7-X were: standard, low- ι , high- ι and

high-mirror. In this subsection the magnetic structure is discussed at the position of the M51 endoscopes: toroidal angle $\phi = 302.9^\circ$. The Poincaré maps for the mentioned 4 magnetic configurations are shown in Figure 2.3. The figures were produced with the help of field-line tracing tool developed for W7-X [42].

In Figure 2.3.a the standard configuration is shown. It is characterized by $\iota = 5/5$ at LCFS. In the figure the 5 magnetic islands are clearly seen outside of LCFS, which is shown in red. Those magnetic islands are completely independent. The upper 2 islands are cut-out by 2 divertor targets and create the plasma-wetted area, where most of the PSI processes take place. Specifically, this is of highest interest for the photon influx spectroscopy.

In the case of the high-mirror and the standard configurations $\iota = 5/5$ at LCFS, providing 5 independent islands. The high-mirror configuration is special due to high mirror ratio $b_{01}=10\%$.

The low- ι configuration is characterized by $\iota = 5/6$ at LCFS with 6 magnetic islands outside of LCFS. This configuration is also of interest for the endoscopes system due to presence of strong PSI zone in its view.

The last main magnetic configuration is high- ι with $\iota = 5/4$ at LCFS with 4 magnetic islands outside of LCFS. In this configuration the magnetic island in view of the endoscopes system does not intersect the divertor target and does not provide sufficient photon fluxes for the PSI studies.

All the above mentioned magnetic configurations are shown for the plasma current (neo-classic bootstrap current) $I_{\text{tor}} = 0$. During a plasma discharge I_{tor} can develop which causes the strike line to widen and shift to the pumping gap between the divertor targets. For tomographical purposes its important to know the exact position of the flux surfaces for each I_{tor} when an image was recorded. For both the low- ι and high- ι configurations the magnetic islands are interconnected with each other.

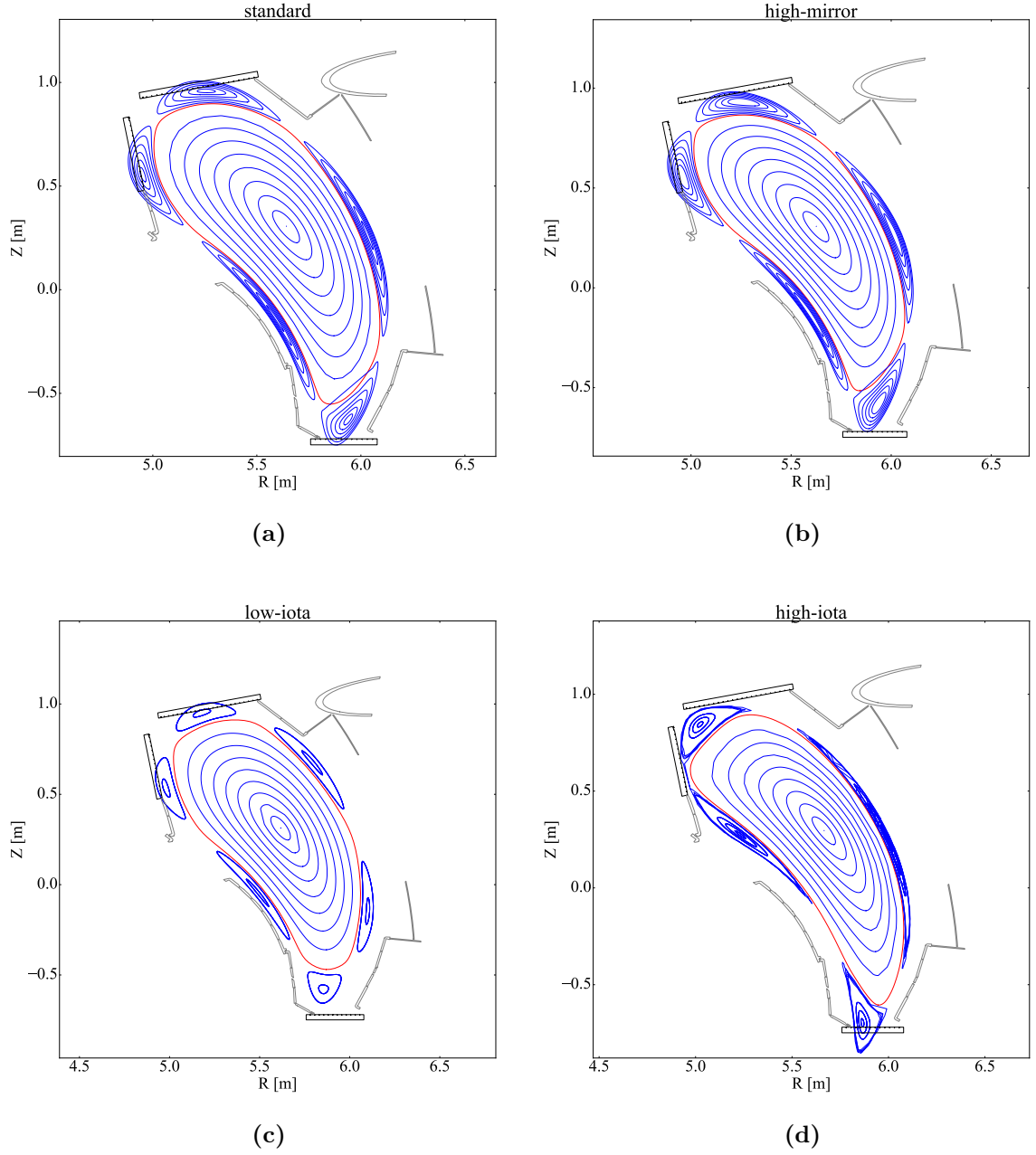


Figure 2.3: Poincaré maps of the 4 main magnetic configuration of W7-X used in OP1.2b: a)standard; b)high-mirror; c)low- ι ; d)high- ι . LCFS is denoted in red, while magnetic flux surfaces of the main plasma and the islands are shown in blue. The black lines correspond to the solid surfaces.

In addition to the Poincaré maps shown in Figure 2.3 it is important to know the L_c profiles at the vicinity of the field of view of the endoscopes, with $R = [4.8 - 5.6]$ m and $Z = [0.4 - 1.1]$ m, which is shown in Figure 2.4. The colormap used in this figure exploits the grey color for maximal values.

The structure of L_c corresponds to the Poincaré maps. For the standard and high-mirror configurations 2 islands are present in the vicinity of 2 divertor target plates (are shown in blue). Moreover, the O-points can be clearly seen in Figure 2.4 in the center of islands marked with grey according to the colorbar. The regions of the islands with the highest values of $L_c \in [100 - 1000]$ m correspond to the plasma-wetted areas. For the standard configuration FWHM of the strike line ≈ 15 cm.

2. Edge and divertor diagnostics for impurity characterization at Wendelstein 7-X

The low- ι configuration provides even greater area with such a high values of L_c . This reflects in the highest photon intensities measured during experiments allowing the shortest integration times among magnetic configurations. The position of the O-points are also clearly seen in the plasma, as for the high-mirror configuration.

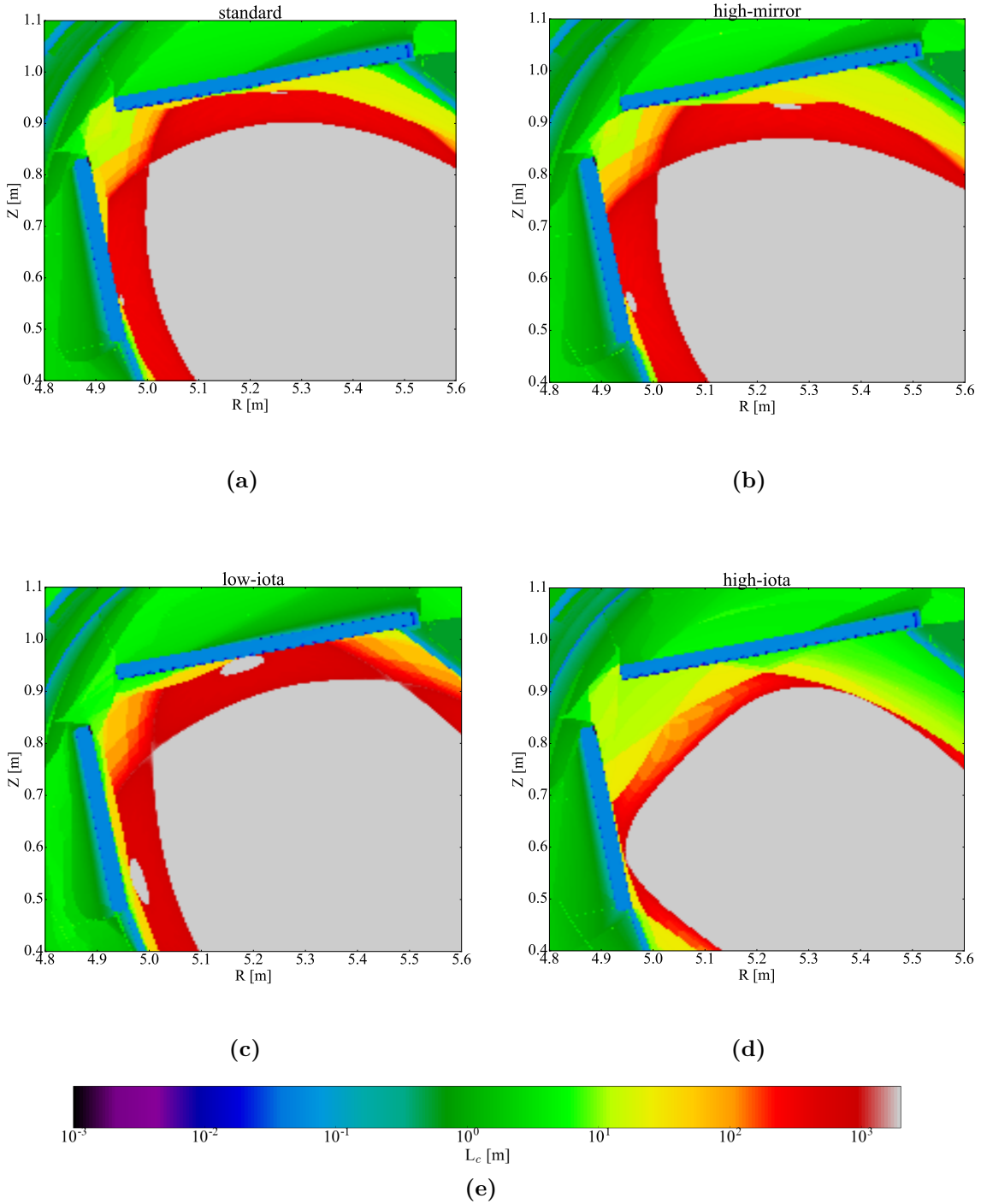


Figure 2.4: Connection length L_c of the 4 main magnetic configuration of W7-X: a)standard; b)high-mirror; c)low- ι ; d)high- ι ; e)colorbar for the (a-d) plots.

In contrast to the above mentioned configurations, the high- ι configuration does not have areas where magnetic islands are intersected in the vicinity of the field of view of the

endoscope system. A small area is only seen at the vertical divertor target and provides insufficient amount of information of the PSI processes.

A scheme based of reflective optics has been selected to provide high flexibility of the endoscope and its resistance to neutron damage. In addition such a scheme mitigates chromatic aberrations in the wide range of wavelengths: [350 - 7000] nm.

The optical path consists of 6 aluminium coated mirrors divided into the endoscope head (mirrors 1-4 = M_1 - M_4) and into the mirror box (mirrors 5-6 = M_5 - M_6). The first mirror is placed into a rotatable casing after the aperture of $4 \times 4 \text{ mm}^2$ size. This allows high spatial resolution due to the narrow viewing angle (9° in poloidal and toroidal directions) overcompensated by 30° rotation allowing observation of both divertor targets together with the magnetic island by scanning.

In addition to the scanning function, the rotatable casing is also used as a shutter to close the optical path and as a mirror to check for depositions and deterioration. These functions depend on the position of the rotatable casing, when it either closes the optical path from the plasma vessel or puts a dedicated reflecting mirror on the optical path to reflect light coming from the back part of the endoscope. It should be mentioned here that during OP1.2b of W7-X the shutter was open through the complete campaign and after re-calibration no signs of decreased transmission has been observed. This indicates that M_1 is well screened from transport of carbon or other impurities.

The M_1 - M_4 mirrors are located in the endoscope tube inside W7-X so vacuum conditions must be fulfilled. Additionally, the internal surface of the tube is covered with an anti-reflection coating. The vacuum-air barrier is provided by a double wedge-shaped CaF_2 window to reflect ghost images and provide transmission in the wide wavelength range. The M_5 - M_6 mirrors are located in the mirror box and serve to define focal length.

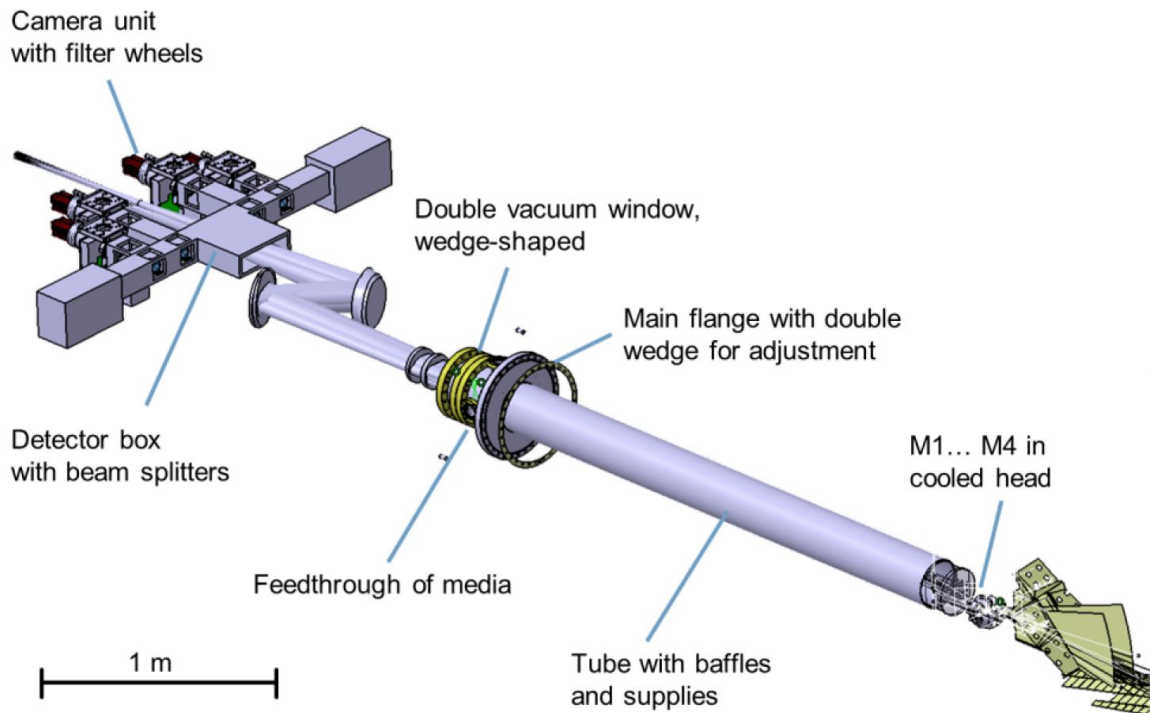
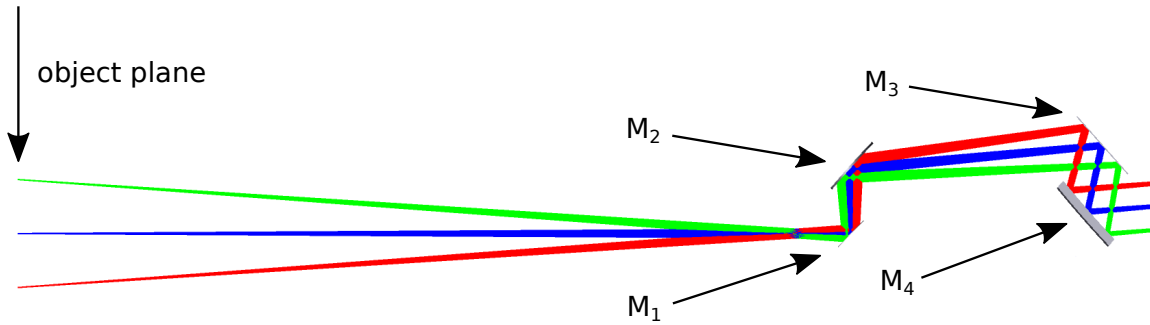


Figure 2.5: CAD scheme of the endoscope (taken from [41]).

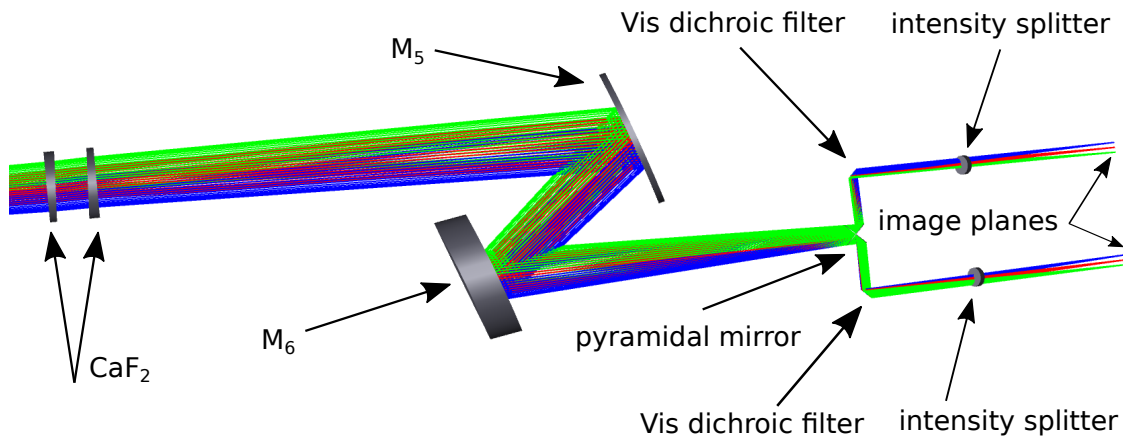
The CAD drawing of the complete endoscope is shown in Figure 2.5, where additionally the entrance slit is shown in front of the aperture. In Figure 2.6 the optical path is shown produced by the ZEMAX software package. 3 field sources were

2. Edge and divertor diagnostics for impurity characterization at Wendelstein 7-X

selected in the object plane: $x = 0$ mm; $y = (0, 35, -35)$ mm. The optical path is optimized in sense of ghost images and spatial resolution.



(a) Optical path from the object plane to the M₄ mirror. 3 colors correspond to the 3 source fields: $x = 0$ mm; $y = (0, 35, -35) = (\text{blue}, \text{green}, \text{red})$.



(b) Continuation of the optical path from the CaF₂ vacuum wedge-like window to the sensor planes.

Figure 2.6: Optical scheme of the J endoscope obtained with the ZEMAX software package.

2.1.2 Detector system

At the back part of the endoscope the detector box is located. It contains an impressive amount of cameras and fiber outputs for spectrometers (see Figure 2.7):

1. 3 cameras for the VIS range
2. 2 cameras for the UV range (with an image intensifier)
3. 1 single fiber for the overview spectrometer
4. 2 fiber bundles for the UV spectrometers
5. 1 fiber bundle for the VIS spectrometer
6. 1 fiber bundle for the IR spectrometer
7. 1 camera for the IR range

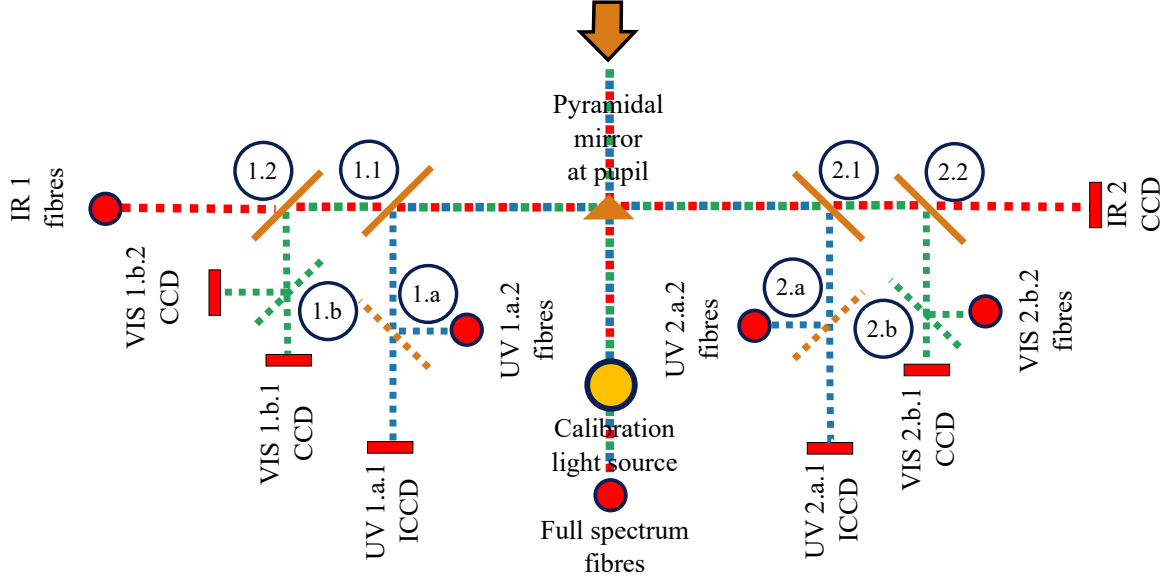


Figure 2.7: Detector box of the endoscope. 1.1, 2.1 - dichroic beam splitters deflecting the UV range; 1.2, 2.2 - dichroic beam splitters deflecting the Vis range; 1.a, 1.b, 2.a, 2.b - intensity beam splitters; UV 1.a.1, UV 2.a.1, VIS 1.b.1, VIS 1.b.2, VIS 2.b.1 - CCD cameras in the corresponding wavelength ranges; IR2 - the IR camera; UV 1.a.2, IR1, UV 2.a.2, VIS 2.b.2 - fibre bundles for spectroscopy in the corresponding wavelength range (taken from [41] and modified). UV: [350 - 550] nm, VIS: [550 - 950] nm, IR: [950 - 7000] nm.

In total there are 11 optical branches per 1 endoscope. In order to divide the entering light in these 11 branches an optical layout shown in Figure 2.7 has been chosen. The incoming image was divided in 2 equal parts with a pyramidal mirror. At the tip of the pyramidal mirror a fiber array of 19 fibers was located in order to guide the light to the overview spectrometer system. In addition, one of the fibers was designed to be used for self-calibration together with an in-built light source during an experimental campaign.

After the pyramidal mirror the light was split into 3 wavelength ranges: UV, VIS and IR with the help of dichroic filters arranged by 45° to the beam. The first dichroic filters 1.1 and 2.1 reflect the UV range allowing 2 UV cameras (1.a.1, 2.a.1) and 2 UV fibre bundles (1.a.2, 2.a.2) to obtain the UV part of the image. The VIS part of the spectrum was transmitted further.

Subsequently, the dichroic filters 1.2 and 2.2 reflect the VIS range and transmit the IR range. 3 Vis cameras (1.b.1, 1.b.2, 2.b.2) and 1 Vis fibre bundle are sitting in this part. The rest of the light is in the IR range and it proceeds to the IR2 camera and the IR1 fibre bundle.

Two of five CCD cameras are aimed at the UV range. Specifically, weak lines such as H_γ , H_2 and CH Gerö bands are in this region. In order to be able to observe these weak lines an image intensifiers have been used. The same producer and model was chosen as in the case of previous devices: ProxyVision - MCP-Proxifier. The most important characteristics of the image intensifiers are given in Table 2.1:

Type	BV 2562 BZ
Photocathode	bialkali
Phosphor screen	P43
Control voltage	0 - 5 V
MCP output voltage	400 - 800 V
Highest sensitivity	200 - 500 nm
Number of MCPs	1
Gateability	No

Table 2.1: Relevant properties of the image intensifiers used.

The principal scheme of a micro channel plate (MCP) intensifier is shown in Figure 2.8. Photons coming from a weak light source impinge on a photocathode and release electrons (Figure 2.8.c). In this case the photocathode is bialkali (model P43) and optimized for the UV range [300 - 550] nm. The electrons released from the photocathode are passing a cellular structure of microchannels where they are guided and accelerated due to the applied electric field and electron multiplication occurs (Figure 2.8.b). The multiplied electrons then hit a luminescent screen and the produced visible light is then transferred to the CCD chip by a taper made of optical fibers to provide scaling between the MCP screen and the CCD chip. Such a configuration provides high spatial resolution with the gain factor of up-to 10^4 .

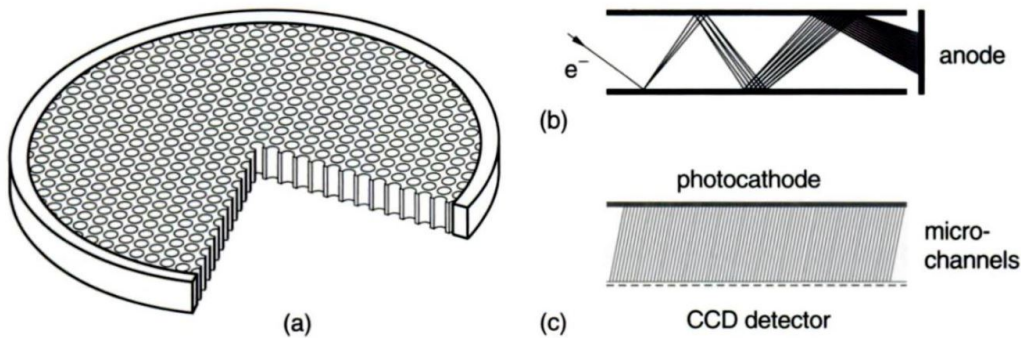


Figure 2.8: MCP scheme (taken from [43]).

The image intensifiers have been calibrated in the same geometry as the Pike cameras [44] and the overview spectrometer. An Ulbricht sphere was used as a light source. For high control voltages grey filters have been used and their transmission have been included in the calculation. The *UV 1.a.1* image intensifier was calibrated with an H_β filter and the *UV 2.a.1* image intensifier with a CIII interference filter. The accelerating voltage is tuned by applying the control voltage to the device interface. This control voltage was scanned in the range [0 - 5.0] V with the 0.5 V step.

The results of the gain calibration are shown in Figure 2.9. The markers show measured values and the dash line show linear fit of the gain in a semilogarithmic scale, from which gain can be calculated for values of the control voltage which were not measured. Such linearity of the gain in semilogarithmic scale is caused by the dependence of electron gain on the control voltage u , which is:

$$\text{Gain} \propto 10^{u \cdot \text{constant}} \quad (2.1)$$

A deviation from this linearity is only observed for $u > 4.5$ V. In the feasible range of control voltage [1.0 - 4.5] V the dependence is linear can be easily interpolated.

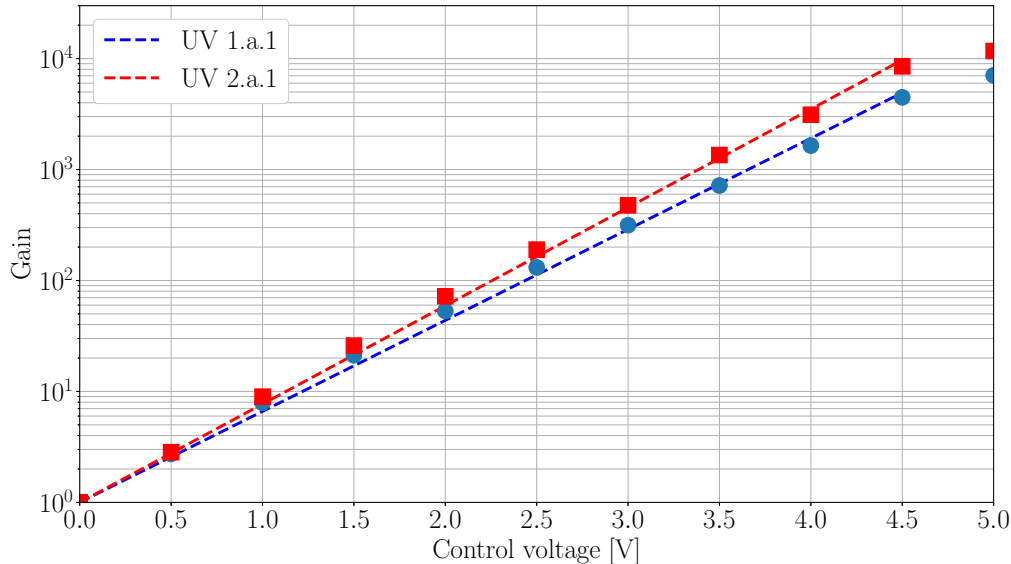


Figure 2.9: Measured gain of the image intensifiers at the cameras UV 1.a.1 and UV 2.a.1 (as shown in Figure 2.7).

The most important part of the detector box of the endoscope system is the filter camera module (FCM). FCM consist of the next parts:

1. Filter wheel for the neutral density filters: 6 positions (1 empty)
2. Filter wheel for the narrow band interference filters: 6 positions (1 empty)
3. 3 CCD cameras for the VIS branch
4. 2 CCD cameras with image intensifiers coupled with a taper for the UV branch
5. Motors to provide rotation of the filter wheels, control electronics, tuning knobs

The most important part of FCM in terms of data acquisition and transfer is the camera. Specifically, the F-145B Pike by Allied Vision monochrome camera was used. Its maximum image resolution is 1388×1038 pixels at 30 frames per second rate. The interface is IEEE1394b FireWire via a fiber connection. The sensor was of Type 2/3 SONY ICX285 progressive scan CCD. The pixel size of the detector was $6.45 \mu\text{m}$ [44]. The control of the filter wheels as well as the MCPs was done via the control unit of the camera.

To avoid confusion it is important to note that the camera was using a 14-bit analog-to-digital converter with a 16-bit output raw data format. Since the information on the output data format was rather hidden in the data sheets it is important to mention that the output raw data file is a binary file where the value of charge counts in each pixel are represented by a 2-byte value. This values is stored according to the Little Endian format, were the lower byte goes first. In addition, the last 2 bits of the lower byte are always 0 due to the 14-bit ADC. Therefore, to correctly read the data it is needed to shift the value by 2 positions right and then swap the bytes. The 2-byte values in a raw

2. Edge and divertor diagnostics for impurity characterization at Wendelstein 7-X

file are represented in a form of a 1D array which has to reshaped accordingly to the resolution of the image.

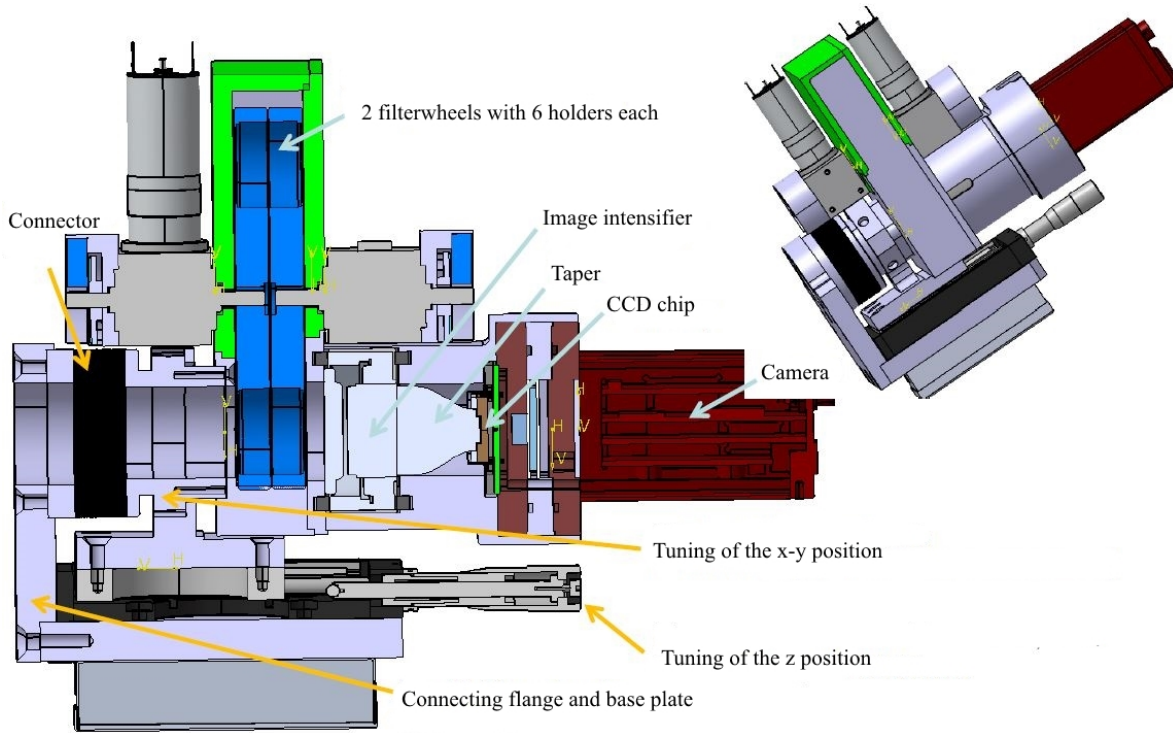


Figure 2.10: Schematic view of the filter camera module (FCM). The 2 filter wheels are shown in blue. The other important elements are denoted in the figure [produced by A. Charl].

Model	λ_{CW} [nm]	FWHM [nm]	Line
010FC06-25	410.06	1	HI (H_{δ})
010FC06-25	426.30	1	CII
020FC34-25	430.70	2.0	CH
010FC08-25	433.90	1	HI (H_{γ})
010FC08-25	465.03	1	CIII
015FC10-25	486.00	1.5	HI (H_{β})
020FC35-25	516.50	2.0	C_2
030FC36-25	601.50	3.0	H_2
015FC12-25	656.10	1.5	HI (H_{α})
015FC12-25	667.82	1.5	HeI
015FC12-25	706.52	1.5	HeI
015FC12-25	728.13	1.5	HeI
020FC37-25	909.48	2.0	CI

Table 2.2: List of the interference filters installed on the AEJ51 endoscope during the experimental phase OP1.2b. λ_{CW} - central wavelength, FWHM - full width at half maximum.

Position	Filter 1	Filter 2	Filter 3	Filter 4	Filter 5	Filter 6
VIS 1.b.1	empty	HeI 728.13	HeI 706.52	HeI 667.82	CI 909.48	H_2 601.5
VIS 1.b.2	empty	HeI 728.13	HeI 706.52	HeI 667.82	CI 909.48	H_α 656.10
VIS 2.b.1	empty	HeI 728.13	HeI 706.52	HeI 667.82	H_2 601.50	H_α 656.10
UV 1.a.1	empty	C_2 516.50	CII 426.30	CIII 465.03	CH 430.70	H_β 486.00
UV 2.a.1	empty	H_δ 410.06	CII 426.30	CIII 465.03	CH 430.70	H_γ 433.90

Table 2.3: Position of the interference filters installed on the AEJ51 endoscope during the experimental phase OP1.2b in the corresponding filter wheels. Numbers after lines are λ_{CW} in [nm]

2.1.3 Endoscope image correction and resolution

It is of high interest that the image distortions caused by imperfections of the assembly and the modeling can be counter-acted with the help of computer vision algorithms. Specifically, the *OpenCV* library was used in this work [45].

The algorithm provided by *OpenCV* employs a pinhole camera model. In this model the transformation between the object (in general 3D) space and the camera 2D (pixel) space is performed by the perspective transformation [46]:

$$s \cdot \mathbf{m}' = \mathbf{A}[\mathbf{R}|\mathbf{t}]\mathbf{M}' \quad (2.2)$$

where \mathbf{s} - scaling factor, \mathbf{m}' - image vector in pixels, \mathbf{A} - camera matrix containing camera (optical system) internal parameters, $[\mathbf{R}|\mathbf{t}]$ - is rotation and translation matrix and \mathbf{M}' - object matrix. The camera matrix needs to be calculated once and then is used for all configurations. In contrast, the rotation and translation matrix must be calculated for each imaging geometry - for example for every angle of the first mirror of the endoscopes.

The above mentioned matrices can be written in a more explicit way:

$$s \begin{bmatrix} u \\ v \\ 1 \end{bmatrix} = \begin{bmatrix} f_x & 0 & c_x \\ 0 & f_y & c_y \\ 0 & 0 & 1 \end{bmatrix} \begin{bmatrix} r_{11} & r_{12} & r_{13} & t_1 \\ r_{21} & r_{22} & r_{23} & t_2 \\ r_{31} & r_{32} & r_{33} & t_3 \end{bmatrix} \begin{bmatrix} X \\ Y \\ Z \\ 1 \end{bmatrix} \quad (2.3)$$

where image vector (u, v) is in pixels, focal lengths vector (f_x, f_y) and principal points vector (c_x, c_y) are also in pixels.

So far only the perspective transformation has been discussed. Now the distortion part comes into the equations. Two types of the distortions are considered in *OpenCV*: radial and tangential. The radial distortion appears on the image as curvature of otherwise straight lines and it increases with the distance from the optical axis. Therefore, it only depends on the radial distance from the image center $r = \sqrt{x^2 + y^2}$:

$$x' = x(1 + k_1 r^2 + k_2 r^4 + k_3 r^6) \quad (2.4)$$

$$y' = y(1 + k_1 r^2 + k_2 r^4 + k_3 r^6) \quad (2.5)$$

where x' and y' are the corrected values and k_1 , k_2 and k_3 - are radial distortion coefficients. If $k_1 > 0$ then it is distortion of a 'barrel' type (lines are curved outside of

the image) and if $k_1 < 0$ then it is distortion of a 'cushion' type (lines are curved inside of the image).

The tangential distortion comes from misalignment of the mirrors and appears on the image as if some parts were closer or more far away even if the object is perpendicular to the optical axis. This is corrected via introduction of the p_1 and p_2 parameters:

$$x' = x + (2p_1xy + p_2(r^2 + 2x^2)) \quad (2.6)$$

$$y' = y + (p_1(r^2 + 2y^2) + 2p_2xy) \quad (2.7)$$

Therefore, the task of *OpenCV* is to find the distortion coefficients (k_1, k_2, k_3, p_1, p_2) and the intrinsic camera parameters (f_x, f_y) and (c_x, c_y). Then the final position of the corrected image (u, v) in pixels are:

$$u = f_x \left(x(1 + k_1r^2 + k_2r^4 + k_3r^6) + 2p_1xy + p_2(r^2 + 2x^2) \right) + c_x \quad (2.8)$$

$$v = f_y \left(y(1 + k_1r^2 + k_2r^4 + k_3r^6) + 2p_2xy + p_1(r^2 + 2y^2) \right) + c_y \quad (2.9)$$

To calculate the distortion coefficients and the intrinsic camera parameters it is required to take an image of a chess-board pattern. Such a pattern was measured in the focal plane of the AEJ51 endoscope for the visible camera (VIS 2.b.1) and is shown in Figure 2.11a. The algorithm knows that the lines are parallel and the squares should be of the same size in the object plane. It detects the corners where two black squares touch each other (color dots in the figure) and then by numerical methods finds the needed parameters.

The corrected image is shown in Figure 2.11b. It is clear that almost all distortions in the original images have been corrected. With this method all obtained images at W7-X must be corrected using the parameters obtained by *OpenCV*.

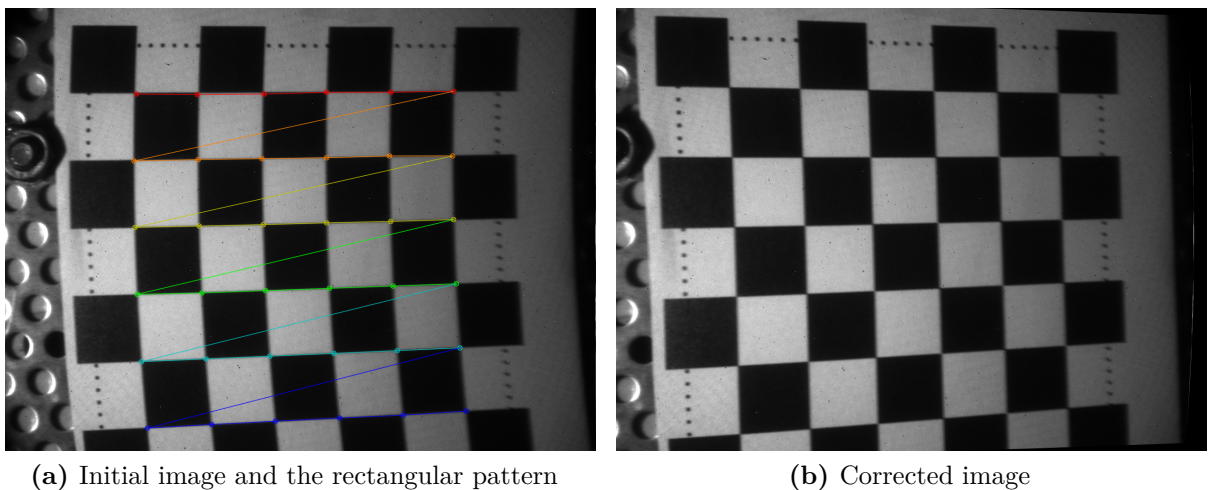


Figure 2.11: Usage of the OpenCV library to correct image distortions: a) The uncorrected chess-board pattern together with the identified black squares intersections (in color); b) The corrected image.

One of the most important characteristics of an optical system is its ability to resolve image details at specific values of contrast. To quantitatively describe a system a common approach is to use the modulation transfer function - MTF.

The most suitable explanation is to use a sequence of completely black and white rectangles (line-pairs) in the object space. When width of these line-pairs is high then it is easily distinguished by the optical system and those line-pairs clearly appear in the image. Once their size decreases - so the inverse value of spatial frequency (w [lp/mm], number of line-pairs per mm) increases - the image becomes blurred and the contrast decreases. So MTF combines spacial resolution and contrast abilities of the system and is defined as:

$$MTF(w) = \frac{I_{\max}(w) - I_{\min}(w)}{I_{\max}(w) + I_{\min}(w)} \quad (2.10)$$

For the endoscope system the minimal spatial resolution was defined as 2 lp/mm in the focal plane on the optical axis at 90% contrast. That means that the spatial resolution is 0.5 mm.

To quantify MTF experimentally a simple but an effective approach was used. A slit of tunable width was put in the focal plane of the AEJ51 endoscope. Behind the slit an Ulbricht sphere was used to back-illuminate the slit with a homogeneous light. A set of slit widths d was selected: 0 mm (to measure background), 0.05 mm, 0.25 mm, 0.5 mm, 0.75 mm, 1 mm, 1.25 mm, 1.5 mm, 1.75 mm, 2 mm, 3 mm and 4 mm. These values of d (except $d = 0$) correspond to a set of values of the spatial frequency w : 10 lp/mm, 2 lp/mm, 1 lp/mm, 0.7 lp/mm, 0.5 lp/mm, 0.4 lp/mm, 0.3 lp/mm and lower values could not be resolved.

The measured profiles of the slit were averaged over its height and the background was subtracted. Afterwards this profile was overlapped 10 times with its self with a shift which corresponds to the FWHM of the profile. After this, according to Equation 2.10 the values of MTF were calculated with the first order approximation.

A more proper explanation of the MTF can be found in [47], where transfer function is well explained. The basic idea is that a continuous object $f(x,y)$ is transformed with the help of impulse response $h(x,y)$. The impulse response characterizes transformation of a point (delta function) in the object plane into a 2D distribution in the image plane. Basically, it is the point spread function (PSF). This transformation can be written in the form of a 2D convolution:

$$g(x, y) = f(x, y) \otimes h(x, y) \quad (2.11)$$

In the case of harmonic forms in the object plane the transformation can be written as:

$$G(\epsilon, \eta) = F(\epsilon, \eta) \cdot H(\epsilon, \eta) \quad (2.12)$$

where: (ϵ, η) - spectral frequencies for (x, y) , $F(\epsilon, \eta)$ - object spectrum, $G(\epsilon, \eta)$ - image spectrum, $H(\epsilon, \eta)$ - transfer function, a Fourier transformation of $h(x,y)$.

When $H(\epsilon, \eta)$ is normalized to be $H(0,0)$, than it is called the optical transfer function - OTF:

$$OTF(\epsilon, \eta) = |H(\epsilon, \eta)| \cdot e^{i\Theta(\epsilon, \eta)} \quad (2.13)$$

The absolute value of OTF is the required characteristic MTF. Considering only one spatial coordinates, as it was done before, MTF can be written as:

$$MTF(\epsilon) = \left| \frac{FT(g(x))}{FT(f(x))} \right| \quad (2.14)$$

where FT stands for Fourier transform. The equation above basically corresponds to:

$$MTF(\epsilon) = \frac{M_{\text{img}}(\epsilon)}{M_{\text{obj}}(\epsilon)} \quad (2.15)$$

For the case of the simple model described above, $M_{\text{obj}}(\epsilon) \approx 1$ and $MTF(\epsilon) \approx M_{\text{img}}(\epsilon)$. This approximation is a good first estimate.

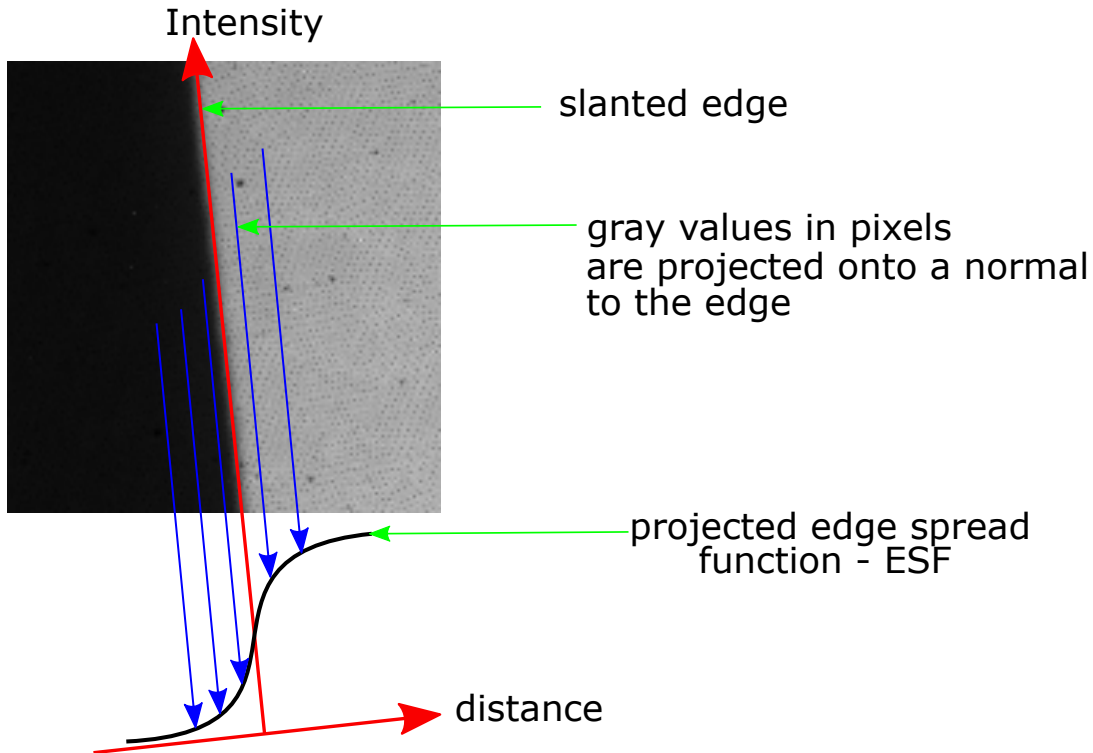


Figure 2.12: Illustration of the slanted-edge method of MTF calculation.

The real calculation of MTF can be very effectively optimized using the open-source program *MTF mapper* [48], which is based on the slanted-edge method described in [49] and [50] by the developer. The main advantage of the method is its robustness against image distortions.

The slanted-edge method is based on the idea of imaging a slanted-edge and projection of the obtained values between black and white parts on a normal to this edge. This projection is called edge spread function (ESF) - see Figure 2.12. Then a sequence of steps is applied to ESF, as explained in [49]:

- By computing derivative of ESF the line spread function (LSF) is obtained.
- The edges of LSF are apodized.
- Fast Fourier Transform is performed on LSF.
- MTF is calculated as magnitude of the FFT coefficients.

All results are shown in Figure 2.13. The values calculated by **Zemax** and **MTF Mapper** give very close values up-to the frequencies of 3 lp/mm. For higher frequencies the measured values starts to decay faster than those calculated by Zemax. The simple slit approach gives values with much smaller contrast and those values can be considered

as the lowest possible. That means that the measured MTF values for the frequency of 2 lp/mm is in the range of [0.8 - 0.94], which contains the requested value of 0.9.

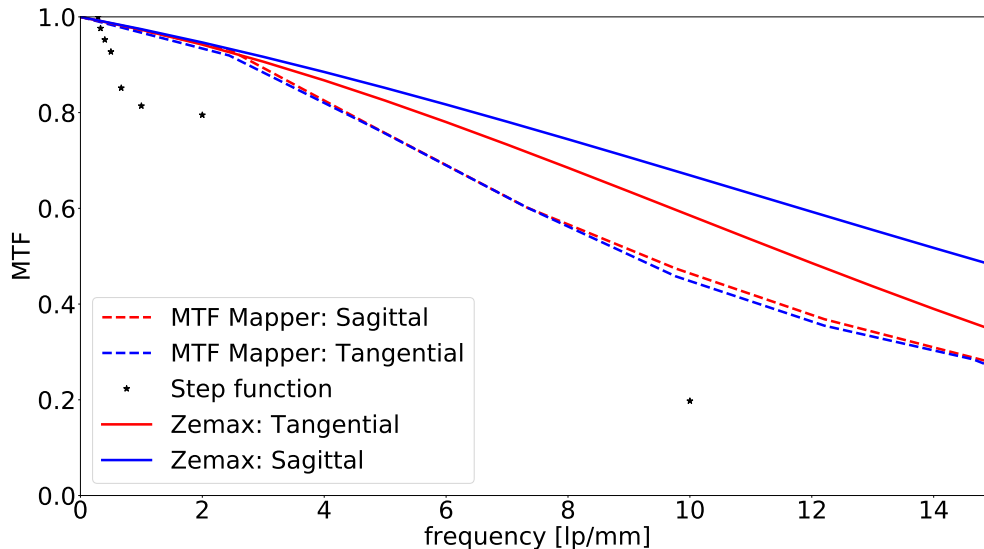


Figure 2.13: Values of the MTF function of the AEJ51 endoscope for the visible camera (VIS 2.b.1) without interference filters (polychromatic). The results of Zemax calculation are shown for the point in the center of the image in the wavelength range from 350 nm to 550 nm for both sagittal and tangential components. The values obtained with *MTF Mapper* were chosen from the location on the image close to the optical axis and are shown for both sagittal and tangential components. The values obtained with the slit approach are shown too.

2.1.4 UV-VIS-NIR overview spectroscopy

The ultraviolet-visible-near infrared overview spectroscopy system played a major role in characterization of boronizations at W7-X during OP1.2b. In contrast to OP1.2a (the first part of the TDU campaign, 2017), when it was temporary connected directly to a viewing port [5], in OP1.2b (the second part of the TDU campaign, 2018) the overview spectroscopy system was connected to the AEJ51 endoscope.

The overview spectrometer is a set of 5 Czerny-Turner spectrometers mounted in a desktop casing together with a power supply unit and an USB2 hub. The model of the spectrometers is Avantes AVASPEC-ULS2048L-USB2-RM and each in the casing is referenced as a channel or simply chI , where I is number of the channel. The desktop mount is shown in Figure 2.14. Each channel is dedicated to a specific wavelength range:

- ch1 [297 - 459] nm
- ch2 [452 - 590] nm
- ch3 [583 - 698] nm
- ch4 [680 - 889] nm
- ch5 [789 - 1121] nm

2. Edge and divertor diagnostics for impurity characterization at Wendelstein 7-X

Different channels have different sensitivity and for spectral overview it is possible to select different integration times for each of them. Unfortunately, for boronization characterization it was important to get spectra in the full wavelength range synchronized in time which required uniform integration time along channels. For the standard magnetic configuration such a choice provided integration times from 100 ms to 500 ms which was sufficient for the flat top discharges.

The spectral resolution is [0.19 - 0.48] nm. The input of each channel is an SMA adapter and a slit of $25\ \mu\text{m} \times 1\ \text{mm}$. A lens is used to focus the input light onto a CCD line with 2048 pixels of $14\ \mu\text{m} \times 200\ \mu\text{m}$ size.

The channels were connected to a $800\ \mu\text{m}$ WF CeramaOptec 80 m long fibers going from the laboratory into the torus hall of W7-X. In the torus hall these fibers were connected to the next fibers of 5 m length leading directly to the tip of the pyramidal mirror in the detector box of the endoscope.



Figure 2.14: Desktop mount of 5 Avantes AVASPEC-ULC2048L-USB2-RM spectrometers with the power supply and the USB2 hub. Arrows point at the 5 SMA connectors for each channel (spectrometer). 5 free slots could be used for additional spectrometers.

Since the pyramidal mirror is located in front of the focal plane of the endoscopes it provides spectrum for the complete field of view of the endoscope without spatial resolution. 5 central holes of the pyramidal mirror were used for the overview spectrometers optical fibers during OP1.2b.

The field of view (FoV) of the overview spectrometer is shown in Figure 2.15. It corresponds to the position of the first mirror of the endoscopes fixed at 0° and provides information for photon influx spectroscopy by observing the strike line and collecting all photons coming from C and H and from their first ionization stage; in case of B and O their second ionization stage can be tracked. Presence of divertor Langmuir probes in the vicinity of the overview spectrometer's FoV provided unique possibility to characterize impurity influx in the standard, high-mirror and low-iota configurations of W7-X.

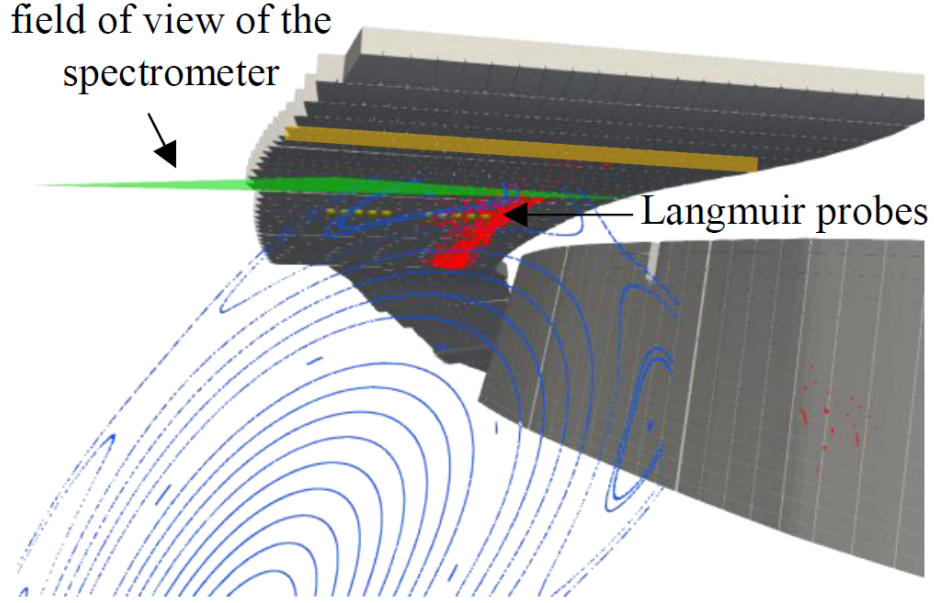


Figure 2.15: Field of view of the overview spectrometer (green) for the standard magnetic configuration of W7-X. The strike-line location is shown only for the magnetic island in the field of view (red, “vacuum” case). The Poincaré map is depicted in blue. Positions of the TDU Langmuir probes are shown in yellow dots. Horizontal and vertical divertor target plates are shown in grey [2].

2.1.5 Endoscope calibration

The new endoscopes for W7-X are highly improved versions of the observation system developed for the TEXTOR tokamak. The procedure of radiometric (absolute) calibration is similar in both cases. Therefore, the corresponding procedure described in [51] has been tuned for the case in hand and is described below.

The goal of radiometric calibration is to get information on how to transform the measured counts in the sensor cells into the photon flux density coming from the specific region of plasma in the machine. That means that we deal with three spaces [51]:

- The object space $V_r \subset \mathbb{R}^3$,
- The sensor space $V_s \subset \mathbb{R}^2$ and
- The image space $V_i \subset \mathbb{Z}^2$

The measured values are denoted as $I(\lambda, \vec{r}_i)$ where \vec{r}_i is:

$$\vec{r}_i = (m\Delta x, n\Delta y) \quad (2.16)$$

$m, n \in \mathbb{Z}$ - column and row number in the image.

In that way values in each pixel (image space) are proportional to the average photon flux density $\langle i(\lambda, \vec{r}_i) \rangle$ following on the sensor (image space). The proportionality coefficient consists of: pixel area $\Delta x \Delta y$, exposure time t_{exp} and the spectral response of the sensor $s_{\text{CCD}}(\lambda)$ - Equation 2.17.

$$I(\lambda, \vec{r}_i) = s_{\text{CCD}}(\lambda) \cdot t_{\text{exp}} \cdot \Delta x \cdot \Delta y \cdot \langle i \rangle (\lambda, \vec{r}_i) \quad (2.17)$$

$$\langle i \rangle (\lambda, \vec{r}_i) = \frac{1}{t_{\text{exp}} \Delta x \Delta y} \int_0^{t_{\text{exp}}} \int_{(m-\frac{1}{2})\Delta x}^{(m+\frac{1}{2})\Delta x} \int_{(n-\frac{1}{2})\Delta y}^{(n+\frac{1}{2})\Delta y} i(\lambda, t, \vec{r}_s) dt dx dy \quad (2.18)$$

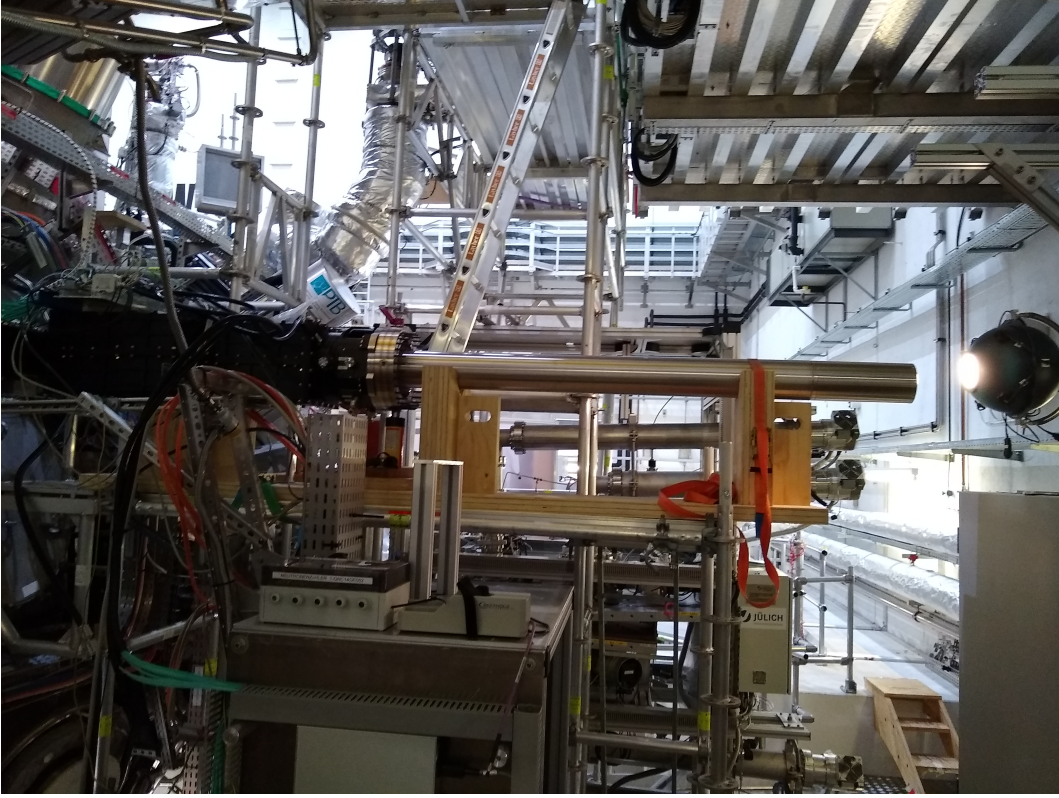


Figure 2.16: Setup of the endoscope for radiometric calibration in the Torus hall of W7-X. The AEJ endoscope can be seen on the left. The complete optical path (including the optical fibers leading to the laboratory) were completely the same as during the experiment. The Ulbricht sphere can be seen on the right and its opening is located in the focal plane of the endoscope.

The $\langle i(\lambda, \vec{r}_i) \rangle$ value is averaged over the exposure time and sensor size after integrating the photon flux density in the sensor space - $i(\lambda, t, \vec{r}_s)$ in Equation 2.18. The value of the latter depends on three parts: the emission of photons in the object space (can be either plasma in the device or another source), the geometrical field of view of the endoscope - so the observation volume $\Delta V(\vec{r}_i)$ imaged on the pixel in the image space with \vec{r}_i and the spectral transmission of the endoscope.

In its turn the emission of photons in the object space or number of the photons emitted per dt from $V(\vec{r}_i)$ can be written as:

$$\frac{\partial N_p(\Delta V(\vec{r}_i))}{\partial t} t_{\text{Pla}} = \Delta \Omega \int_{t_p} \int_{\Delta V(\vec{r}_i)} \epsilon_{p,q}(\vec{r}_r, t) dt dV \quad (2.19)$$

where $\epsilon_{p,q}$ - local plasma emission coefficient for the p→q transition. In this case the grey value at λ_0 at i-th pixel is:

$$GV_{\text{plasma}}(\lambda_0, \vec{r}_i) = s(\lambda_0) \int_{t_{\text{pla}}} \int_{\Delta V(\vec{r}_i)} \epsilon_{p,q}(\vec{r}_r, t) dt dV \quad (2.20)$$

where $s(\lambda_0)$ - spectral response of the system at λ_0 . Since the left hand side of Equation 2.20 is measured by a camera and the space-time integral of the local emission coefficient of the plasma is the desired unknown one would need to know $s(\lambda_0)$, which is constant of the optical system:

$$s(\lambda_0) = S_{\text{CCD}}(\lambda_0) T_{\text{sys}}(\lambda_0) [T_{\text{ND}}(\lambda_0) = 1] \tau(\lambda_0) \Delta \Omega \quad (2.21)$$

In the equation above $T_{\text{sys}}(\lambda_0)$ - transmission of the system at λ_0 , T_{ND} - transmission of the neutral density filter at λ_0 (since no ND filter was used during calibration it = 1), $\tau(\lambda_0)$ - transmission of the interference filter.

It is obvious that $s(\lambda_0)$ can be found with a help of a light source with the known photon emission density and then Equation 2.20 can be solved. An Ulbricht sphere was used as such a source with the known spectral radiance L_λ with the units:

$$[L_\lambda] = \left[\frac{\text{W}}{\text{cm}^2 \cdot \text{sr} \cdot \text{nm}} \right] \quad (2.22)$$

The Ulbricht sphere provided homogeneous emission at its opening. A care was taken that the halogen lamp was powered by an appropriate voltage and current, as stated in its calibration certificate from the corresponding authority. In addition time of lamp usage was below of the values stated as the next re-calibration term.

Now $s(\lambda_0)$ can be written as:

$$s(\lambda_0) = \frac{GV_{\text{cal}}(\lambda_0, \vec{r}_i)}{t_{\text{cal}}} \cdot \frac{E(\lambda_0)}{L_\lambda(\lambda_0)\Delta\lambda_{\text{eff}}(\lambda_0)\Delta A(\vec{r}_i)} \cdot \frac{T_{\text{ND}}(\lambda_0)}{[T_{\text{ND,Cal}}(\lambda_0) = 1]} \quad (2.23)$$

where $\Delta_{\text{eff}}(\lambda_0)$ is an effective transmission of the interference filter at λ_0 , which can be substituted with the FWHM of the interference filter with the central wavelength at λ_0 ; $T_{\text{ND}}(\lambda_0)$ - transmission of the neutral density filter.

Once $s(\lambda_0)$ has been obtained the number of photons from the $\Delta V(\vec{r}_i)$ imaged onto a pixel with measured $GV_p(\lambda_0, \vec{r}_i)$:

$$4\pi \int_{t_p} \int_{\Delta V(\vec{r}_i)} \epsilon_{p,q}(\vec{r}_r, t) dt dV = 4\pi \frac{GV_p(\lambda_0, \vec{r}_i)}{s(\lambda_0)} \quad (2.24)$$

The values of $s(\lambda_0)$ for the AEJ51 endoscope are shown in Figure 2.17:

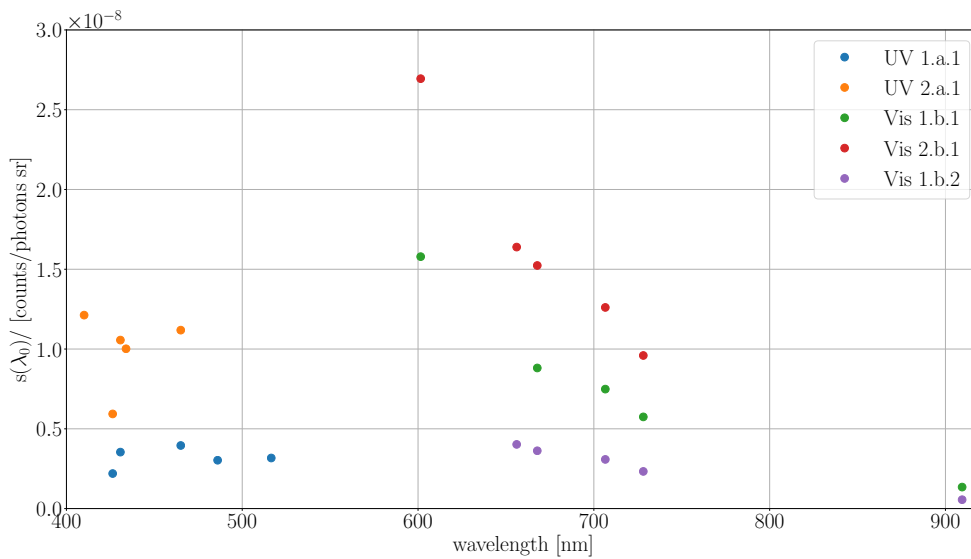


Figure 2.17: $s(\lambda_0)$ - spectral response of the AEJ51 endoscope for all cameras and all narrow band interference filters mounted during OP1.2b of W7-X.

2.2 Edge particle and photon flux measurements

2.2.1 Divertor Langmuir probes

As it will be shown in the section describing the S/XB method for the impurity influx deduction, knowing of the T_e and n_e values at the strike line is essential. A set of Langmuir probes located on the 3rd and the 4th fingers (see Figure 2.18a) was used for this purpose. In the TDU campaign of W7-X the probes [52] were installed in the modules M51 and M30 of the device, which are connected by magnetic field line in the standard magnetic configuration of W7-X (see Figure 2.1, green and blue cross-sections). The initial design predicted their location close to the location of the FZJ endoscopes field of view. Specifically, in this work the values of T_e and n_e obtained with the probe no.10 of the finger no.3 were used to get corresponding values of the S/XB coefficients.

The probes represent a set of graphite tips located in the graphite tiles of W7-X on the same level as the tiles. The tips are biased relatively to the vessel to obtain current-voltage (IU) characteristics. The space between the tip and the tile is filled in with ceramics to isolate the tip from the tile from a possible shortage. The obtained IU-characteristics are than objects to a suitable physics model which fits the data best.

Specifically, at the beginning of the data processing the simple Langmuir (SL) model was used [53], which provided values of T_e reaching up-to ≈ 120 eV which caused a doubt in its correctness, since such high values are not typical for the boundary plasma even at the strike line location. After this new models were investigated in the work cited above and finally a model was selected which fit the experimental data in the best way and this model caused the values of T_e to drop \approx by a factor of 2.

The initial SL model provided:

$$I = I_{sat} \left(1 - \exp\left(-\frac{V - V_f}{T_e}\right) \right) \quad (2.25)$$

$$I_{sat} = A_{coll} J_{sat} = A_{coll} Z n_i e c_s \quad (2.26)$$

$$c_s = \sqrt{\frac{Z T_e + \gamma T_i}{m_i}} \quad (2.27)$$

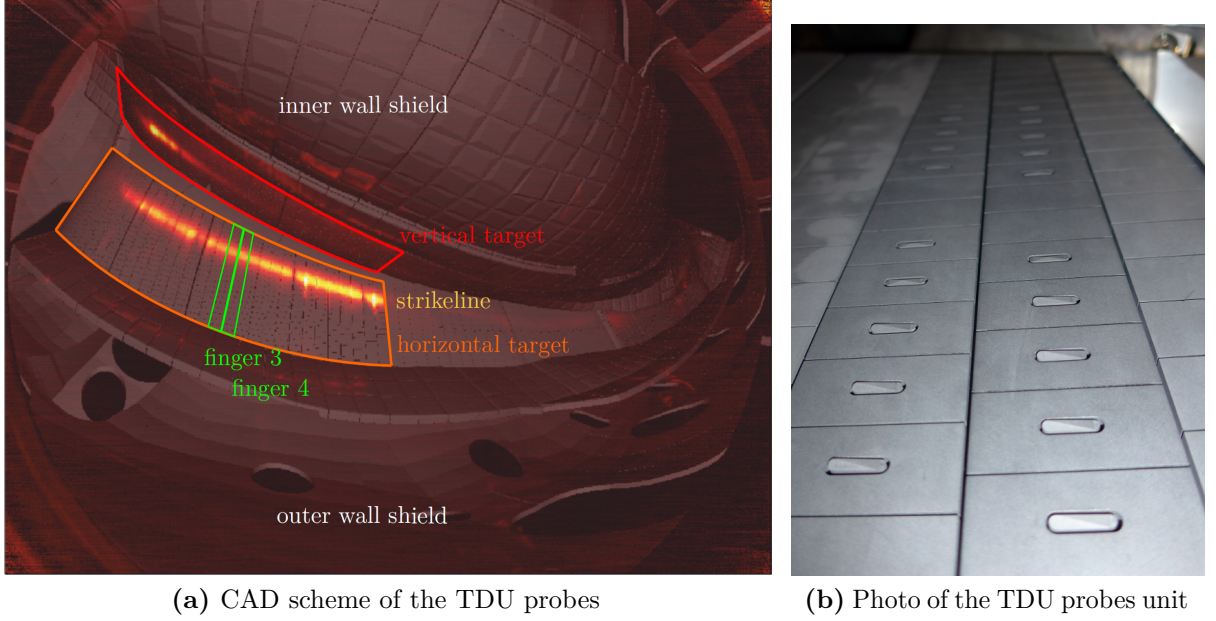


Figure 2.18: TDU probe system at W7-X: a) Image from an infrared camera showing the 3rd and the 4th finger of the horizontal part of TDU where the probes are located. The strike lines are shown in orange; b) Photo of the TDU fingers with the probe tips (taken from [53] and [54]).

where: I_{sat} is the ion saturation current, V is the biasing voltage, V_f is the plasma potential, A_{coll} is the effective collection area, J_{sat} the saturation current density, c_s is the ion sound speed, Z - the ion charge (assumed to be 1 for hydrogen plasmas), m_i - ion mass and $\gamma = 3$ is the coefficient responsible for the adiabatic cooling of the ions.

As explained in [53], the SL could not provide reliable values of T_e mostly due to violated assumption about constant negligible value of the sheath thickness. In the cited work it was shown that the Weinlich-Carlson sheath expansion (WSE) model should be used, since it takes into consideration formation of a pre-sheath with the thickness \approx the ion gyro radius due to the Bohm requirement of the ion speed c_s when they enter the sheath. In this model the predicted sheath thickness is [53]:

$$l_{\text{sheath}} = \frac{l_{\text{norm}}}{12} [(\phi_{\text{pr}}^{3r} - \phi_w^{3r})] + 3(4 - \phi_{\text{De}}^{2r})(\phi_{\text{pr}}^{1r} - \phi_w^{3r}) \quad (2.28)$$

where: ϕ_{pr} , ϕ_w , ϕ_{De} are the dimensionless potentials of the mean probe, the wall and the Debye sheath correspondingly. With this l_{sheath} the collection area was corrected appropriately.

Another important improvement of the initial SL model was introduction of the virtual asymmetric double probe model [53]. The necessity of it comes from the fact that at the presence of magnetic field the volume from which a probe gathers electrons and ions is now limited by a cone. This cone is aligned along the magnetic field and its radius depends on how strong the perpendicular transport is. Therefore, it is necessary to present single probes as virtual double probes which gets significant part of the current from the wall. In practice it meant introduction of an additional fitting parameter β , which is ratio between the area of the electrode to the general characteristics (an effective area A_{coll}) of the double probe. The resulted model was denoted as DWSE, where the D-prefix stands for 'double'.

In the work cited above all different models were compared and it was shown that in terms of the reduced chi-squared $\chi_v^2 \approx 1.7$ the DWSE fits the IU characteristics in

the best way. The first important sign that the model was correct were the values of T_e smaller by \approx a factor of 2 in comparison to the values obtained with the initial approach. In addition a rigorous numerical study was done in [53].

2.2.2 Midplane multipurpose manipulator

In contrast to the divertor measurements with the TDU probes with fixed location the multi-purpose manipulator allows measurements with different R. A changeable probe head allows to choose an optimal configuration for the task at hand. In this work the FZJ combined probe data was used. This probe was equipped with:

- Langmuir pins (P2, P4): $T_e(R)$, $n_e(R)$
- Mach probes: plasma flow velocity
- Compensation coils
- 3D pick up coils: $\vec{B}(R)$ and fluctuations
- Ion sensitive probe: T_i

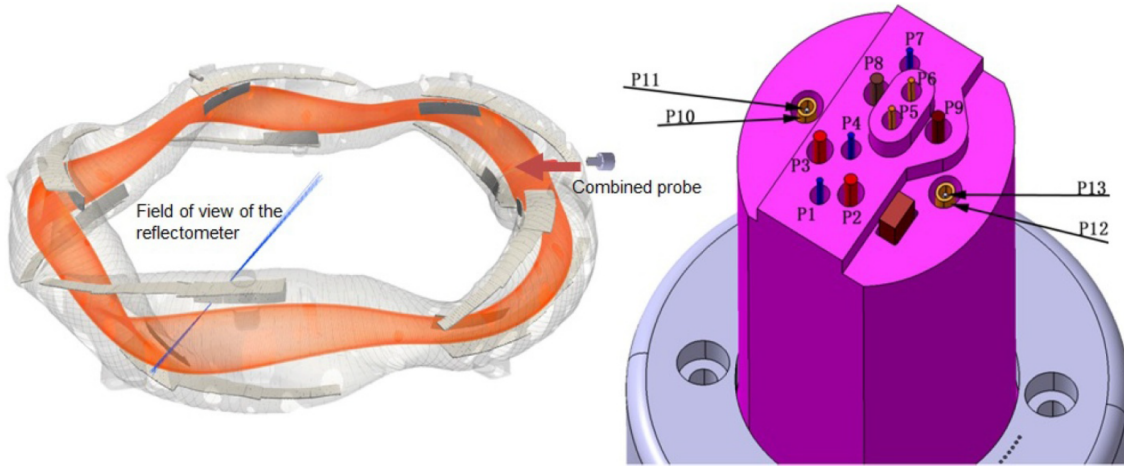


Figure 2.19: Location of the multi-purpose manipulator (MPM) with the combined probe (left). Top view of the combined probe with all the pins numbered. Number of the Langmuir pins are P2 and P4 (modified [55]).

T_e and n_e profiles were measured with the Langmuir pins (P2 and P4 in Figure 2.19) in the triple configuration. T_e was calculated using Equation 2.29 and n_e with Equation 2.30.

$$T_e = \frac{e(U_{pin} - U_{float})}{\ln 2} \quad (2.29)$$

$$n_e = \frac{I_{sat}}{0.49 \cdot e \cdot A_{eff}} \quad (2.30)$$

The assumption included in the calculation is that the effective charge $A_{eff} = 1$.

2.2.3 Filterscopes

The filterscope data was used to obtain photon fluxes of line radiation from different locations at W7-X. The system was firstly used at W7-X for the limiter campaign OP1.1 (December 2015 - March 2016) [56] and it is based on the previously developed one in the Oak Ridge National Laboratory (ORNL) [57]. Later it was successfully applied at various fusion experiments [58], in particular at the TEXTOR tokamak [59].

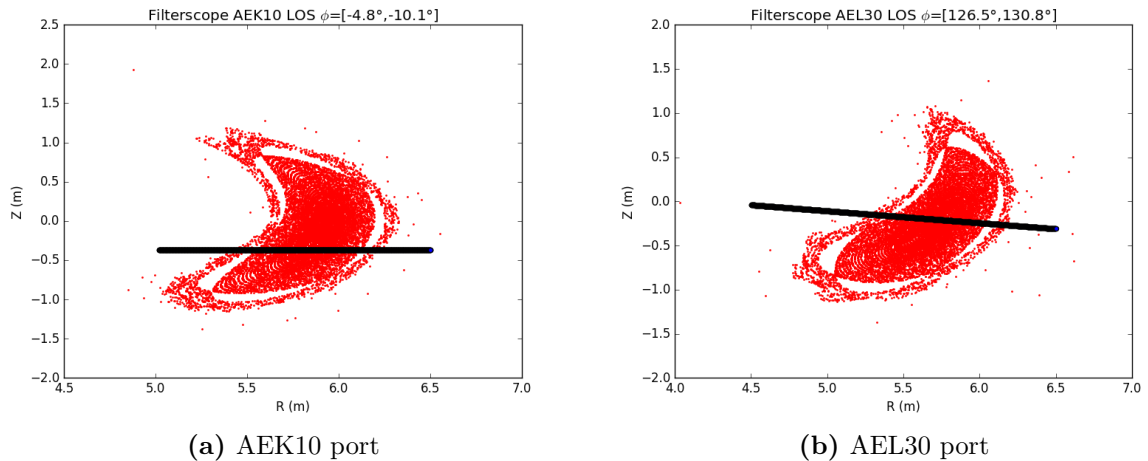


Figure 2.20: Field of view of the filterscope system and the corresponding Poincaré plots for the standard magnetic configuration (taken from [60]).

Visible line emission from the plasma was focused with a help of a lens on the outer side of the port on an optical fiber. The lens was focused at the corresponding surface which was checked with a laser beam to be sharply imaged on the surface. The size of the base of the viewing cone was ≈ 5 cm in all cases. Light was transmitted via the optical fiber to the laboratory where it was split in 4 channels each allowing simultaneous observation of 4 spectral lines of interest with the same field of view. The fiber was connected with a fiber optic bulkhead connector and focused by a lens on a spectral narrow band filter. The filtered line was then detected with a photomultiplier tube (PMT).

In OP1.2b in total 18 lines of sight were available with 14 of them "looking" through the plasma. These remaining 14 lines of sight were looking at different locations around the machine giving 56 PMTs in total. All channels have been absolutely calibrated by placing an Ulbricht sphere 1 m in front of the lens. The transmission of the vacuum window is included later. In case the signal is too strong a neutral density filter was applied.

A wide variety of narrow band filters was available during OP1.2b. $H\alpha$, $H\beta$ and $H\gamma$ hydrogen Balmer line filters were available to study hydrogen recycling. CI, CII, CIII, CIV and CH filters were aimed to study carbon erosion and influx. HeI and HeII filters could be used to deduce He confinement time $\tau_{P,He}^*$ [56]. In addition, ArI, ArII, ArIII and NII lines would allow to study injected impurity behaviour. Finally, BII and OII filters were installed to study wall conditioning. Despite this wide variety of options, only 2 channels had suitable combination of the field of view and the bandwidth filter for the boronization study. Specifically, the field of view from the AEK10 port allowed CIII (C^{2+} , 465.4 nm) and OII (O^+ , 441.9 nm) line emission measurement. This field of view was aiming at the carbon shield. The second field of view was from the AEL30

port and it only allowed the CIII line measurement. The latter field of view was aiming at the stainless steel wall. These situation is shown in Figure 2.20, where the Poincaré maps of the standard magnetic configuration are shown for the vacuum case in red. The black lines are the corresponding fields of view of the used filterscope channels.

2.3 Core impurity measurements

2.3.1 HEXOS

Not only ultra-violet, visible and near infra-red ranges provide all the important information about impurities in a plasma. Extreme ultra-violet range [1 - 200] nm contains important emission lines of the higher ionization stages of impurities. Those include B, C, O and metals coming due to the PSI processes as well as He, Ne, N, Ar coming from external injections for the diagnostic purposes or to study impurity transport in the device. He as a fuel for helium plasma discharges or helium GDC can also be measured.

For the above mentioned purposes the high-efficiency extreme ultra-violet overview spectrometer (HEXOS) data was used at Wendelstein 7-X [61]. The requirement of high intensity and high spectral resolution was reached by the selection of a single reflective diffraction grating as the main optical element to decrease signal losses. The grating is holographic allowing maximum intensity at the 1st order of diffraction together with minimum intensity coming to the higher orders.

The specific measurement range is from 2.5 nm to 160 nm. This range is split into 4 subranges (4 spectrometers) to avoid undesirable effects at the edges of the grating. The field of view of these 4 spectrometers is shown in Figure 2.21 for the basic vacuum magnetic configurations of Wendelstein 7-X: standard (EIM), high-mirror (KJM) and high-iota (FTM). This field of view looks through the complete plasma in the triangular cross-section of W7-X allowing observation of the lower ionization stages of the impurities coming from the near edge region as well as higher ionization stages coming from the hotter regions of plasma. The usage of an MCP (micro channel plate) together with NMOS linear image sensor [62] allowed high operation frequency of the kHz order of the spectrometer.

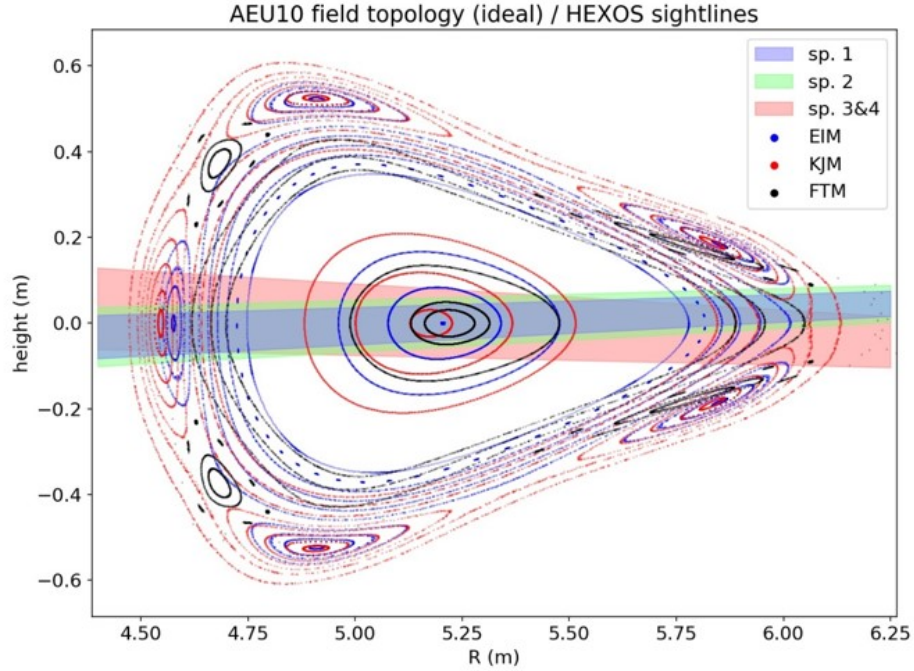


Figure 2.21: Field of view of the HEXOS VUV spectrometer used for the higher ionization stages of the impurities studies (taken from [63]).

2.3.2 Bolometry

To study influence of the impurity line radiation it is important to measure total radiative power of the plasma P_{rad}^{tot} . By knowing this value it is possible to get the change in P_{rad}^{tot} after the boronization and observe time evolution of the radiative fraction f_{rad} , which is:

$$f_{rad} = \frac{P_{rad}^{tot}}{P_{heating}^{tot}}. \quad (2.31)$$

It is of highest interest to know f_{rad} when the plasma density reaches its highest values simultaneously increasing impurity radiation to a point when all power is lost via impurity radiation - so called radiation induced density limit (RIDL).

To measure P_{rad}^{tot} the bolometry system data has been used at W7-X [64]. The future steady-state operation of W7-X requires the system to withstand high thermal heat loads and stray not absorbed radiation from the electron cyclotron resonance heating system. To tackle this issue a metal film resistive sensor is used. It is 4 μm thick with an additional 50 nm layer of carbon coating to improve its absorption in the visible range. Such a configuration allows frequencies up-to 4 kHz which is useful close to RIDL, where f_{rad} increases abruptly.

The bolometry system is located in the triangular poloidal cross-section of W7-X and it consists of two sensors (cameras):

1. Horizontal bolometer camera (HBC) with 32 lines of sight
2. Vertical bolometer camera (VBC) with 40 channels

Such a configuration allows to view the complete plasma cross-section (see Figure 2.22).

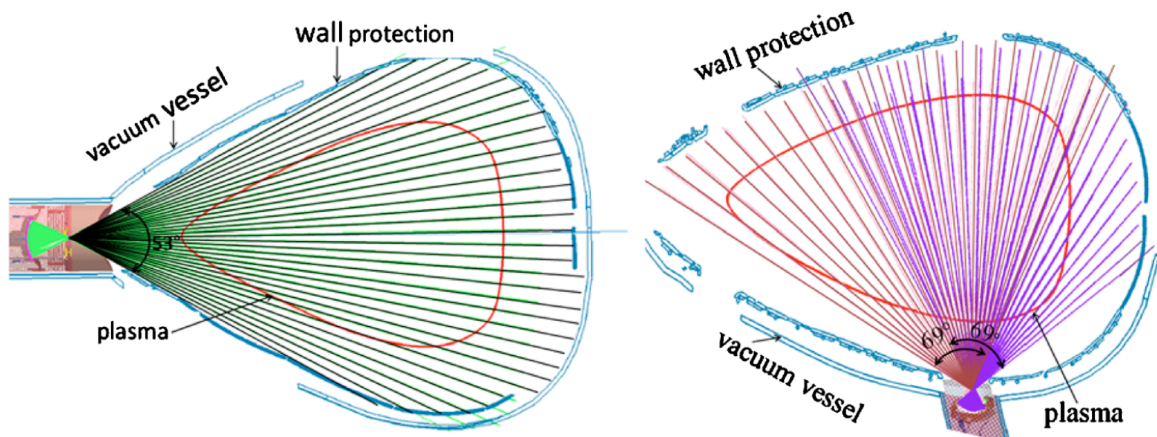
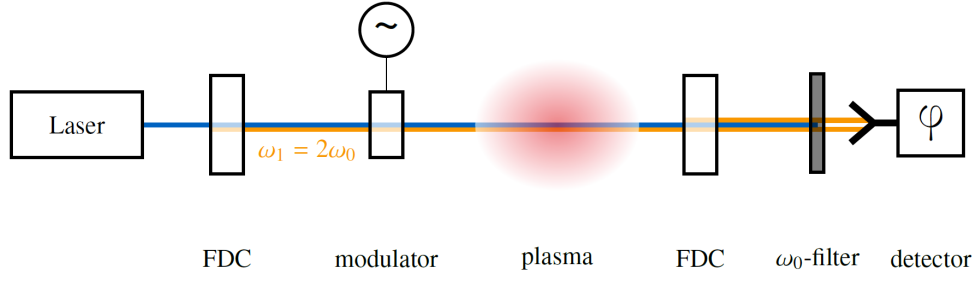


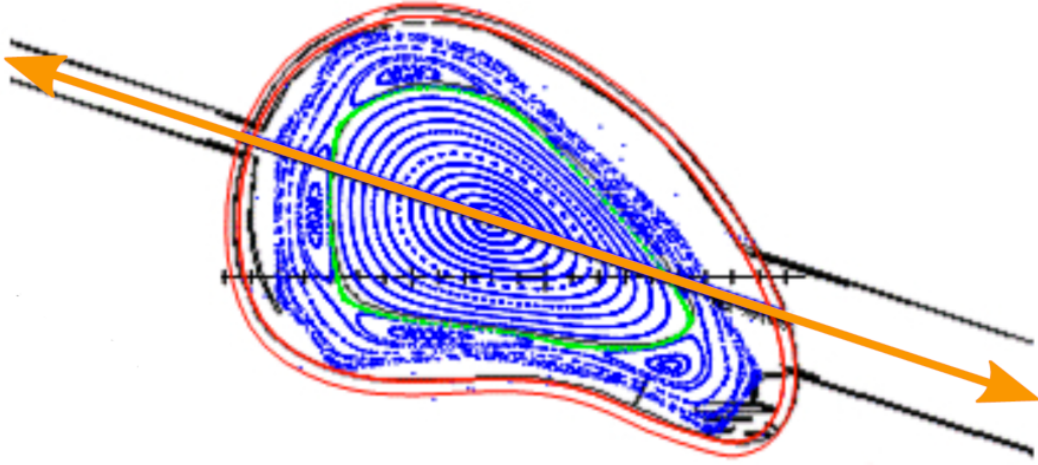
Figure 2.22: Field of view of the bolometry system (taken from [64]). Horizontal bolometer camera (HBC) - left, vertical bolometer camera (VBC) - right.

2.3.3 Dispersion interferometry

The dispersion interferometry (DI) system at W7-X was designed as the main tool for real-time density feedback control. As a result it provided the line-integrated electron density $\int n_e dl$ with high temporal resolution of up-to 50 kHz. The data provided by this system was of highly importance in this work. This method was pioneered on the TEXTOR tokamak [65]. This subsection is based on the work of Brunner et al. [66] dedicated for W7-X's implementation.



(a) Principal scheme of the dispersion interferometer. FDC stands for frequency doubling crystal.



(b) Laser optical path of the dispersion interferometer between the AEZ31 and AET31 ports of W7-X, $\phi = 170.5^\circ$.

Figure 2.23: Dispersion interferometer scheme (taken from [66]).

The basis of the DI system is the dependence of the refractive index of the plasma on its density [66]. The scheme describing the principles of its work is shown in Figure 2.23a. A 20 W CO₂ laser provides continuous light at $\lambda = 10.6 \mu\text{m}$ (frequency ω_0). This light then passes through a frequency doubling crystal (FDC) AgGaSe₂ where a second harmonic $\omega_1 = 2\omega_0$ is generated. Both beams then pass through a modulator and cross the plasma. After the plasma the beams again go through a FDC and the ω_0 part is filtered out. The remaining beams reach the diode detector. The important property of such an optical arrangement is cancellation of the vibrational distortions in the system. Light path of the laser beams is shown in Figure 2.23b in orange, where the right arrow points in the direction to the optical system and the left arrow points to a corner cube reflector, where the beams are reflected. Therefore, they path the plasma twice. For the standard magnetic configuration (vacuum) the length of the plasma region along the beam is ≈ 1.33 m. The resulting signal can then be written as [66]:

$$I_{\text{sig}} = I_1 + I_2 + 2\sqrt{I_1 I_2} \cos(\rho \sin(\omega_m t) + \phi_P), \quad (2.32)$$

where I_1 and I_2 are the intensities of the second harmonic beams generated by the 1st and the 2nd FDCs, ω_m - modulation frequency, ρ - modulation depth and ϕ_P - plasma induced phase shift. The main information on the line-integrated electron density is hidden in ϕ_P , since the refraction index of plasma depends on light wavelength. Taking

into account the refractive index of plasma:

$$n(\omega) = 1 - \frac{2\pi n_e e^2}{m_e \omega^2} \quad (2.33)$$

it was shown in [65] that after obtaining ϕ_P the line-integrated electron density can be obtained from:

$$\phi_P = \frac{e_0^2 \lambda}{4\pi c_0^2 \epsilon_0 m_e} \int n_e(l) dl \quad (2.34)$$

To calculate ϕ_P the cos part of Equation 2.32 was integrated and presented as:

$$\int_0^\pi \cos(\rho \sin(\omega_m t) + \phi_P) d(\omega_m t) = \pi(J_0(\rho) \cos \phi_P + H_0(\rho) \sin \phi_P) \quad (2.35)$$

$$\int_\pi^{2\pi} \cos(\rho \sin(\omega_m t) + \phi_P) d(\omega_m t) = \pi(J_0(\rho) \cos \phi_P - H_0(\rho) \sin \phi_P) \quad (2.36)$$

where J_0 and H_0 are the 0th order Bessel and Struve functions correspondingly. Having the above two integrals it is possible to calculate ϕ_P with the help of inverse tangent function. This function was implemented with the help of field programmable gate arrays (FPGA).

3

Spectroscopy at the divertor region of Wendelstein 7-X

3.1 Photon influx spectroscopy

Emission spectroscopy is one of the most important diagnostic tools for the plasma edge characterization. One of the main advantages is that it is non-perturbative. On the other hand calibration of a set-up might be an issue due to coating of the optical elements during plasma operation or connection issues of an optical fibers. Nevertheless, it is a well established method. Its basis and application for the experimental campaign OP1.2b of W7-X are discussed below.

A spectral line of an element is described by the emission coefficient ϵ . It is the number of emitted photons by a specific transition from excited level i to level k by an element with density n_A^* in the excited state into 4π solid angle:

$$\epsilon = \frac{1}{4\pi} n_A^* A_{ik} \quad (3.1)$$

In this equation A_{ik} is the spontaneous transition probability. With the assumption of equilibrium between electron excitation from the ground state and radiative deexcitation one could write:

$$n_A^* \sum_{k < i} A_{ik} = n_A n_e \langle \sigma_{\text{Exg}} v_e \rangle \quad (3.2)$$

In this case n_A is density of elements in the ground state and $\sum_{k < i} A_{ik}$ is probability of all transition from the level i into lower levels k . $\langle \sigma_{\text{Exg}} v_e \rangle$ is the excitation rate from the ground state into the excited level by electron collisions. If one took n_A^* from the previous equation and substituted it into the result would be:

$$\epsilon = \frac{\Gamma}{4\pi} n_A n_e \langle \sigma_{\text{Exg}} v_e \rangle \quad (3.3)$$

An observable value would be the line integrated intensity:

$$I_{\text{tot}} = h\nu \int_{r_1}^{r_2} \epsilon(r) dr = \Gamma \frac{h\nu}{4\pi} \int_{r_1}^{r_2} n_A(r) n_e(r) \langle \sigma_{\text{Exg}} v_e \rangle dr \quad (3.4)$$

3. Spectroscopy at the divertor region of Wendelstein 7-X

where Γ is the corresponding branching coefficient.

An important step is needed in order to connect particle flux with the observed integrated intensity. Lets assume that the flux of atoms into the plasma $\Phi(r)$ is equal to the number of ionization events. That means all atoms are ionized along the observation path or in the observed volume:

$$\frac{d\Phi_A(r)}{dr} = -\frac{d(n_A v_A)}{dr} = n_A(r)n_e(r) < \sigma_I v_e > \quad (3.5)$$

The integrated value along all attenuation length or over all attenuation volume is:

$$\Phi_A = \int_{r_1}^{r_2} n_A(r)n_e(r) < \sigma_I v_e > dr \quad (3.6)$$

Having Equation 3.4 and Equation 3.6 an equation connecting the observable I_{tot} and the wanted Φ_A can be written:

$$\Phi_A = 4\pi \frac{I_{\text{tot}} \int_{r_1}^{r_2} n_A(r)n_e(r) < \sigma_I v_e > (r) dr}{\Gamma h\nu \int_{r_1}^{r_2} n_A(r)n_e(r) < \sigma_{\text{Exg}} v_e > (r) dr} \quad (3.7)$$

Assuming that the space integrals over $n_A(r)n_e(r)$ have the same form in the nominator and the denominator together with a weak dependence of the excitation rate coefficients Φ_A can be rewritten as:

$$\Phi_A = \frac{4\pi I_{\text{tot}} < \sigma_I v_e >}{\Gamma h\nu < \sigma_{\text{Exg}} v_e >} = 4\pi \frac{I_{\text{tot}}}{h\nu} \frac{S}{XB} \quad (3.8)$$

The $\frac{S}{XB}$ factor is widely noted as S/XB where $S \equiv < \sigma_I v_e >$, $X \equiv < \sigma_{\text{Exg}} > v_e$ and $B \equiv \Gamma$. The S/XB is referred as "ionizations per photon" coefficient.

The S/XB coefficients for different lines of B, C, H and O are functions of T_e and n_e . Therefore, it is valuable to study how the error in determination of the above mentioned values influences the S/XB ratios. In Figure 3.1 ratios of $[S/XB(\text{BII})]/[S/XB(\text{H}_\gamma)]$, $[S/XB(\text{CII})]/[S/XB(\text{H}_\gamma)]$ and $[S/XB(\text{OI})]/[S/XB(\text{H}_\gamma)]$ are shown for the average values of $\langle T_e \rangle = 75 \text{ eV}$ and $\langle n_e \rangle = 7.6 \cdot 10^{18} \text{ m}^{-3}$ with a range of $\pm 5 \text{ eV}$ and $\pm 0.5 \cdot 10^{18} \text{ m}^{-3}$ corresponding to the divertor probes data.

The outcomes are that such a range of error of T_e and n_e result in the biggest error of the normalized boron influx of 13%. The same error for carbon is 10 %. The smallest error is for oxygen: 5 %. The results are positive since oxygen was the main point of interest. Moreover, since n_e and T_e have an inverse dependence on each other a change in one of them would be counteracted by the other one keeping the point of interest in the "dark blue" region in Figure 3.1.

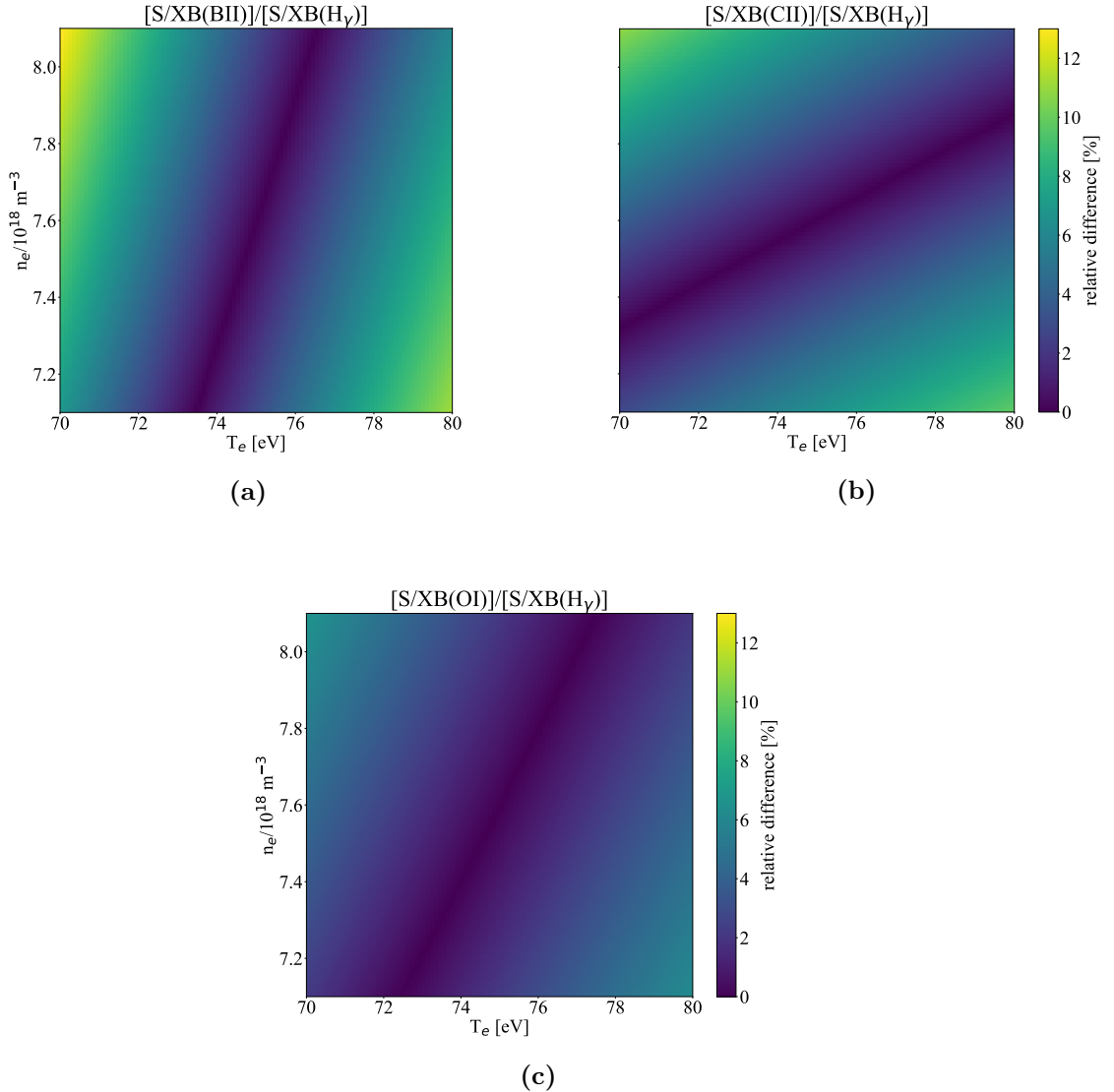


Figure 3.1: Scan of the ratios of the S/XB coefficients around $\langle T_e \rangle = 75$ eV and $\langle n_e \rangle = 7.6 \cdot 10^{18} \text{ m}^{-3}$: a) BII/ H_γ , b) CII/ H_γ , c) OI/ H_γ .

The values of the S/XB coefficients were obtained from [67].

3.2 Helium-beam emission spectroscopy

The reciprocal Langmuir probes require a complicated setup for operation. In addition, the movement of the probe head disturbs the plasma and its operation is frequently complicated. The divertor Langmuir probes measure plasma parameters only at the divertor target and can not provide profiles inside the plasma. Taking the above mentioned limitations of Langmuir probes another method can be used for quick T_e and n_e profiles measurement: helium-beam emission spectroscopy (He-BES).

In He-BES neutral helium is injected into the plasma from, typically, a sequence of nozzles (the Thermal Helium Beam diagnostic during OP1.1 and OP1.2b of W7-X) to allow spatial information measurements. Due to different processes in the plasma the helium atoms get excited and subsequently emit line radiation. These processes can be simulated with the help of collisional-radiative models (CRM) - a system of rate equations for the excited states of helium. Using the solution of CRM together with

3. Spectroscopy at the divertor region of Wendelstein 7-X

the radiative transitions coefficients the emissivity $\epsilon(\vec{r}, T_e, n_e, \lambda)$ of a specific line is obtained. Among different spectral lines 3 are selected. From these 3 lines 2 line-ratios which are sensitive to T_e or n_e are used.

Recently in the work of Zholobenko et al. [68] the corresponding approach has been applied to the case of W7-X and is described in detail below. Additional details can be found in the technical report [69]. Following explanation is based on the work of Zholobenko et al.

The modelling of the He-BES at W7-X was done with the help of the EMC3-EIRENE code. With the help of the 3D EMC3 part the plasma background is defined. That includes 3D grid of T_e , T_i and n_e produced for specific input conditions, like power entering SOL P_{SOL} and electron density at the LCFS n_e^{LCFS} . After this the EIRENE part is used to model the neutral particle transport of the puffed thermal helium particles until they get ionized.

After the solution of the neutral particle transport problem the built in CRM model in EIRENE is used to get the population density of the excited states of He. The system of linear differential equations has the form:

$$\begin{aligned} \frac{dn(p)}{dt} = & - \left(\sum_{q < p} A(p \rightarrow q) + \sum_{q \neq p} C(p \rightarrow q)n_e + S(p)n_e \right) n(p) + \\ & + \sum_{q \neq p} (C(q \rightarrow p)n_e + A(q \rightarrow p)) n(q) + \\ & + (\alpha(p)n_e + \beta(p) + \beta_d(p)) n_i n_e \end{aligned}$$

where:

- $A(p \rightarrow q)$ - the spontaneous transition probability from level p to q
- $C(p \rightarrow q)$ - rate coefficient for electron impact de-excitation from level p to q
- $S(p)$ - rate coefficient for electron impact ionization
- $\alpha(p)$, $\beta(p)$, $\beta_d(p)$ - rate coefficients of the 3-body, radiative and dielectronic recombination
- $n(p)$, $n(q)$ - density of atoms in the p - and q -state

Electron impact excitation and ionization coefficients were updated from the newest cross-sections available. The singlet-triplet mixing of the wave functions was studied and it was shown that for the case of W7-X a constant correction can be included due to small magnetic field at the edge ($B < 3.7$ T). Additionally, dilution of the He-beam due to collisions with p^+ together with transport effects of 2^1S and 2^3S was taken into account.

The solution is $n(\vec{r}, p)$ - population density in state p . Now it is possible to write the expression for volumetric emissivity $\epsilon(\vec{r}, p \rightarrow q)$ - number of photons released per unit volume per unit time for the $p \rightarrow q$ transition:

$$\epsilon(\vec{r}, p \rightarrow q) = n(\vec{r}, p)A(p \rightarrow q) \quad (3.9)$$

The calculated volumetric emissivity can now be used to produce a synthetic image, which is part of the corresponding diagnostics EIRENE module. The photon density

flux $I(\vec{r})$ is:

$$I(\vec{r}) = \frac{1}{4\Pi} \sum_{i=1}^N \epsilon_i \Delta s_i \quad (3.10)$$

where ϵ_i - volumetric emissivity in the i -th cell of the EIRENE grid and Δs_i is the length of the line of sight in that cell.

Among the different transitions 3 of them are widely used to form 2 line intensity ratios which are either sensitive to T_e or n_e :

$$R_{T_e} = \frac{I(728.1 \text{ nm})}{I(706.5 \text{ nm})} \approx \frac{n(3^1S)A(3^1S \rightarrow 2^1P)}{n(3^3S)A(3^3S \rightarrow 2^3S)} \quad (3.11)$$

$$R_{n_e} = \frac{I(667.8 \text{ nm})}{I(728.1 \text{ nm})} \approx \frac{n(3^1D)A(3^1D \rightarrow 2^1P)}{n(3^1S)A(3^1S \rightarrow 2^1P)} \quad (3.12)$$

The used transition are shown in Figure 3.2 together with other He levels for $n \in [1 - 4]$.

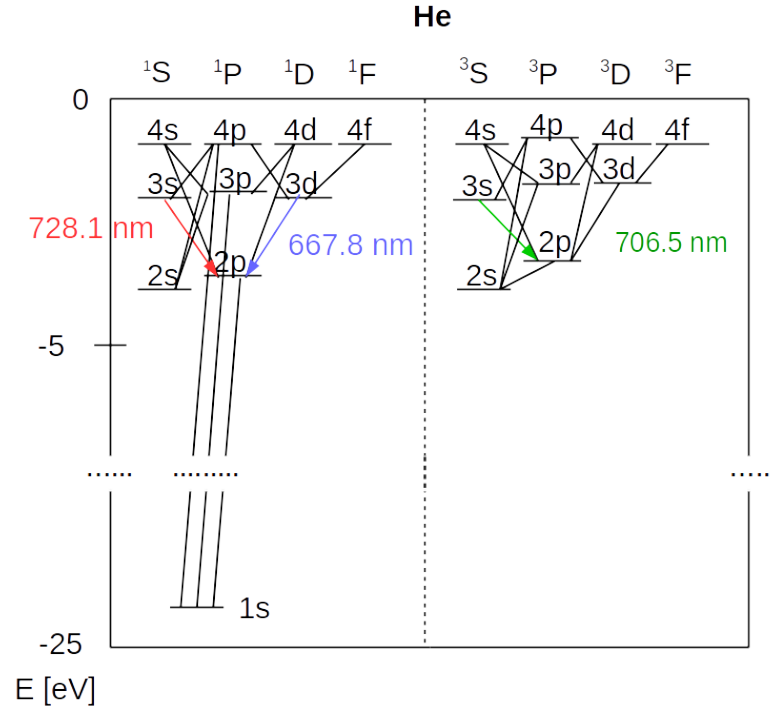


Figure 3.2: He levels for $n \in [1 - 4]$ together with the 3 transitions used in He-BES.

In the above equations the transition from line intensities I to the volumetric emissivity can be done assuming that the radiation is local. Obviously, that might not be very precisely and the correction factor $G(\text{LOS})$ can be used to correct the ratios:

$$G(\text{LOS}) = \frac{\int \epsilon_1(s) ds}{\int \epsilon_2(s) ds} \left(\frac{1}{\int ds} \int \frac{\epsilon_1(s)}{\epsilon_2(s)} ds \right) \quad (3.13)$$

Therefore, the experimentally measured line intensities can be compared with the modelling results. By including different processes it is possible to get understanding of

3. Spectroscopy at the divertor region of Wendelstein 7-X

all processes in the plasma and obtain T_e and n_e profiles. Such a precise comparison requires significant effort and is only suitable for dedicated discharges.

For faster, but less precise values of T_e and n_e the measured line-ratios are compared to the contour plots of the ratios as functions of T_e and n_e . Then the point on the contour map is found by minimization of:

$$D(T_e, n_e) = \sum_{T_e, n_e} \left(1 - \frac{R_{T_e, n_e}^{\text{measured}}}{R(T_e, n_e)_{T_e, n_e}^{\text{modelled}}} \right)^2 \quad (3.14)$$

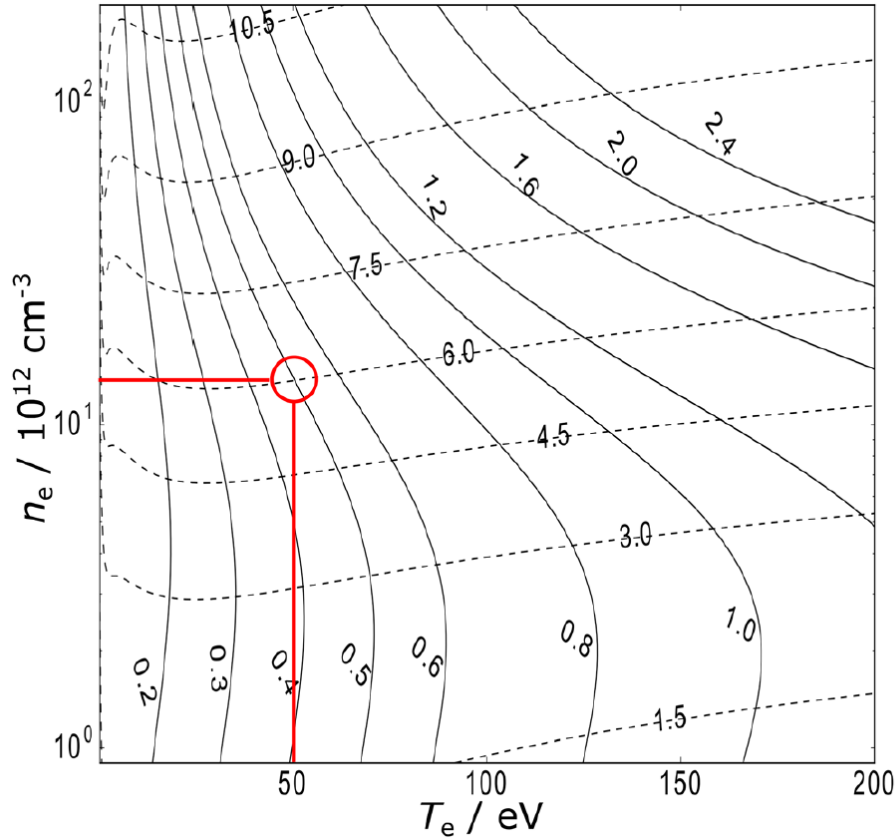
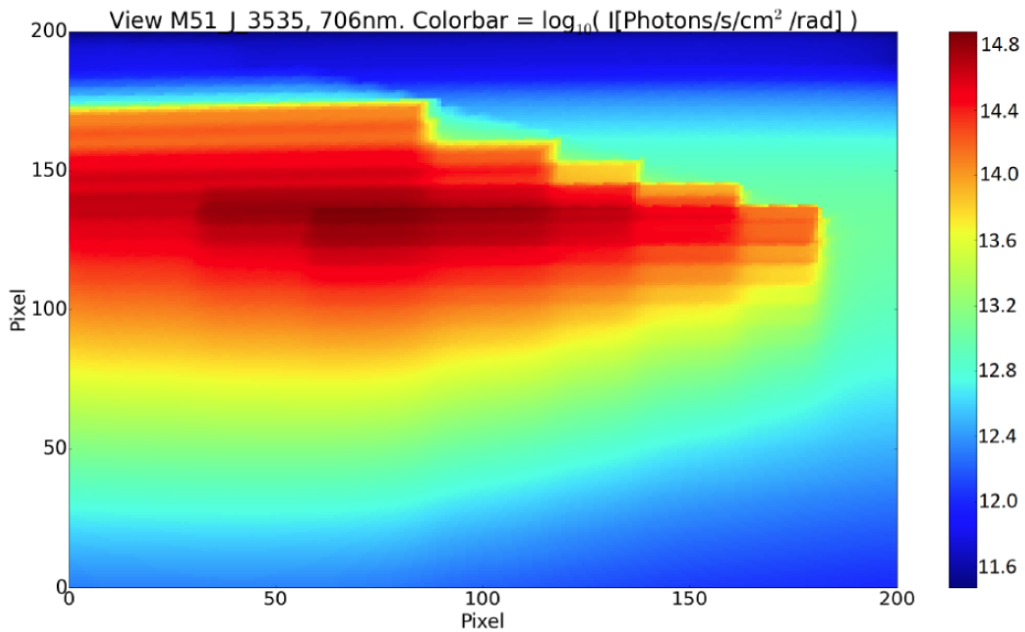


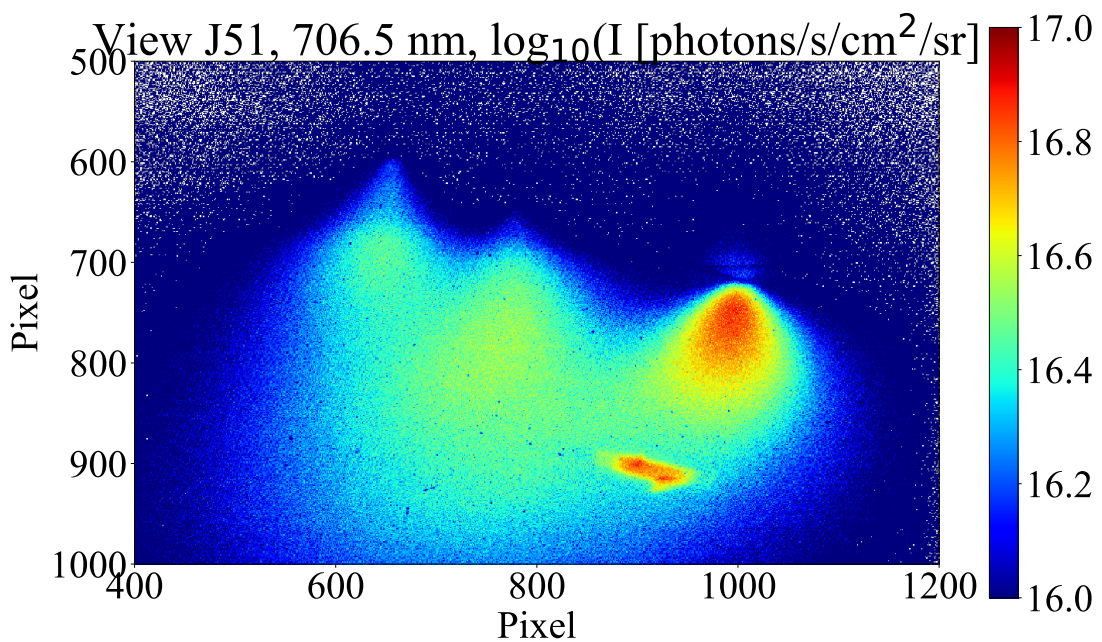
Figure 3.3: Emissivity ratios calculated with the updated version of the CR model in the work of Zholobenko et al. The results are shown for the not metastable resolved case. The solid line corresponds to R_{T_e} and the dashed line to R_{n_e} . The red mark illustrates result of minimization of 3.14 and the corresponding values of T_e and n_e (taken from [69]).

The point found for such a minimization is shown in Figure 3.3 with a red circle. Then the values of T_e and n_e are shown with red lines projections on corresponding axis.

In the work of Zholobenko et al. [69] an artificial image for the 706.5 nm HeI line emission is given for a W7-X discharge in the standard magnetic configuration, what is shown in Figure 3.4a. The image is simulated for the $P_{\text{SOL}}=10$ MW, $\langle n_e \rangle_{\text{LCFS}} = 5 \cdot 10^{19} \text{ m}^{-3}$ (electron density at LCFS) edge plasma parameters.



(a) Artificial camera image of the 706.5 nm line of HeI for a W7-X discharge in the standard magnetic configuration as obtained by the diagnostics module of EIRENE. $P_{\text{SOL}}=10$ MW, $\langle n_e \rangle_{\text{LCFS}} = 5 \cdot 10^{19} \text{ m}^{-3}$ (taken from [69]).



(b) A composite image of a sequence of helium puffs from the 3 (2nd, 3rd and 5th) nozzles at the M51 module of W7-X for the 20181010.021 discharge.

Figure 3.4: Comparison of the artificial camera image of a simultaneous helium puff from the all 5 divertor nozzles in the M51 module of W7-X with the measured helium puff during the 20181010.021 discharge of W7-X.

Figure 3.4b shows a similar measurement during the 20181010.021 discharge in the standard magnetic configuration of W7-X as a composite image of 3 separate puffs from

the 2nd, 3rd and 5th) nozzles in the M51 module for the 706.5 nm HeI line. The value of $\langle n_e \rangle_{\text{LCFS}} \approx 5 \cdot 10^{19} \text{ m}^{-3}$.

A significant difference can be seen between 2 figures. Unfortunately, the developed modelling code was not available for the scan of the plasma background parameters. The edge parameters during the modelling do not correspond to those during the measurement. A further investigation should be done in future once an access to the developed code is restored by the responsible scientist in the modelling group.

3.3 Identified spectra

The 5-channel overview Avantes spectrometer provided the best available overview spectra allowing simultaneous observation of all fuel and impurity emission lines in the wide wavelength range. In the next experimental campaigns the endoscopes system is aiming at observation of different impurity lines, including B, C, O, Ar, N, Ne. In addition, He will be used for the T_e and n_e profiles calculation. Since the narrow band interference filters have an FWHM $\approx 1.5 \text{ nm}$ it is extremely important to monitor the vicinity of the central wavelength of the filters for parasitic emission of other impurities.

Furthermore, as will be shown in Chapter 5, the capabilities and the configuration overview spectrometer were enough to characterize influence of boronizations on B, C and O influx. Therefore, this subsection will be devoted for the recycling impurities Ar, He, N, Ne and B, C, O spectra are discussed with more focus in Chapter 5.

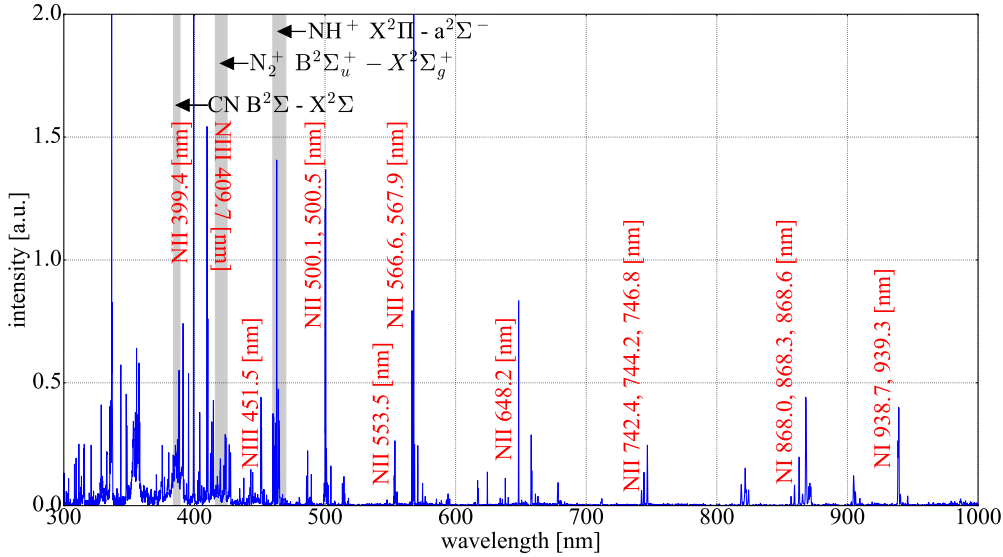


Figure 3.5: Emission spectra of different ionization stages of N together with the expected ranges of the molecular bands. The spectra were obtained with the overview spectrometer for the 20180920.050 discharge of W7-X in the standard magnetic configuration. N_2 was injected from the divertor nozzles (number 4 and 2) in the M51 module. The spectra without N_2 puffing was subtracted from the one during puffing to obtain only the lines and bands of interest.

In Figure 3.5 a spectra of different ionization stages of N is shown for the range of wavelengths [300 - 1000] nm. The spectra has been obtained during a N seeding experiment when N_2 was puffed in via the divertor puffing system (Thermal Helium Beam diagnostic) through the 4th and 2nd nozzles during the 20180920.050 discharge

in the standard magnetic configuration. The most intensive lines are at 399.4 nm for the $2s^2 2p 3p \ ^1D \rightarrow 2s^2 2p 3s \ ^1P^\circ$ transition and at 566.6 nm with 567.7 nm for $2s^2 2p 3p \ ^3D \rightarrow 2s^2 2p 3s \ ^3P^\circ$. These lines could be used in the filter cameras for N observation. The summary of the observed N lines is given in Table 3.1.

In addition to the atomic lines a couple of molecular bands were observed previously at JET [70]. N_2^+ band at $\approx [416 - 425]$ nm for the $B^2\Sigma_u^+ - X^2\Sigma_g^+$ transitions would be observable if the puffed in N_2 molecules could travel significant distance into the plasma before ionization. Although N_2 was puffed in the view of the overview spectrometer this band was not observed giving a hint that N_2 molecules are quickly dissociated. The NH^+ molecule band for the $X^2\Pi - a^2\Sigma^-$ transition is located at $\approx [460 - 470]$ nm. This band comes from the reactivity of N with H, but it has also not been observed by the overview spectrometer. This advises that N_2 and N didn't react with H.

In contrast to the previous bands the CN molecule band at $\approx [384 - 389]$ nm for the $B^2\Sigma - X^2\Sigma$ transition was observable by the overview spectrometer. This indicates presence of chemical erosion of C by N [70]. Nevertheless, the sensitivity and resolution of the overview spectrometer is not sufficient for quantitative analysis of the process. A high resolution spectrometer is needed to study this question in the future.

Line	Transition	wavelength [nm]
N II	$2s^2 2p 3p \ ^1D \rightarrow 2s^2 2p 3s \ ^1P^\circ$	399.4
N III	$2s^2 3p \ 2P^\circ \rightarrow 2s^2 3s \ 2S$	409.7
N III	$2s 2p(^3P^\circ) 3p^4D \rightarrow 2s 2p(^3P^\circ) 3s^4P^\circ$	451.5
N II	$2s^2 2p 3d \ ^3F^\circ \rightarrow 2s^2 2p 3p \ ^3D$	500.1, 500.5
N II	$2s 2p^2(^4P) 3p \ ^5D^\circ \rightarrow 2s 2p^2(^4P) 3s \ ^5P$	553.5
N II	$2s^2 2p 3p \ ^3D \rightarrow 2s^2 2p 3s \ ^3P^\circ$	566.6, 567.9
N II	$2s^2 2p 3p \ ^1P \rightarrow 2s^2 2p 3s \ ^1P^\circ$	648.2
N I	$2s^2 2p^2(^3P) 3p \ ^4S^\circ \rightarrow 2s^2 2p^2(^3P) 3s \ ^4P^\circ$	742.4, 744.2, 746.8
N I	$2s^2 2p^2(^3P) 3p \ ^4D^\circ \rightarrow 2s^2 2p^2(^3P) 3s \ ^4P$	868.0, 868.3, 868.6
N I	$2s^2 2p^2(^3P) 3p \ ^2D^\circ \rightarrow 2s^2 2p^2(^3P) 3s \ ^2P$	938.7, 939.3

Table 3.1: List of the identified N lines in the H plasma of W7-X in OP1.2b during a N injection.

3. Spectroscopy at the divertor region of Wendelstein 7-X

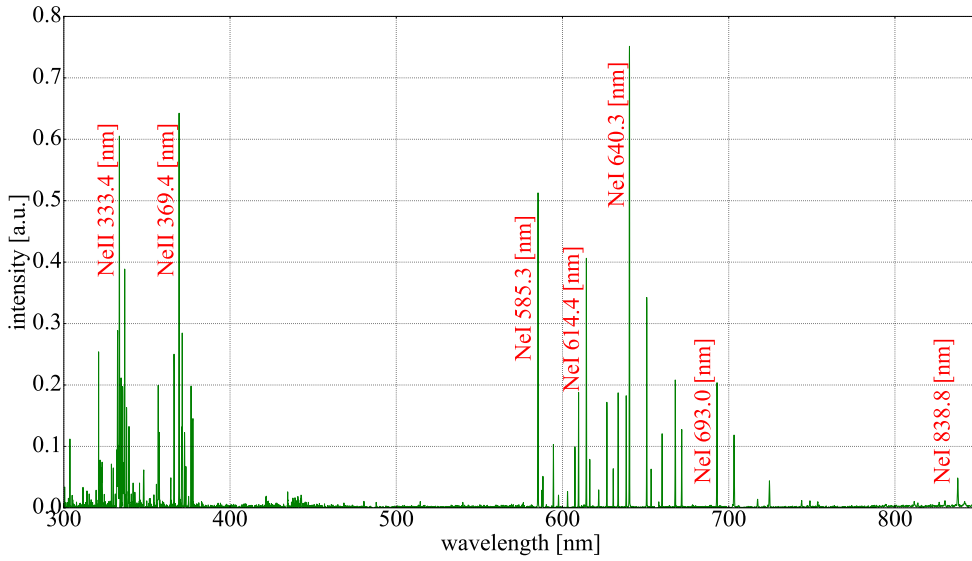


Figure 3.6: Emission spectra of Ne obtained with the overview spectrometer for the 20180920.040 discharge of W7-X. Ne was injected from the divertor nozzles in the M51 module. The spectra without Ne puffing was subtracted from the one during puffing to obtain only the Ne lines.

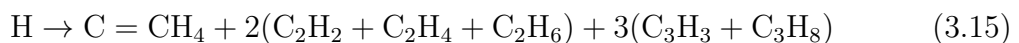
Line	Transition	wavelength [nm]
Ne II	$2s^2 2p^4(^3P) 3p^4 D^\circ \rightarrow 2s^2 2p^4(^3P) 3s^4 P$	333.4
Ne II	$2s^2 2p^4(^3P) 3p^4 P^\circ \rightarrow 2s^2 2p^4(^3P) 3s^4 P$	369.4
Ne I	$2s^2 2p^5(^2P_{1/2}^\circ) 3p^2[1/2] \rightarrow 2s^2 2p^5(^2P_{1/2}^\circ) 3s^2[1/2]^\circ$	585.3
Ne I	$2s^2 2p^5(^2P_{3/2}^\circ) 3p^2[3/2] \rightarrow 2s^2 2p^5(^2P_{3/2}^\circ) 3s^2[3/2]^\circ$	614.4
Ne I	$2s^2 2p^5(^2P_{3/2}^\circ) 3p^2[5/2] \rightarrow 2s^2 2p^5(^2P_{3/2}^\circ) 3s^2[3/2]^\circ$	640.3
Ne I	$2s^2 2p^5(^2P_{3/2}^\circ) 3p^2[3/2] \rightarrow 2s^2 2p^5(^2P_{1/2}^\circ) 3s^2[1/2]^\circ$	693.0
Ne I	$2s^2 2p^5(^2P_{3/2}^\circ) 3p^2[7/2] \rightarrow 2s^2 2p^5(^2P_{3/2}^\circ) 3s^2[5/2]^\circ$	838.8

Table 3.2: List of the identified Ne in the H plasma of Wendelstein 7-X in OP1.2b during a Ne injection.

Neon spectra are important for the impurity seeding studies. Among the other lines the NeI lines at 585.3 nm and 640.3 nm are the most intensive lines of NeI (see Figure 3.6 and Table 3.2). The 333.4 nm and 369.4 nm lines are suitable for NeII measurements. No problem related to the line overlap with other impurities or fuel has been detected.

The spectra of carbon are specifically important for PSI studies, since W7-X is equipped with a graphite divertor. A typical spectrum is shown in Figure 3.7, which was obtained for the 20180920.013 discharge when methane was puffed in the field of view of the overview spectrometer.

In addition to the C and C^{+N} (N stands for the degree of ionization) lines (given in Figure 3.7 and Table 3.3) a couple of molecular bands provide important information about composition of the re-eroded layer. The chemical erosion of carbon by hydrogen contains a couple of products:



The above given molecules dissociate and emission of the molecular bands from the dissociation products can be measured. The CH Gerö band ([425 - 430] nm) comes from methane molecules, the C₂ Swan molecular band ([515-517] nm) comes from the ethane molecules and the C₃ band (405 nm) comes from the propane molecules. The corresponding transitions are shown in Figure 3.7.

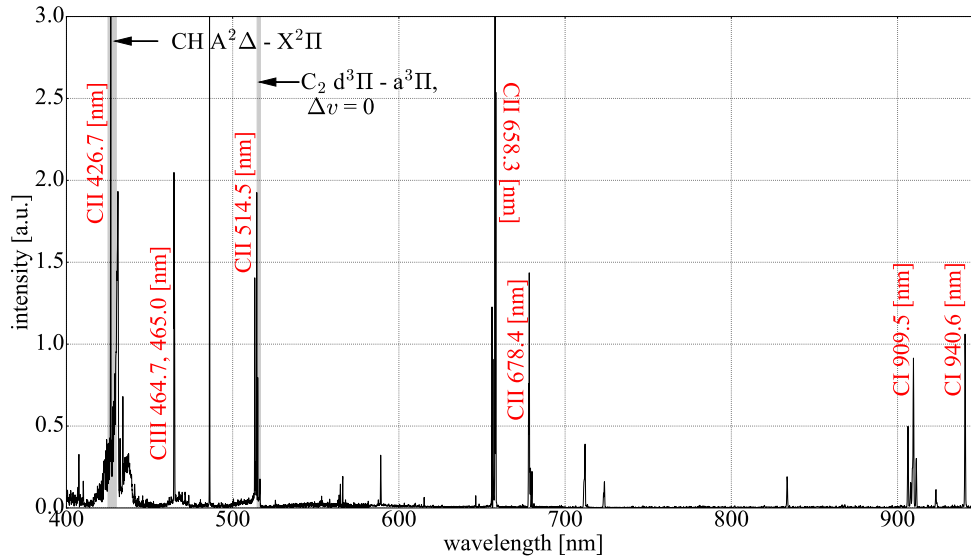


Figure 3.7: Emission spectra of C obtained with the overview spectrometer for the 20180920.013 discharge of W7-X. CH₄ was injected from the divertor nozzles in the M51 module. The spectra without methane puffing was subtracted from the one during puffing to obtain only the C lines.

By measuring the C₂ and CH bands it is possible to study re-deposition of the eroded layers. In [71] these spectra were measured at the JET tokamak with carbon divertor targets during a strike line sweep. The presence of these bands was related to chemical erosion of a soft a-C:H layer. Sweeping provided scanning of the divertor target and gave information on gross erosion and re-deposition zones. Unfortunately, such measurements were not possible in the frame of this work, since only the overview spectrometer was available.

3. Spectroscopy at the divertor region of Wendelstein 7-X

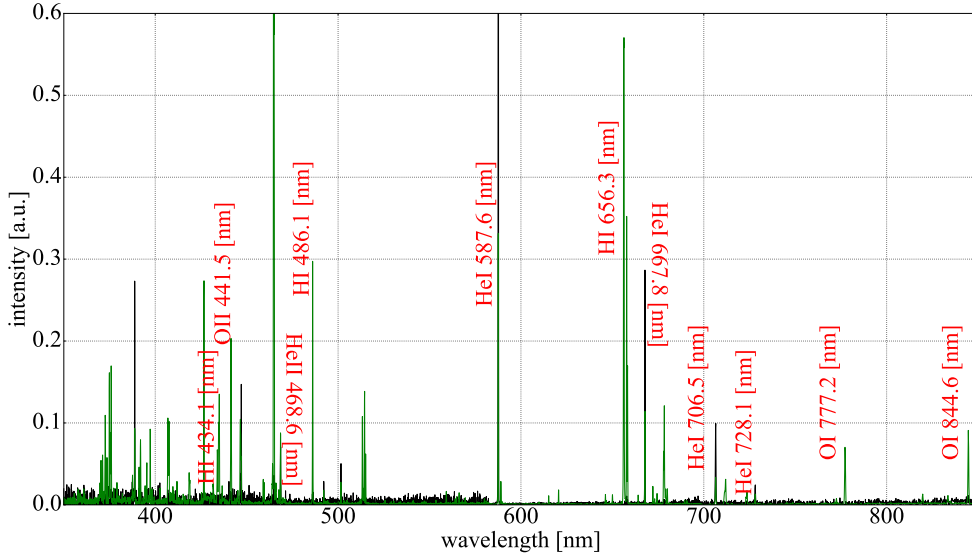


Figure 3.8: Emission spectra of He, H and O obtained with the overview spectrometer for the 20180801.022 and 20181010.022 discharges of W7-X. The He spectrum (black part) was obtained by injection from the divertor nozzles in the M51 module. The spectra without He puffing was subtracted from the one during puffing to obtain only the He lines. The complete spectrum for 20180801.022 was added afterwards.

Line	Transition	wavelength [nm]
C II	$2s^24f \ ^2F^\circ \rightarrow 2s^23d \ ^2D$	426.7
H I (H_γ)	$5 \rightarrow 2$	434.1
O II	$2s^22p^2(^3P)3p \ ^2D^\circ \rightarrow 2s^22p^2(^3P)3s \ ^2P$	441.5
C III	$1s^22s3p \ ^3P^\circ \rightarrow 1s^22s3s \ ^3S$	464.7, 465.0
He II	$4 \rightarrow 3$	468.6
H I (H_β)	$4 \rightarrow 2$	486.1
C II	$2s2p(^3P^\circ)3p \ ^4P \rightarrow 2s2p(^3P^\circ)3s \ ^4P^\circ$	514.5
He I	$1s3d \ ^3D \rightarrow 1s2p \ ^3P^\circ$	587.6
H I (H_α)	$3 \rightarrow 2$	656.3
C II	$2s^23p \ ^2P^\circ \rightarrow 2s^23s \ ^2S$	658.3
He I	$1s3d \ ^1D \rightarrow 1s2p \ ^1P^\circ$	667.8
C II	$2s2p(^3P^\circ)3p \ ^4D \rightarrow 2s2p(^3P^\circ)3s \ ^4P^\circ$	678.4
He I	$1s3s \ ^3S \rightarrow 1s2p \ ^3P^\circ$	706.5
He I	$1s3s \ ^1S \rightarrow 1s2p \ ^1P^\circ$	728.1
O I	$2s^22p^3(^4S^\circ)3p \ ^5P \rightarrow 2s^22p^3(^4S^\circ)3s \ ^5S^\circ$	777.2
O I	$2s^22p^3(^4S^\circ)3p \ ^3P \rightarrow 2s^22p^3(^4S^\circ)3s \ ^3S^\circ$	844.6
C I	$2s^22p3p \ ^3P \rightarrow 2s^22p3s \ ^3P^\circ$	909.5
C I	$2s^22p3p \ ^1D \rightarrow 2s^22p3s \ ^1P^\circ$	940.6

Table 3.3: List of the identified intrinsic lines in the H plasma of W7-X in OP1.2b before boronization.

An overview of the spectra of the main impurity before boronization - oxygen, together with helium and hydrogen are shown in Figure 3.8 and Table 3.3. The spectra in Figure 3.8 was obtained by adding a spectrum during a He puff and a normal discharge before boronization.

The most important lines of oxygen are OI lines at 777.2 nm and 844.6 nm which can be used for the photon influx spectroscopy measurements. The other strong line of oxygen is the OII line at 441.5 nm. The main 3 lines of HeI for the helium line ratio method are shown with the weakest intensity of the 728.1 nm line. The Balmer lines of hydrogen are shown for the α line 656.3 nm, β at 486.1 nm and γ at 434.1 nm.

Although before boronization the device had a high oxygen content, which caused chemical erosion of carbon with CO and CO₂ production, no molecular bands were detected before boronization with the overview spectrometer. In [72] detailed information can be found on the CO, CO₂, CO⁺, CO₂⁺ molecular bands spectra. The strongest band of CO is the Angström band: B ¹Σ - A ¹Π with the band heads in the visible range. Observation of the CO⁺ are even more complicated to detect since the band heads are located in the UV range and the UV spectrometer of the endoscope is needed. The CO₂ bands are in principle problematic to observe in the visible and UV ranges, since the molecule is transparent in those ranges. The CO₂⁺ molecule has the strongest Fox, Duffendack and Barker's system A ²Π - X ²Π with the head at 416.0 nm. It seems to be detectable by the overview spectrometer, but for any analysis a higher resolution spectrometer is needed, which will be available in the next experimental campaign of W7-X.

The molecular spectra of different B molecules could also provide information on the boronization mechanisms and B erosion. For the BH molecule the most intensive are 3 systems: A ¹Π - X ²Π (433.2 nm), b ³Σ - a ³Π (366.2 nm), B ¹Σ⁺ - A ¹Π (341.5 nm). Only signs of the first band were seen in the spectra immediately after the first boronization. The ²Π - ²Σ of BH⁺ at 434.0 nm overlaps with H_γ line of boron and is neither detectable nor usable. For the BO molecule the A ²Π - X ²Σ is one of the strongest. The 616.5 nm head was observable, but due to the low resolution it was only observed right after boronization.

As a summary of CO, CO₂, CO⁺, CO₂⁺, BH, BH⁺ and BO molecular spectra: their bands are either not observable or very weak as measured by the overview spectrometer. In the next experimental campaign of W7-X the high resolution spectrometers should be used to search for this spectra. By applying strike line sweep and rotation of the first mirror of the endoscope it might be possible to obtain important information on the PSI processes.

More details on B, C and O spectra can be found in the laboratory report for spectral studies at ASDEX [73]. In [74] a spectral study during OP1.2a has been done with additional information on analytical approach on T_e determination from line ratios of recycling He.

3.4 2D tomographic reconstruction of emission profiles

Emissivity profiles of the fuel and impurities are of high interest at W7-X. Specifically, 2D emissivity profiles of H, O, C, B, Ar, He, Ne and N can provide important information on plasma background. By comparing these profiles with simulation results it is possible to better understand the mechanism of the impurity transport and the plasma-surface interactions. The improved simulations then could be used to predict the consequences of long pulse operation at W7-X and make operation optimizations etc.

Among other methods optical observations systems provide information about the plasma without perturbing it. Having corresponding atomic system models important

3. Spectroscopy at the divertor region of Wendelstein 7-X

plasma parameters can be obtained. With the help of cameras 2D profiles can be easily measured. Unfortunately, these 2D profiles are line integrated - the signal at each pixel of the sensor is an integral of emission along a line of sight going through different plasma regions with different plasma parameters. The line integration results in disturbed data in position, size and shape of the emission profile. It is the task of tomography to resolve this issue and provide, in this case, 2D profiles in a poloidal cross section.

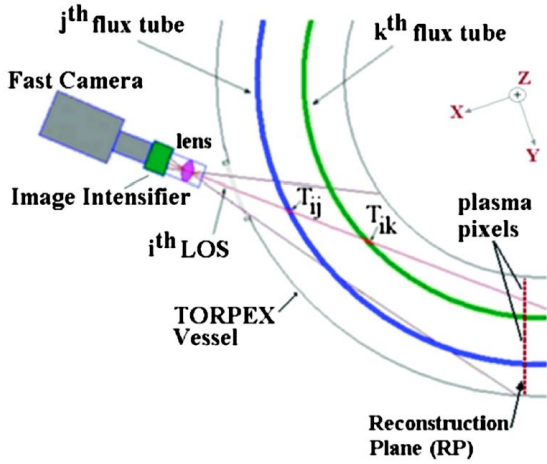
A camera sensor provides an image which is a 2D matrix of brightness \mathbf{I} coming as a result of integration of the emissivity of the plasma \mathbf{g} along a line of sight (LOS). It is an obvious idea (as it was also shown in [75]) to divide a poloidal cross section of the plasma into "plasma pixels". In that case the emissivity of each plasma pixel is denoted as g_j , where $j \in [1 - M]$ with M - number of "plasma pixels". Each "plasma pixel" corresponds to a specific flux tube, which means that every LOS crosses those flux tubes with a specific length T_{ij} (see Figure 3.9a). Assuming that every flux tube has constant emissivity, brightness at each camera pixel can be written as:

$$I_i = \sum_{j=1}^M T_{ij} g_j, \quad (3.16)$$

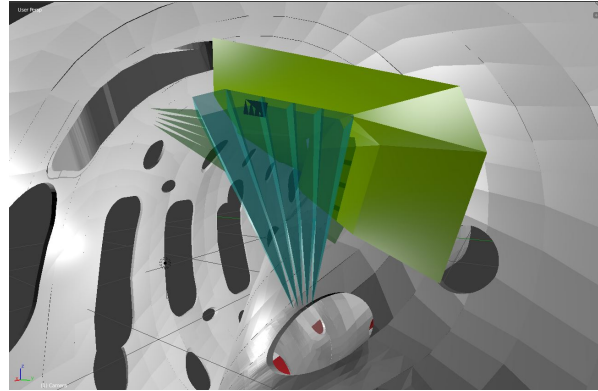
where N - number of camera pixels. In the matrix form Equation 3.16 can be rewritten as:

$$\mathbf{I} = \mathbf{T}\mathbf{g} \quad (3.17)$$

In Equation 3.17 the unknown value is \mathbf{g} - the main goal of tomography. The values of \mathbf{I} are measured and the transfer matrix \mathbf{T} is known for each field of view.



(a) Basics of the tomographic reconstruction (taken from [75]).



(b) Additional fields of view due to the endoscopes' first mirror rotation.

Figure 3.9: Main basics of the tomographic reconstruction: a) Brightness of the image pixels \mathbf{I} as product of the transfer matrix \mathbf{T} and the emissivity profile \mathbf{g} , view in the toroidal cross section, b) Additional fields of view due to the rotation of the first mirror of the J and L 51 endoscopes, poloidal cross section view.

Now the task is to solve Equation 3.17, which is a system of linear algebraic equations (SLAE). Numerically this means to find such \mathbf{g} that the residual square $R^2 \rightarrow 0$, where R^2 is defined as [75]:

$$R^2 = (\mathbf{I} - \mathbf{T}\mathbf{g})^T (\mathbf{I} + \mathbf{T}\mathbf{g}) \quad (3.18)$$

Depending on the ratio between M and N the system is characterized as:

- $M < N$ - underdetermined
- $M \geq N$ - overdetermined

In case SLAE is underdetermined $R^2 = 0$ and there exist infinite number of solutions. In this case the solution can be selected with the help of different methods [75]:

- linear or Philipps-Tikhonov regularizations
- Cormack inversion
- maximum entropy
- minimum Fisher information

In our case the system is overdetermined which allows to find a stable solution by least squares fitting. Specifically, singular value decomposition (SVD) method is used. This method had been used before on the JET tokamak [76]. By using SVD the transfer matrix \mathbf{T} in Equation 3.17 can be decomposed in:

$$\mathbf{T} = \mathbf{U}\mathbf{D}\mathbf{V}^*, \quad (3.19)$$

where:

- \mathbf{U} , \mathbf{V} - unitary matrices, so $\mathbf{U}^{-1}=\mathbf{U}^*$ and $\mathbf{V}^{-1}=\mathbf{V}^*$
- \mathbf{D} - a diagonal matrix with values being singular values of \mathbf{T}

Therefore, Equation 3.17 can be rewritten as:

$$\mathbf{I} = \mathbf{U}\mathbf{D}\mathbf{V}^*\mathbf{g} \quad (3.20)$$

and the solution for \mathbf{g} is found by multiplying the above equation by \mathbf{V} , \mathbf{D}^{-1} and \mathbf{U}^{-1} :

$$\mathbf{g} = \mathbf{V}\mathbf{D}^{-1}\mathbf{U}^{-1}\mathbf{I} \quad (3.21)$$

A real measurement was not possible during the experimental phase OP1.2b of W7-X since only 1 endoscope was installed at W7-X and its first mirror was fixed. Anyway, it was possible to make a mockup of an emissivity profile in the poloidal plane and produce an artificial image of the cameras. Then those artificial images were used to feed in the SVD algorithm for the reconstruction.

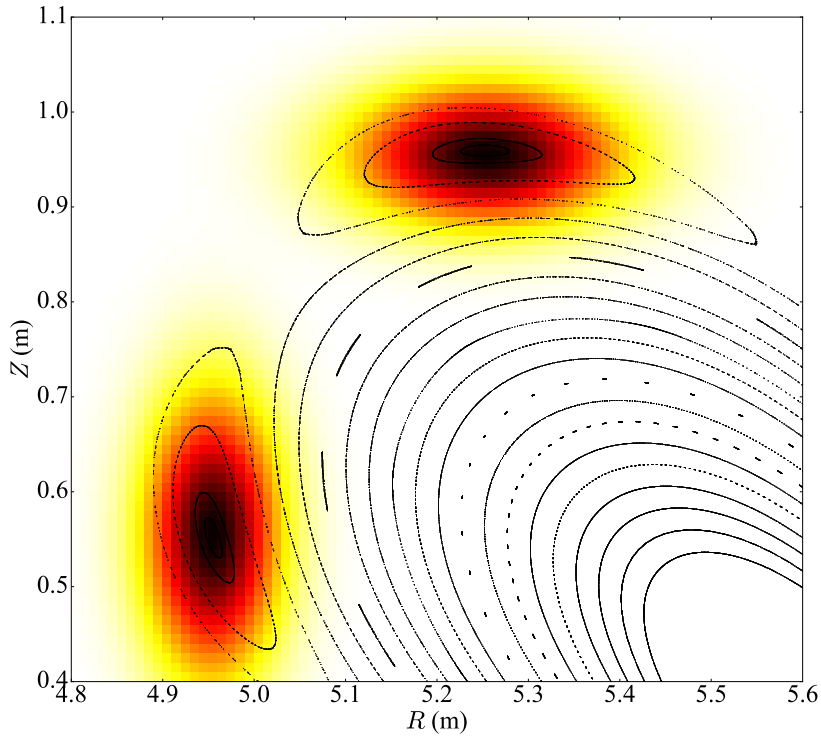


Figure 3.10: Test emission profile as a sum of 2 Gaussian distributions with the centers at the O-points of the magnetic islands in the standard magnetic configuration in the M51 module of W7-X (further adoption of [77]).

The specific emissivity profile used is shown in Figure 3.10, where 2 Gaussians are centered at the O-points of the magnetic islands intersected by the divertor targets in the M51 module of W7-X. The applied approach is further development of [77].

The emissivity profiles were then projected onto the flux tubes in 3D and corresponding camera images were built using Equation 3.16. After this an inversion was performed with the SVD method. The results are shown in Figure 3.11, where the upper row (a and b) are results when 2 endoscopes with 5 positions of the first mirror in the M51 module were used for the above described procedure. The lower row shows results for 4 endoscopes in the M30 and M51 modules with 5 positions of the first mirror for each endoscope.

It is obvious that if more camera views are used - more information is available for the reconstruction. In addition, rotation of the first mirror can provide even higher ratio of known to unknown variables in Equation 3.17.

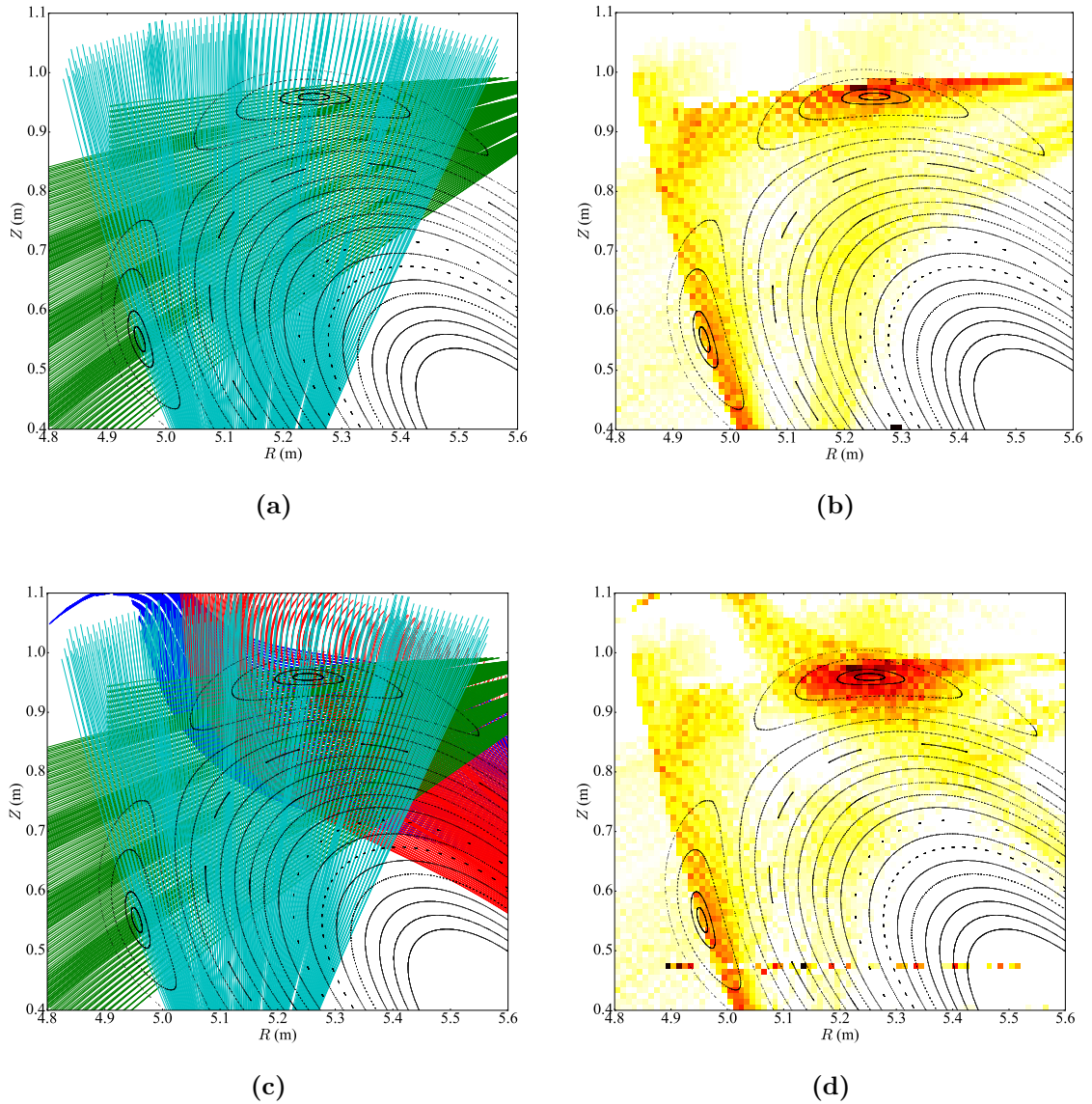


Figure 3.11: a) Fields of view of 2 endoscopes in the M51 module of W7-X for 5 different positions of the first mirror (J - green, L - cyan); b) Result of reconstruction with 2 endoscopes in the module M51; c) Fields of view of 4 endoscopes in the M30 module of W7-X (J - blue, L - red) and in the module M51 for 5 different positions of the first mirror; d) Result of reconstruction with 4 endoscopes in the modules M30 and M51 (further adoption of [77]).

The analogous procedure has been performed to test tomographical reconstruction of radiation of impurities injected through the divertor nozzles. For example, helium 2D emission profiles can be used to reconstruct 2D T_e and n_e profiles.

In this case a HeI emission profile was simulated by a Gaussian form, as suggested in [78]. The results of the initial profiles and the reconstructed result are shown in Figure 3.12. As in the previous case, more cameras would provide better reconstruction. Although, that would require puffing of helium in both M30 and M51 module and assumption of up-down symmetry between both modules. Once 2D profiles of all 3 HeI lines for He-BES available the n_e and T_e profiles are deduced as described in subchapter 3.2.

3. Spectroscopy at the divertor region of Wendelstein 7-X

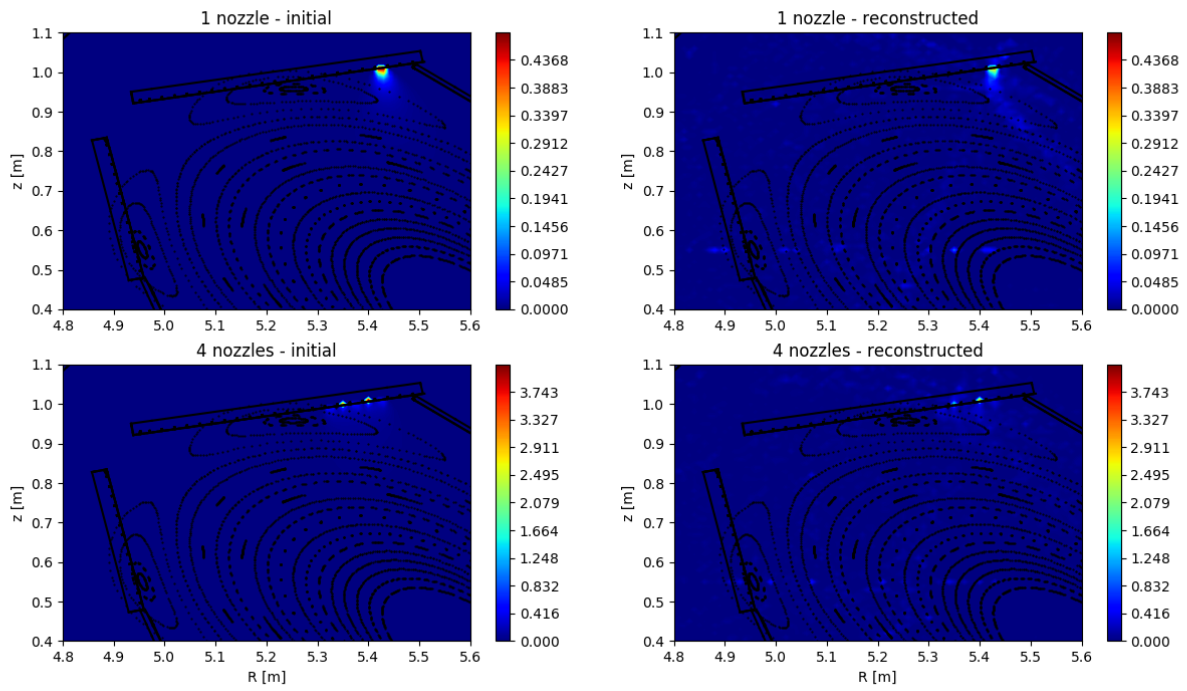


Figure 3.12: Simulated emissivity of He being injected with 1 (top left) and 4 (bottom left) nozzles at the divertor target in the module M51 of W7-X. The results of reconstruction are shown to the right of the corresponding initial profiles.

4

Wall conditioning at Wendelstein 7-X equipped with the passively cooled divertor

It is a well known fact that the wall conditioning of plasma devices is essential for achieving a cleaner plasma with lower impurity content. In its order it leads to a wider plasma operation window in the sense of higher plasma density and deposited energy due to reduced radiation-induced disruption. A number of techniques were used at W7-X during the last operation phase OP1.2 to tackle this issue. The used approach can be divided in two phases: before and after plasma operation of the machine. Before plasma operation baking at 150 °C for approximately 11 days was used to reduce all the impurities in the plasma vessel. After this glow discharge cleaning (GDC) in hydrogen was used to further decrease water, carbohydrates and methane levels. A short GDC in helium was applied afterwards to desaturate the wall of the machine from hydrogen.

After the start of the plasma operation both GDC in helium and hydrogen were used intensively in the experimental campaign OP1.2a for the purposes described above. The statistics of the duration of the GDC discharges in the operation phase OP1.2 are given in Table 4.1, taken from [79]. It is important to note, that after the application of the boronization in OP1.2b the use of hydrogen GDC was completely stopped. From one point it was important to avoid hydrogen GDC due to its sputtering of the boron layer. From the other point, a GDC in hydrogen has become redundant due to significant drop in the main low-Z plasma impurities oxygen and carbon, which is the main focus of this chapter. The duration of GDC in helium was negligibly small. Since strong wall fueling was still an issue after boronization, electron cyclotron wall conditioning (ECWC) in helium was still applied to desaturate the wall from hydrogen. In the future operation phase ion cyclotron wall conditioning (ICWC) will be also applied [80, 17].

4. Wall conditioning at Wendelstein 7-X equipped with the passively cooled divertor

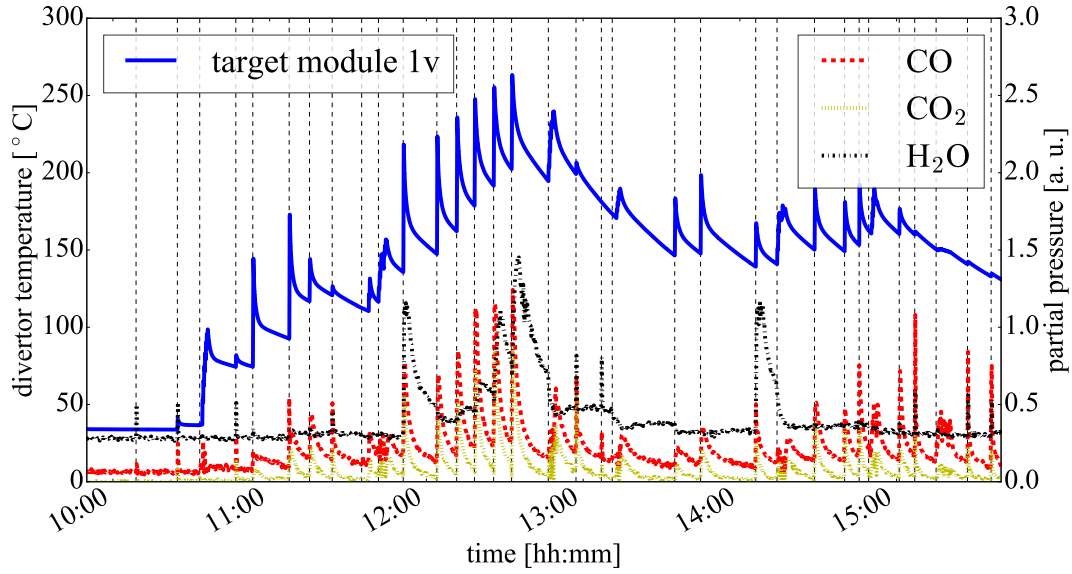


Figure 4.1: Temperature of the divertor module 1v of the upper divertor target M51 of W7-X (left axis) and partial pressure of CO, CO₂ and H₂O (right axis) on the last day before boronization 20180801 (Sereda et al. [2]).

Experimental campaign	OP1.2a	OP1.2b
	Before plasma operation	
H ₂ -GDC	2:58 h	9:35 h
He-GDC	0:36 h	1:50 h
	During plasma operation	
H ₂ -GDC	13:46 h	1:03 h*
He-GDC	14:48 h	2:24 h*

Table 4.1: Statistics of the GDC usage in the experimental phases OP1.2a and OP1.2b. * - the GDC duration before boronization application, after its application the values are negligible [79].

The temperature of the plasma-facing components was increasing during a day of operation leading to significant increase in impurity release. An example is shown for the last experimental day before boronization (20180801) in Figure 4.1. It is clear that H₂O, CO and CO₂ levels would increase for approximately one order of magnitude after heating the divertor. The situation was analogous as in the first TDU experimental campaign OP1.2a [81]. The location of the thermocouples is shown in Figure 4.2.

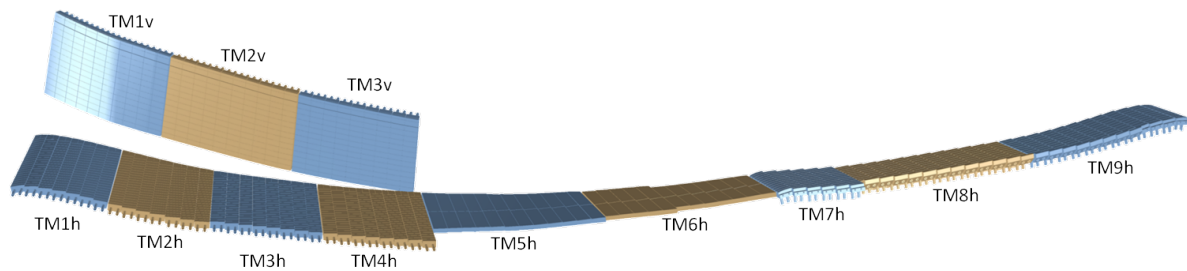


Figure 4.2: Description of the target modules naming convention. The thermocouples used in this work were located in the module TM1v. Figure produced by Marco Krause.

4.1 Baking

The first step of wall conditioning procedure of Wendelstein 7-X was baking, which was performed after plasma vessel closure and initial pump down. The plasma vessel was kept at 150 °C for one week [82]. Mainly water and hydrocarbons were removed due to the thermal desorption. Another process was thermal de-trapping of particles. In this case particles diffused through the bulk material and recombined at the surface [81] and then were pumped out.

The quadrupole mass spectra is shown in Figure 4.3 for outgassing of the plasma vessel at 28 °C before and after baking. The main influence of baking is release of water and its pressure drop by one order of magnitude. CH₄, CO and CO₂ decreased too, but their decrease was not so profound as for water due to chemical erosion of C by O, as discussed before. The heavy hydrocarbons decreased too, as seen for the mass to charge ratios greater than 50.

Baking was not sufficient to provide the required low pressure in the plasma vessel of W7-X after initial conditioning. As explained in Chapter 1, the relative change of the plasma pressure is:

$$\frac{\Delta P}{P} = \propto t^{-1} \quad (4.1)$$

In the case of W7-X the effectiveness of baking quickly dropped after one week period and it is the optimal time for this approach at W7-X. Moreover, heating of the all plasma vessel required special protective measures for the diagnostics around the machine. These measures basically put most of the device manipulations on hold for a week.

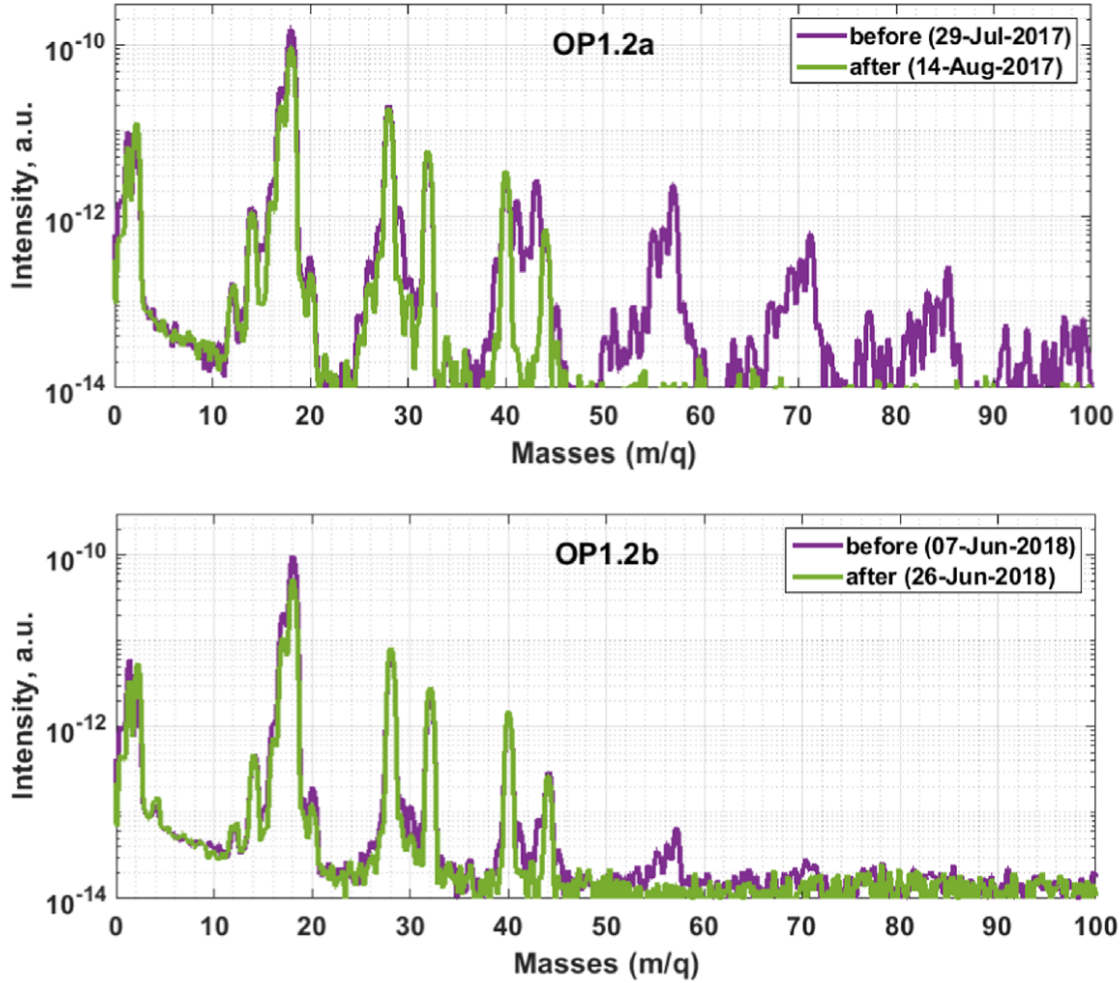


Figure 4.3: Quadrupole mass spectra of the Wendelstein 7-X plasma vessel outgassing before and after baking in both test divertor units campaigns of Wendelstein 7-X OP1.2a (2017) and OP1.2b (2018). The mass to charge ratio constitutes the x-axis and the spectra signal is given in arbitrary units (taken from [79]).

From Figure 4.3 it is obvious that in the second TDU campaign the relative decrease in the impurities was smaller than in the first one. This difference is due to the fact that most of the plasma-facing components were not changed between the two mentioned campaigns providing partly cleaned components for the second campaign.

4.2 Glow discharge cleaning

After initial baking the next step is the glow discharge cleaning (GDC) in H_2 or He. In this case magnetic field is not required. The cleaning technique is based on a hollow cathode discharge. For this a set of anodes is located around the plasma vessel and is biased to $\approx [200 - 400]$ V. The grounded plasma vessel serves as a cathode.

The electrons from anodes are accelerated in the sheath and ionize the neutral gas molecules and atoms. Those ionized molecules and atoms are accelerated to the surface where due to the chemical or physical sputtering they deabsorb the surface from the impurities and plasma fuel. The effectiveness of this process depends both on the homogeneity of the discharge and the ion current. Those two parameters can be tuned by

an appropriate number of anodes around the torus (10 for W7-X), voltage and neutral gas pressure. More details can be found in [24].

H₂-GDC is used to deplete the surface from mainly water and hydrocarbons. In contrast, He-GDC is frequently used to deplete the surface from the retained hydrogen either from a H₂-GDC or a normal plasma discharge in hydrogen to decrease fuel release from the walls and make density control possible. In the case of a He-GDC the process is well described in [23], where the neutral pressure of He and H₂ is describes by a set of neutral pressure balance equations for the Wendelstein 7-X case:

$$\dot{p}_{\text{H}_2} \approx -p_{\text{H}_2} \frac{S_{\text{H}_2}}{V} + c(t)Y_{\text{He}^+}p_{\text{He}}k_{\text{He}}^i n_e - (1 - R_{\text{H}_2^+})p_{\text{H}_2}k_{\text{H}_2}^i n_e, \quad (4.2)$$

where $k_{\text{He},\text{H}_2}^i$ are ionization rates, Q_{He} gas flow of He from external source, S_{He,H_2} vacuume pumping rate, $R_{\text{He}^+,\text{H}_2^+}$ recycling coefficient and Y_{He^+} - removing yield of H₂ by a helium ion.

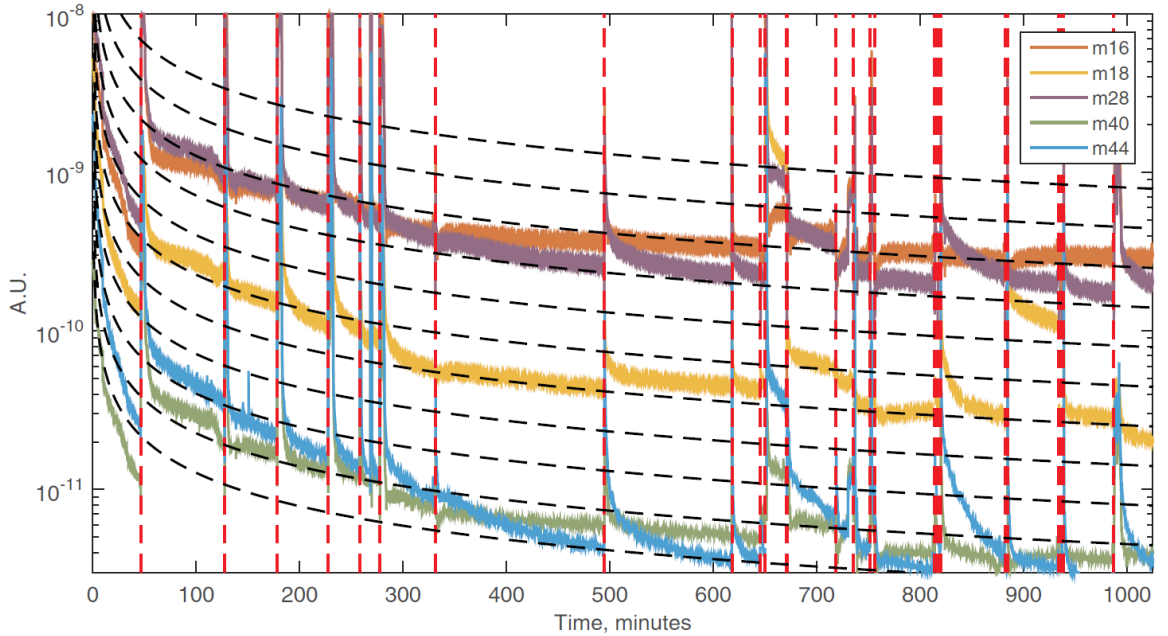


Figure 4.4: QMS spectrometry of the cumulative H₂-GDC during OP1.2a of W7-X. The red dashed lines correspond to the days with ECRH operation. The black dashed lines show the time envelopes. m16 - CH₄, m18 - H₂O, m28 - CO, m40 - Ar and m44 - CO₂ (taken from [81]).

These equations show that the wall is struck by He⁺ ions. In addition, H₂⁺ ions come from the released H₂ molecules which were ionized. As seen from Equation 4.2, maximizing the vacuum pumping speed and minimizing the recycling coefficient can improve the hydrogen removal from the vessel.

It should be noted, that since both H₂-GDC and He-GDC reach most of the plasma facing components it is important to avoid these techniques after deposition of low-Z films, since as they were deposited in a GDC they can also be removed with it due to sputtering processes. In addition, erosion of metal is also possible and GDC discharges should be minimized to avoid it. In the previous work of Gorjaev et al. [83] the best parameter were found for H₂-GDC: working pressure 4.5×10^{-3} mbar, anode current of 1.5 A with voltage of 305 V. For the He-GDC the parameters were: working pressure 3.8×10^{-3} mbar, anode current of 1 A with voltage of 210 V.

4. Wall conditioning at Wendelstein 7-X equipped with the passively cooled divertor

Figure 4.4 shows a cumulative result of the H₂-GDC application in OP1.2a of W7-X for CH₄, H₂O, CO, Ar and CO₂. The red dashed lines correspond to the days with plasma operation and the black dashed lines show the time envelopes.

4.3 Electron cyclotron wall conditioning

This subchapter begins with a quick reminder about the ECRH conditioning presented in subchapter 1.6. In contrast to baking and GDC the radio frequency (RF) assisted wall conditioning can be performed in the presence of the magnetic field. This is very important for W7-X, for which the magnetic field was switched on in the morning of an operational day and then only switched off in the evening after the performed experimental plasma discharges. This hold for both the limiter and the TDU campaigns. The RF assisted wall conditioning in the electron resonance is referred as electron cyclotron wall conditioning (ECWC) and in the ion range as ion cyclotron wall conditioning (ICWC).

In the case of stellarators the RF cleaning can be done in a divertor configuration of the magnetic field, since the nested magnetic surfaces exist even without toroidal plasma current. This means that in the case of a stellarator the plasma is fully ionized and the location of the plasma wetted area is the same as in a normal plasma discharge with the same magnetic configuration [80]. Both electron and ion RF are possible, but in the limiter (OP1.1) and the TDU campaign of W7-X only the electron RF were available at the second harmonic X2 at 140 GHz frequency (for $B = 2.5$ T).

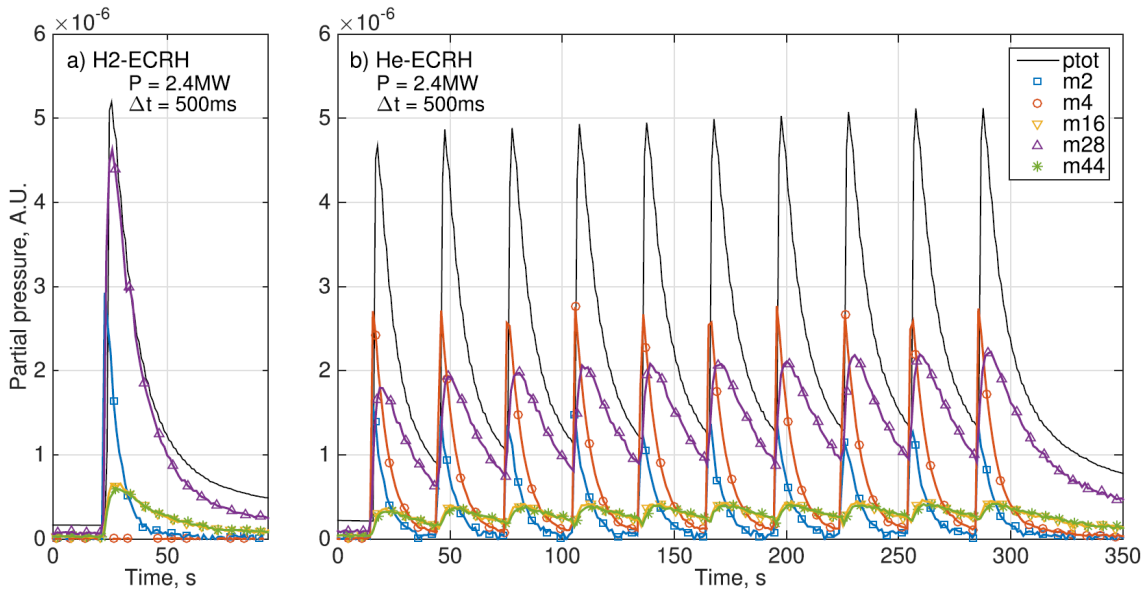


Figure 4.5: QMS spectrometry of the ECWC discharge in hydrogen (20160209.004, left) and the ECWC in helium (20160209.005, right) with a 'train' of plasma pulses during OP1.1 of W7-X. The red dashed lines correspond to the days with ECWC operation. The black dashed lines show the time envelopes. m2 - H₂, m4 - He, m16 - CH₄, m28 - CO and m44 - CO₂ (taken from [84]).

It was found in [79] that the most effective scheme to desaturate the wall from the retained hydrogen is a pulsed operation on an ECWC in helium. In this scheme a set of ≈ 3.5 s pulses with a period ≈ 20 s. A similar situation is shown in Figure 4.5, where a hydrogen and helium ECWC are shown. In this figure the partial pressures of H₂, He, CH₄, CO and CO₂ are shown for two discharges. In addition, it is possible to use a

pulsed operation in hydrogen to get rid of impurities, like a train of ultrashort pulses of ≈ 3 ms without full ionization [85]. Such an approach was tested in OP1.2a and aimed at more uniform H flux to the surface, but more detail study of its effectiveness should be done.

Since the wetted area of an ECWC discharge is as in a normal plasma discharge, an important improvement was usage of the control coils of W7-X. These coils allowed sweeping of the strike line and, therefore, an increase of the wetted area. The increase of hydrogen removal was 30% [79]. This technique is important since the strike line during a normal discharge is moving due to the increase of the toroidal plasma current and hydrogen is deposited across the divertor target.

4.4 Boronization set-up

The boronization procedure requires an approach with high safety standards due to the high toxicity and explosiveness of the diborane gas. For this purpose the boronizations were conducted on Saturdays where only a limited number of personnel was allowed to enter the building. In addition, a full chemical safety suits were required due to the safety regulations. During the first boronization 11 people were present in the control room of Wendelstein 7-X with this number lowered to 8 during the third boronization due to the optimized approach.

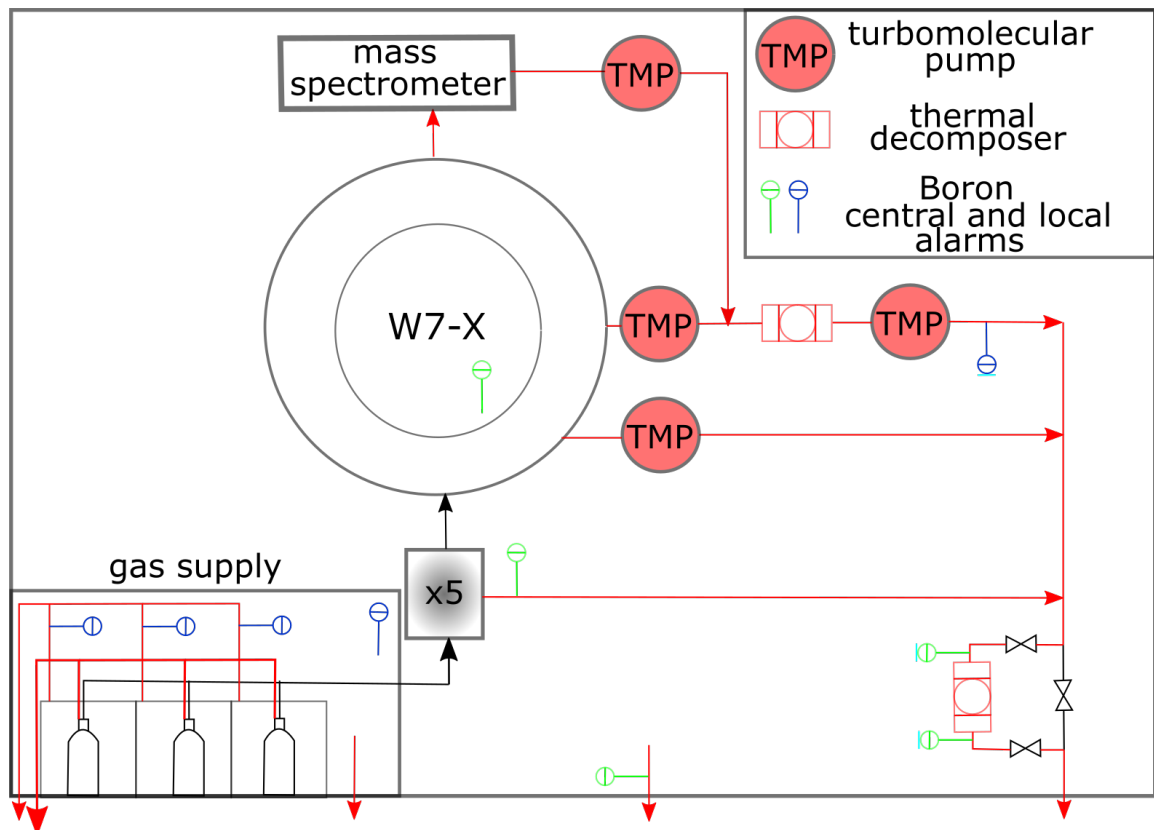


Figure 4.6: Scheme of the boronization set-up during OP1.2b of W7-X.

The three diborane (B_2H_6) gas bottles were located in a dedicated gas supply cabinet. The cabinet was equipped with a diborane sensors which in case of the pre-defined diborane concentration would cause a diborane release through the gas evacuation

4. Wall conditioning at Wendelstein 7-X equipped with the passively cooled divertor

system. In addition, the same would be done if the pressure in the bottles would exceed the pre-defined value and the gas would be released through the bursting disk release pipe.

The diborane gas was feed in the vacuum vessel through 5 gas-inlet modules symmetrically located around the plasma vessel of W7-X giving better conditions for homogeneous distribution of the boron layer on all plasma-facing components of the device. The boronization was performed in a He glow discharge (He-GDC) with 10 anodes located symmetrically around the plasma vessel. The diborane concentration was 10% (limited by the governmental regulations) and the concentration of He was 90%. It total 3 boronizations were performed. The details about the date, duration and the used amount of the diborane gas are given in Table 4.2.

date	duration [hours:minutes]	diborane used [Nl]
04 August 2018	3:30	45
01 September 2018	5:30	85
29 September 2018	5:00	68

Table 4.2: List proving the date, the duration and the used amount of the diborane gas for each boronization during OP1.2b of W7-X. Nl stands for normal liter.

4.5 Strategy to assess boronization at Wendelstein 7-X

Its important to once again introduce the plasma facing components of Wendelstein 7-X:

1. 10 discrete test divertor units made of fine-grane graphite (FGG) - 25 m²
2. Baffle (FGG) - 33 m²
3. Poloidal closure made of stainless steel (SS) - 10 m²
4. Toroidal cloure (FGG) - 3 m²
5. Panels protecting pumping gap (SS) - 10 m²
6. First wall protection system: 50 m² of FGG and 70 m² of SS

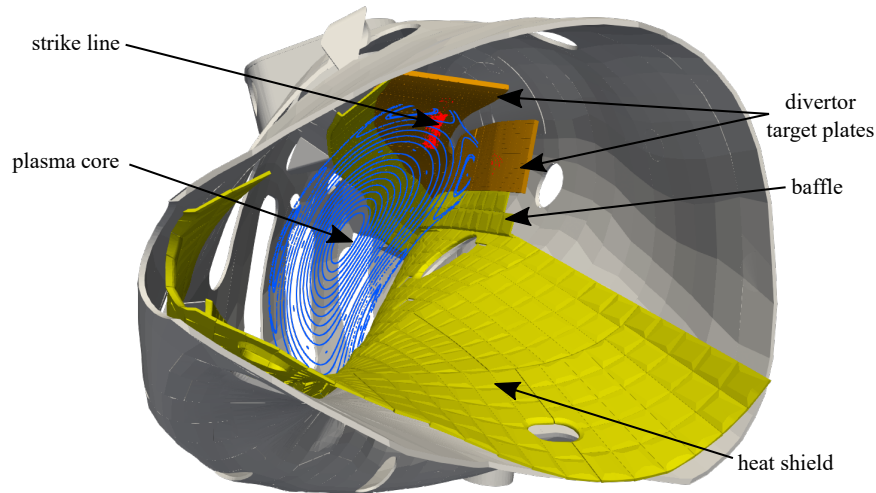


Figure 4.7: Plasma-facing components of W7-X (Sereda et al. [2]).

At the beginning of the campaign three boronizations were planned. The first boronization was the most important one to study impurity levels and composition of the plasma. In addition, it was important to study the radiation-induced density limit. For this purpose two dedicated days were devoted to the boronization study. In order to assess the boronization a matrix of plasmas (parameter scan) was planned.

To study the impurity levels a set of plasma programs with constant density and increasing power in a form of steps was used, as shown in Figure 4.8. Three power levels of 2 MW, 4 MW and 6 MW were planned. In addition, plunges of the multi-purposed manipulator with appropriate probe heads were needed to obtain n_e and T_e density profiles of the plasma. One plunge per power level is sufficient.

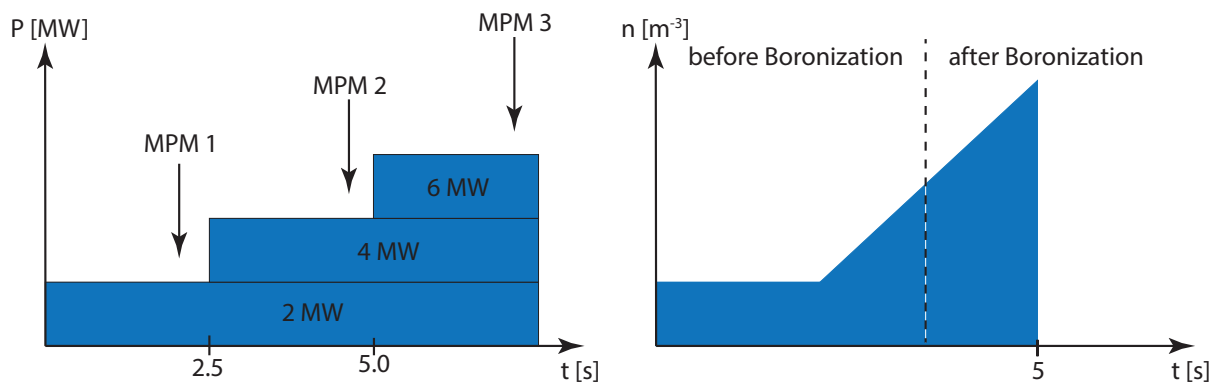


Figure 4.8: Strategy for the first boronization assessment: (a) - impurity levels and composition, (b) - radiation induced density limit.

To study the radiation induced density limit another scheme was proposed, in which the power level should be constant and the density level should be risen until the plasma disruption. Such a density ramp would be possible either with a gas ramp or multiple puffs, as shown in Figure 4.8. An MPM plunge would also be needed for plasma profiles. A set of power levels would let comparison of different plasma conditions. Repetition of equal discharges would also let full diagnostic scan, specifically for spectrometers and filter cameras. The spectrometer settings should mainly allow observation of CI, CII, CIII, OI, OII, H_α , H_β , H_γ , H_δ , BI, BII lines. In addition molecular bands of CH, H_2 and BH are also needed. as discussed in Chapter 3.

4. Wall conditioning at Wendelstein 7-X equipped with the passively cooled divertor

Another evidence of O \rightarrow C mechanism is the observation that the CO outgassing is related to the hottest PFC regions [81].

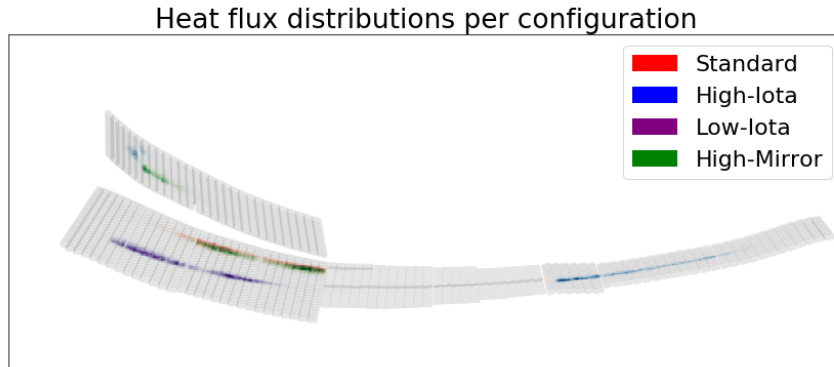


Figure 4.9: Heat flux distributions for the main magnetic configurations on the divertor targets of W7-X, as calculated for the “vacuum” case (Sereda et al. [2]).

Configuration family	Number of discharges	Plasma exposure time [s]	Fraction of time [%]
Standard (group EIM/EJM) [f/r]	638	4809	53.1
High-mirror (group KJM/KKM)	234	1392	15.3
Low-iota (group DAM/DBM) [f/r]	169	1180	13.0
High-iota (group FTM) [f/r]	315	1673	18.5
Total	1256	9054	-

Table 4.3: Statistics of the plasma exposure time for the OP1.2b experimental campaign of W7-X, ‘f’ corresponds to forward and ‘r’ to reversed magnetic configurations (Sereda et al. [2]).

Table 4.4 lists all reference discharges of the power step type used for the long-time effects of boronization characterization.

4.5 Strategy to assess boronization at Wendelstein 7-X

Discharge id	$n_{e1} [\cdot 10^{19} \text{m}^{-2}]$	$P_{ECRH} [\text{MW}]$	$t_b [\text{s}]$	$t_e [\text{s}]$	configuration
20180801.021	2	2, 3, 4	0.5*	2.0*	standard
20180807.011	2	2, 3, 4	2.8	4.5	standard
20180814.030	6	3	2.0	6.0	standard
20180816.015	6	1, 2, 3	4.5	5.5	standard
20180821.005	3.5	2, 2.5	2.9	3.3	standard
20180905.004	3.5	2, 3, 4	2.2	3.8	standard
20180906.006	5.5	2, 3, 4	2.8	3.8	standard
20180918.006	3	2, 3, 4	2.8	3.8	standard
20180919.005	3.5	2, 3	2.2	3.3	standard
20180920.004	3.5	2, 3, 4	2.2	3.8	standard
20181010.005	5.5	2, 3, 4	2.4	3.8	standard
20181016.004	6	2, 3, 3.5	3.0	3.8	standard
20181018.003	3.5	2, 2.5, 3.5	4.5	8.5	standard

Table 4.4: List of the discharges used for long-time characterization of the influence of the boronizations on the performance of W7-X. * - for the TDU data a similar discharge 20171207.013 was used.

5

Effects of boronization

5.1 Electron temperature and density profiles

The edge profile of T_e and n_e were measured with the combined probe mounted on the multi-purpose manipulator. Unfortunately, the pre-boronization data from OP1.2b was not available and an equivalent discharge 20171026.027 from OP1.2a in the standard magnetic configuration was used as a reference. At the moment of plunge P_{ECRH} was 1.8 MW. For the post-boronization characterization the data was available for the 20180807.017 discharge with $P_{\text{ECRH}} = 2.5$ MW. The measurements for the OP 1.2a discharge were done with the triple Langmuir probe and for the OP 1.2b discharge with the swept single Langmuir probe. The latter one was used since the former one had been damaged at the end of the OP1.2a campaign.

The discharges were run at a similar heating power, this is reflected in the measured edge temperatures. Considering the possible errors from the different modes of measurement they are quite similar. In contrast to the edge temperature, the edge density significantly increased after boronization - by a factor of 7. This correlates with the increase in the core density - by a factor of 2.5. Even stronger change in density at the edge can be explained in terms of higher oxygen concentration in this region (in comparison with the core), as suggested by the oxygen radiation at the edge.

Furthermore the higher density did not cause higher radiative losses, due to the reduced impurity influx into the edge plasma. This is another good example of the effectiveness of the boronization, which allowed plasma operation at higher densities in W7-X without causing a radiative collapse. The corresponding profiles are shown in Figure 5.1.

5. Effects of boronization

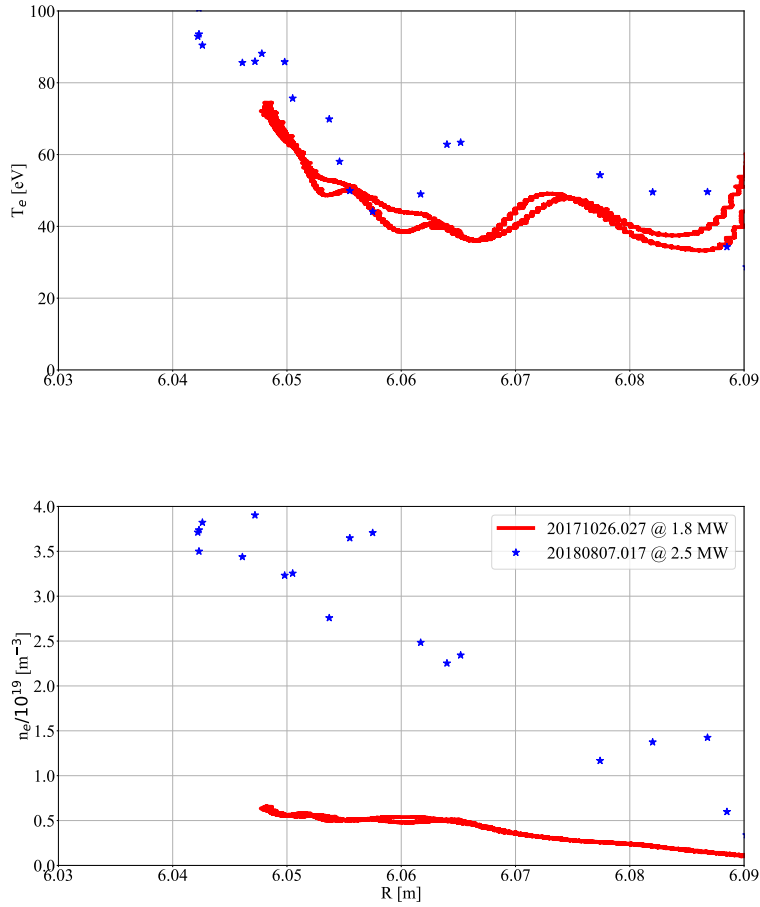


Figure 5.1: T_e and n_e edge profiles measured with the combined probe mounted on the multi-purpose manipulator. The data was available for the standard magnetic configuration in OP1.2a (20171026.027, $P_{\text{ECRH}} = 1.8$ MW) as a reference for the pre-boronization conditions and OP1.2b (20180807.017, $P_{\text{ECRH}} = 2.5$ MW) for the post-boronization characterization.

Another important question is the change of T_e and n_e profiles shape after boronization. The main tool of n_e density measurement was the dispersion interferometer providing line-integrated results: $\int n_e dl$ [m^{-2}] along its line of sight. Its data was immediately available after each discharge with high temporal resolution. In contrast the Thomson scattering results needed more time consuming processing after discharges by the responsible officers.

n_e profiles for 2 discharges before (20171026.027) and after (20180801.021) boronization are shown in Figure 5.2 (left). As for the edge measurements density in the main plasma also increased, but by \approx a factor of 3. Before boronization the density profile is rather flat. After boronization the form of the profile changed and showed peaking at the plasma core and a steeper decrease approaching the edge.

Nevertheless, an averaged value of the line-integrated density obtained by division by the length of sight of the dispersion interferometer (1.33 m) represents the core value very well with the reliable range of 10%. This is illustrated by Figure 5.2 (right), where n_e^{core} [m^{-3}] obtained with the Thomson scattering is shown as function of the line-averaged density $\frac{\int n_e dl}{l}$ [m^{-2}].

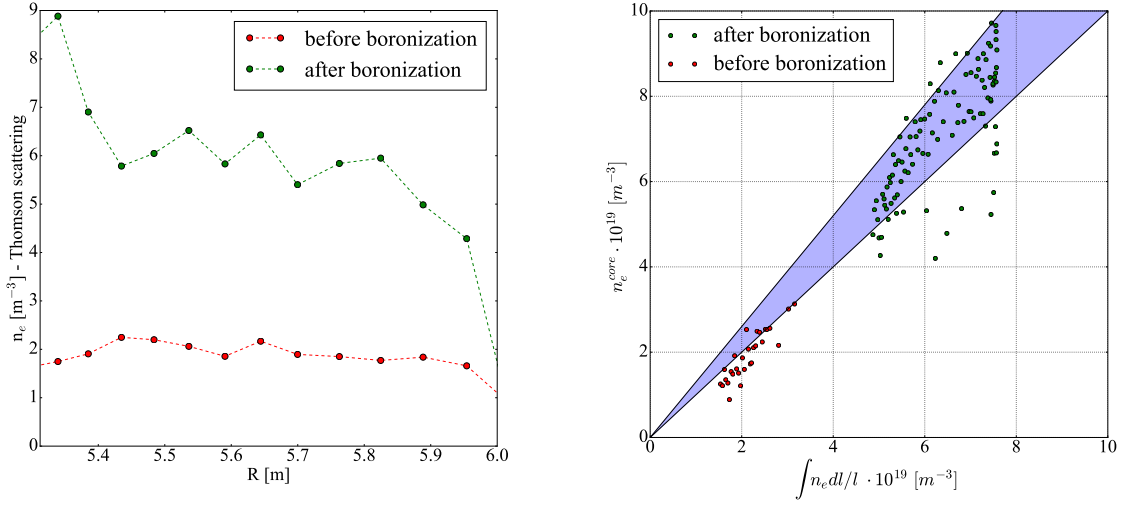


Figure 5.2: n_e profiles obtained with the Thomson scattering diagnostic for the reference discharges (left). Core values of n_e as function of the line integrated n_e divided by the integration length for the reference discharges before and after the first boronization (right).

5.2 Radiation of the low-Z impurities: carbon and oxygen

After the first boronization a substantial reduction of the line radiation of O and C was observed. In Figure 5.3 emission spectra are shown for the reference discharges before the first boronization (20180801.021) and after the first boronization (20180807.011) with similar conditions. For both discharges a moment at the flat top with heating power $\text{PECRH} = 3 \text{ MW}$ and line integrated density approximately $2 \cdot 10^{19} \text{ m}^{-2}$ has been selected. From Figure 5.3 it is clear that the most intensive OI (atomic oxygen) lines at 777.2 nm and 844.7 nm have substantially decreased. The intensity of the CII (C^{1+}) line at 426.7 nm has also significantly decreased. The newly arisen BII line at 703.1 nm is emitted by B^+ . No detectable signs of the molecular CH Gerö band with the head at 430 nm were found on the last day before and the first day after the first boronization.

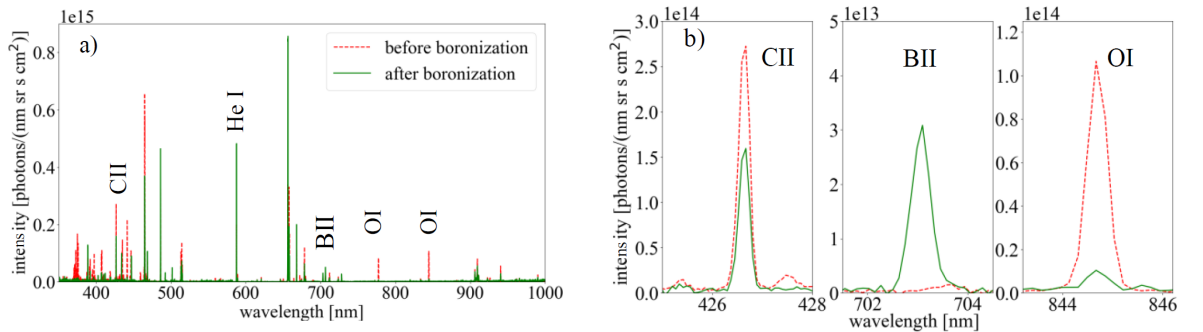


Figure 5.3: Emission spectra measured at the divertor before (red, discharge 20180801.021) and after (green, discharge 20180807.011) the first boronization of W7-X a) in the range of 350 nm – 1000 nm and b) in the vicinity of CII, BII and OI lines (Sereda et al. [2]).

5. Effects of boronization

The same qualitative behaviour is observed in the XUV spectra obtained by the core spectroscopy. The line radiation of O dropped significantly, the C emission decreased and a newly arisen B was seen, as expected, in the spectra (see Figure 5.4).

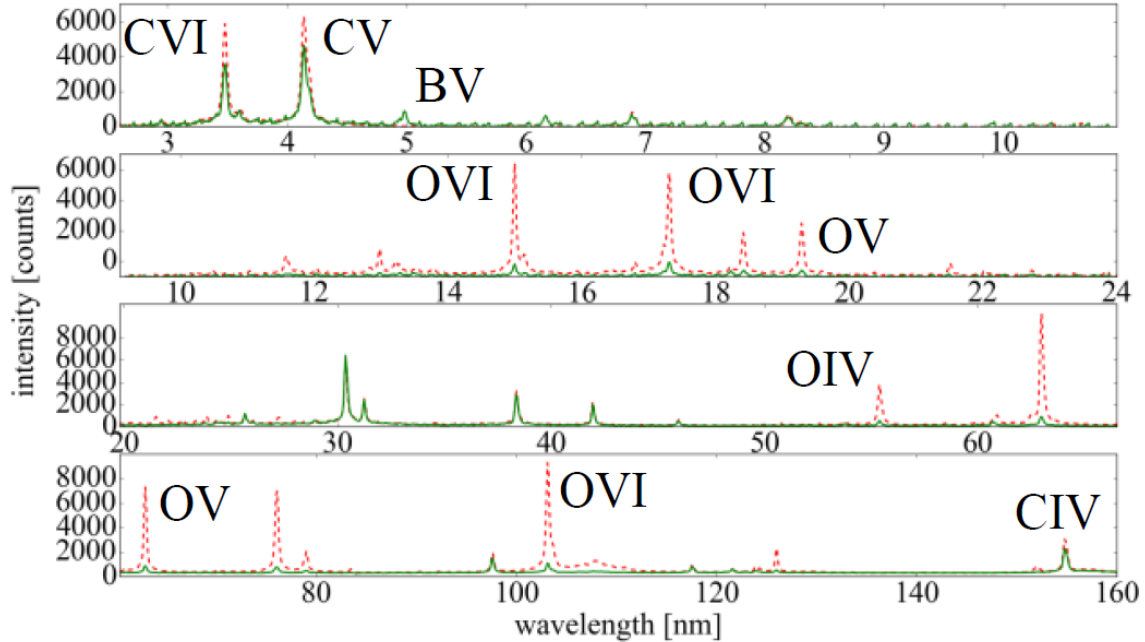


Figure 5.4: Emission spectra in the range 2.6 – 160 nm obtained with HEXOS before (red dashed) and after (green) the first boronization (Sereda et al. [2]).

Due to the substantially decreased line radiation of low- Z impurities O and C the operational window of W7-X was significantly widened in terms of maximum plasma density and stored energy.

Figure 5.5 shows two dedicated discharges of the ‘density ramp’ type before and after the first boronization. Impurity normalized influx of O and C is shown before and after boronization and newly arisen B is present after it. The first boronization resulted in much higher densities. Before it was possible to get line-integrated electron densities up to $4 \cdot 10^{19} \text{ m}^{-2}$ and after values of $1.1 \cdot 10^{20} \text{ m}^{-2}$ were achieved. Simultaneously, impurity normalized influx of O and C dropped approximately by a factor of 4 for C and by approximately a factor of 50 for O right after the first boronization. One should keep in mind that the density after boronization significantly increased and the values in this case cannot be compared directly. Such a reduction in impurities normalized influx resulted in increased line-integrated electron density. This increase also allowed diamagnetic energy of the plasma to increase from approx. 330 kJ up to approx. 510 kJ after boronization (see Figure 5.6). The fraction of radiated power f_{rad} has decreased too. It is known that the impurity concentration decrease leads to the increased critical density [86]. Radiation power is mainly following the line radiation of oxygen [87]. In addition, values of Z_{eff} obtained from Bremsstrahlung radiation decreased from values of around 4.5 for all densities down to low values of around 1.2.

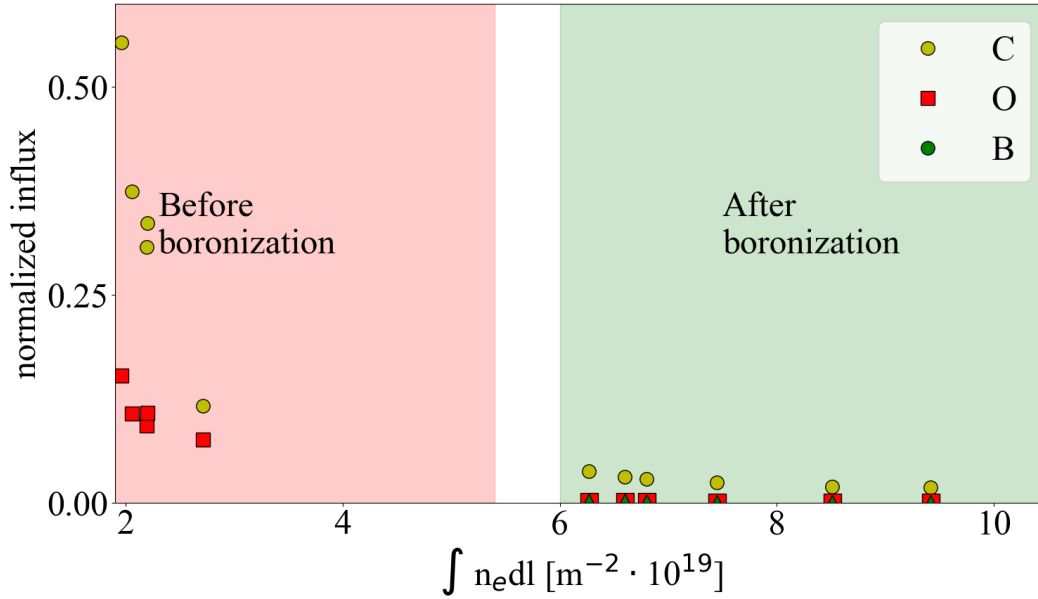


Figure 5.5: Normalized influx of low-Z O and C together with introduced B. Two discharges are shown on the plot: 20180801.036 before the first boronization (red background) and 20180807.013 after (green background) (Sereda et al. [2]).

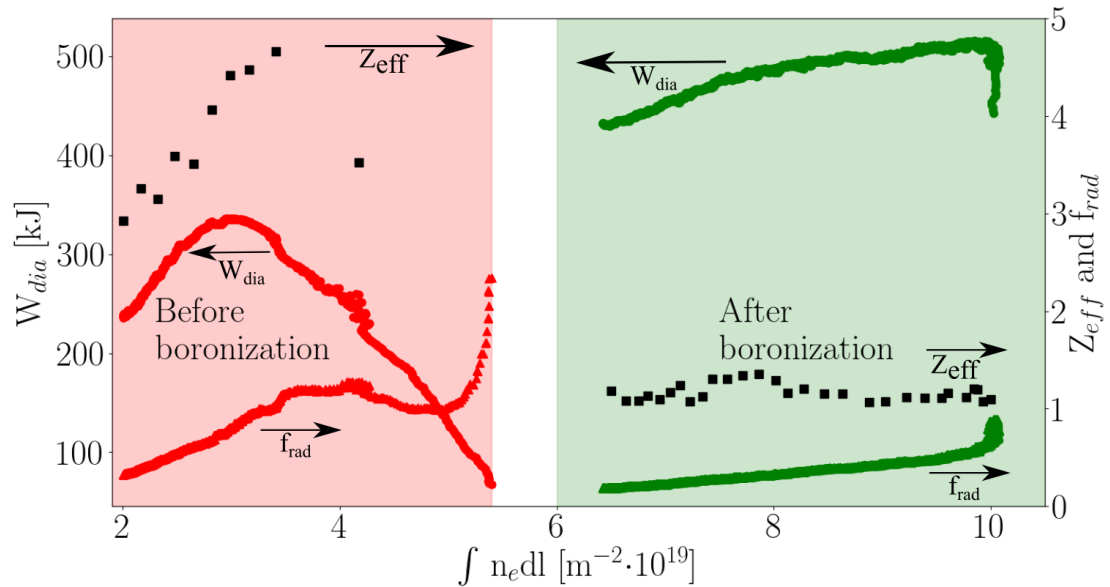


Figure 5.6: Diamagnetic energy, Z_{eff} and radiation fraction of the plasma f_{rad} as a function of the line integrated electron density before boronization (red, 20180807.013) and after (green, 20180801.036) boronization (Sereda et al. [2]).

5.3 Power loads on the divertor

Another important aspect is the influence of boronization on power loads on the divertor target. Since line radiation of oxygen and carbon has significantly decreased after boronization the power radiation at the edge by those impurities has significantly

5. Effects of boronization

decreased too. This decrease has led to higher divertor power loads (P_{div}) on the divertor targets. Figure 5.7 shows this result in more detail. The top and the middle images are the divertor power loads for the discharges before (20180801.021) and after (20180807.011) boronization at $t = 4$ s of the discharge. At this moment in both cases P_{ECRH} and $\int n_e dl$ were the same. It is clear that after boronization the power loads increased but quantitative analysis is complicated since a specific pattern depended on the toroidal current. To estimate this change a plot of P_{div} is shown at the bottom of Figure 5.7. Values of P_{div} were built along the axis shown in magenta in the above images. Indeed, P_{div} increased from the highest values of $\approx 4 \frac{\text{MW}}{\text{m}^2}$ to higher values of $\approx 5 \frac{\text{MW}}{\text{m}^2}$.

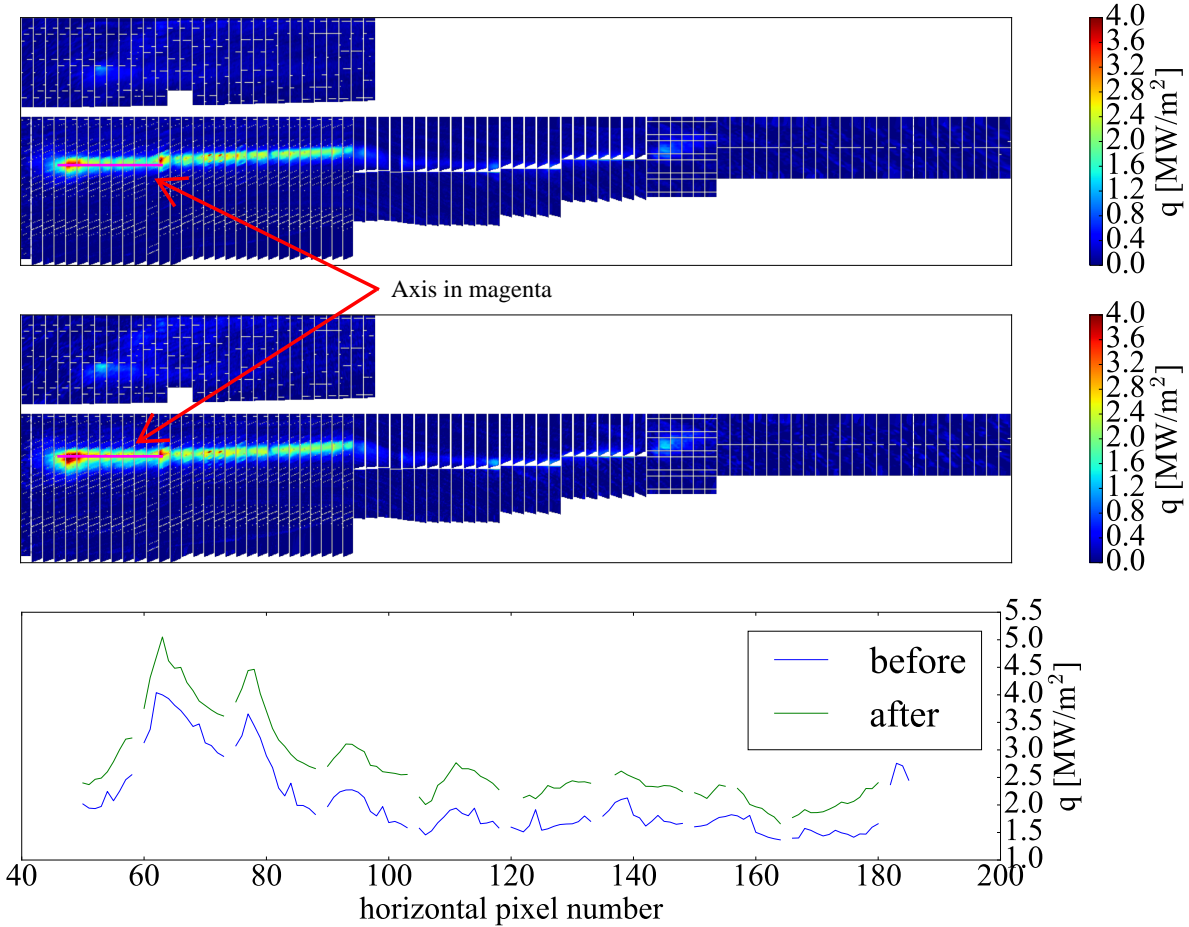


Figure 5.7: Power loads on the divertor P_{div} before (20180808.021, top image) and after (20180807.011, middle image) boronization. The plot of P_{div} on the bottom figure is along the axis shown in magenta in the upper two images.

One of the important positive effects of the high densities achievement was its influence on the heat distribution over the strike line. This influence is characterized by the so-called peaking factor - a ratio between the maximal measured heat flux of the strike line along the magnetic field lines to the average heat flux over the wetted area. Obtaining line-integrated densities close to 10^{19} m^{-3} allowed to decrease peaking factor by 50 percent [88].

In addition, application of boronization allowed a new detachment regime with much higher compression ratios of neutrals. After the boronization values up-to 30 were obtained, which is a factor of 4 higher than before boronization [88]. In the reference given above an heuristic explanation is suggested to explain this increase. It was suggested that the significant decrease in oxygen and carbon radiation at the divertor allowed

plasma to plug more in the divertor, as shown in Figure 5.8. On this figure yellow color represents the hot core plasma and the red color the cold edge one. Furthermore, after boronization the neutral source was located close to the divertor targets making them more easily pumped out. This location also could provide better condition for neutral screening, since the neutrals get ionized closer to the divertor targets and are transported back to the surface.

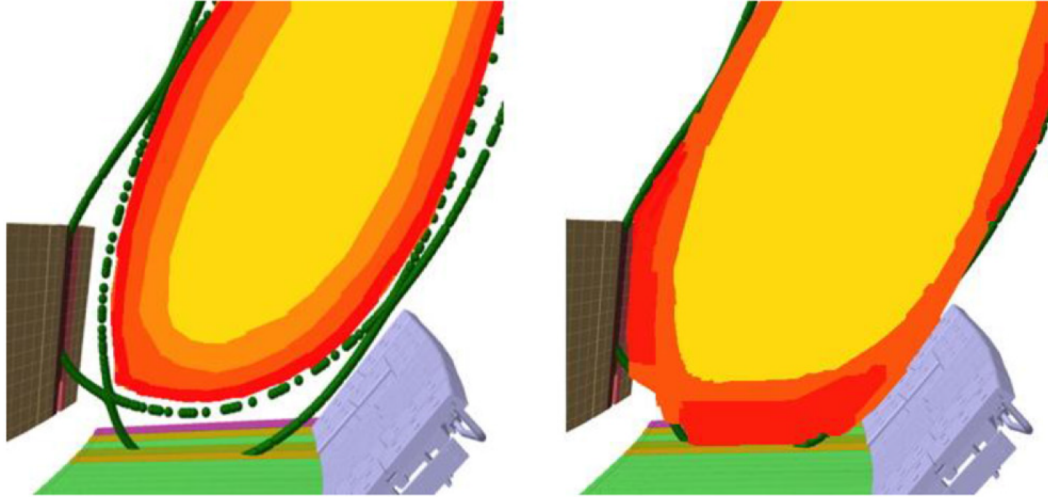


Figure 5.8: Heuristic explanation of the new detachment mechanism after boronization. For the details please follow the text (taken from [88]).

5.4 Morphology and chemical composition of the divertor surface

Interpretation of post-mortem analysis of the plasma-facing components is rather complicated due to the complex 3D nature of plasma-wall interaction in W7-X. Erosion zones at the divertor target plates give no information about deposited boron layers during boronizations. In contrast, the re-deposition zones can provide information about chemical composition of the a-B/C:H layers because of boronizations and the a-C:H layer due to natural deposition during plasma discharges.

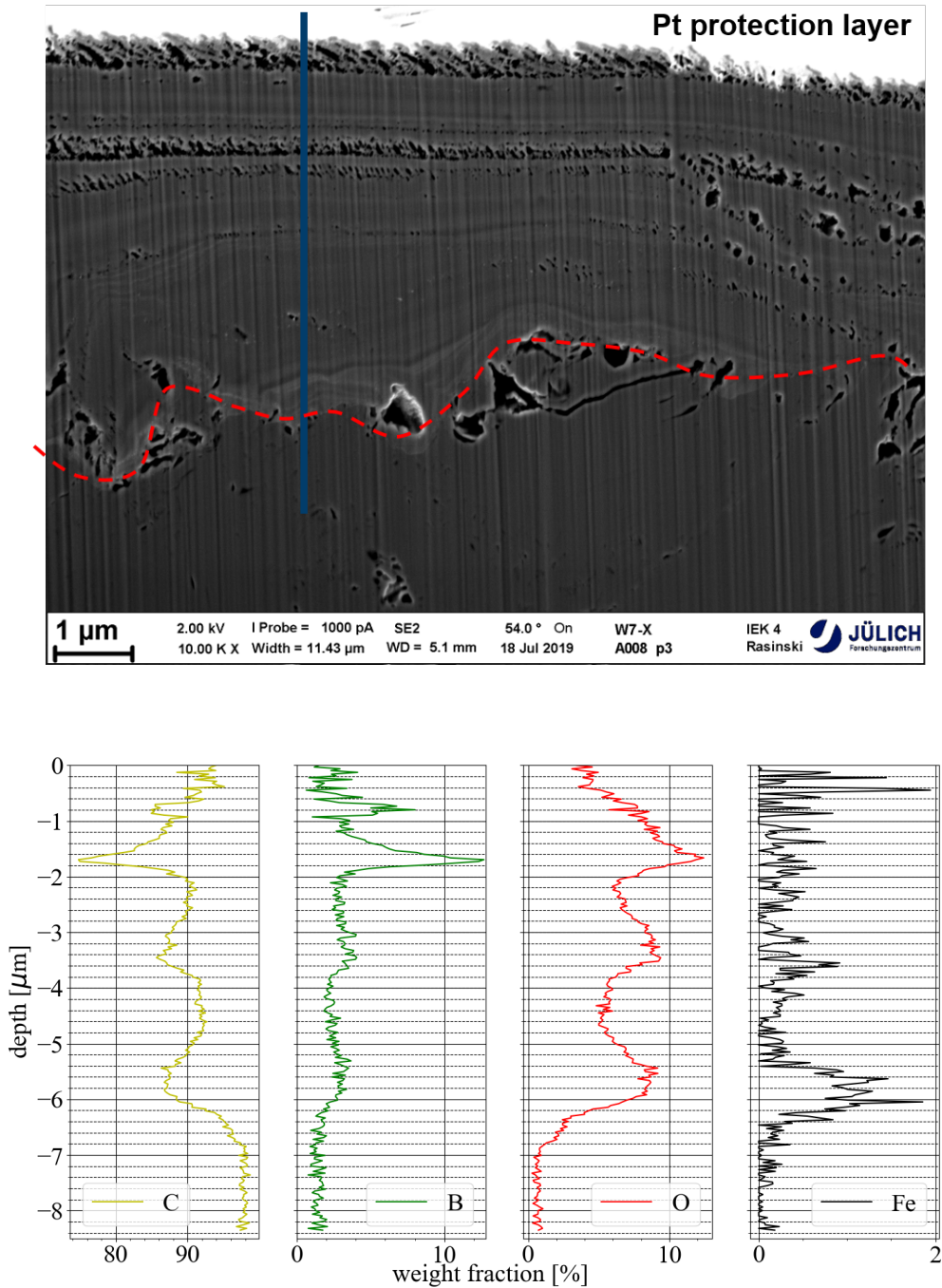


Figure 5.9: a) Scanning electron microscope (SEM) image of a re-deposition zone on the TM2h6 A008 element of the divertor (its location is shown in orange in Figure 2.15), blue line is the axis of the EDX scan. The red dashed line corresponds to the interface between preceding and the last experimental phases; b) Concentration profiles of carbon, oxygen, boron and iron (Sereda et al. [2]).

Figure 5.9a is a scanning electron microscope image of a focused ion beam (FIB) cross-section of such a region. The blue line is the axis along which plots in Figure 5.9b were plotted. Figure 5.9b shows concentration profiles of carbon, oxygen, boron and iron profiles of a re-deposition zone at the divertor target (the location of the sample is shown in Figure 2.15 in orange) obtained with energy-dispersive X-ray spectroscopy (EDX).

Concentration profile of oxygen and boron clearly show 3 distinctive peaks which can be related to the 3 boronizations of the campaign. Similar behaviour of both curves

gives another evidence that oxygen is gettered by boron oxide formation. Simultaneously, the carbon profile shows minimum for the same positions giving another argument that the oxygen and boron peaks are due to the boronizations and not due to re-deposition.

Iron shows a peak at $-6 \mu\text{m}$ in the FIB cross-section, which is related to the He glow-discharge cleaning performed frequently before boronization. During these discharges iron was eroded from the metal components by He ion impact on the steel and transported to these deposition zones. Another interesting point is the porous structure at $-2 \mu\text{m}$ in the FIB cross-section and on the top of the sample. A divertor manipulator will operate in the future operation phase of W7-X [89]. This manipulator will allow exposure of a test sample during helium GDC and ECWC discharges to perform a deep investigation regarding the assumption about porosity of the a:B/C-H layer.

These results show that in addition to the free B introduced with boronizations another mechanism plays a significant role to provide newly available B atoms: erosion and re-deposition (see Figure 5.10).

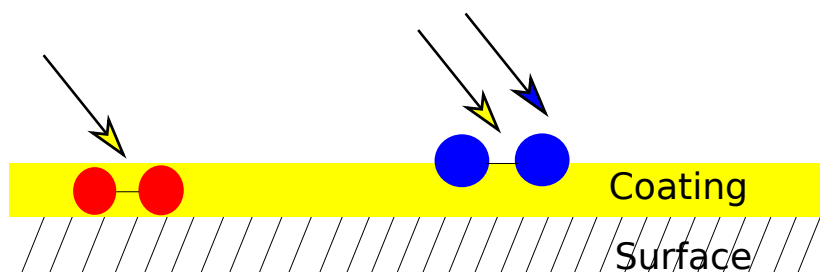


Figure 5.10: Boronization mechanism. The coating a-B/C:H layer is shown in yellow. Oxygen gettered due to the boronization is shown in red, while the blue color shows oxygen gettered due to re-deposition.

5.5 Difference of short and long-term boronizations effects

Both short and long-time effects of boronization study is needed to understand the mechanisms of impurity reduction and predict the necessity of further boronizations. The normalized influxes of B and C at the strike line are shown in Figure 5.11a. Apparently, B is quickly eroded there until a rather constant low level due to balance between its erosion and re-deposition. This happens after the first 59 s of plasma exposure time (15 discharges) after boronization. Simultaneously, C behaves in the same way. The ratio between C and B fluxes (Figure 5.11b) increases with every discharge and together with Figure 5.11a it shows quick erosion of B and increase of C levels. Oxygen behaviour is not shown here since its line radiation wasn't detectable with the overview spectrometer during the first discharges after boronization.

5. Effects of boronization

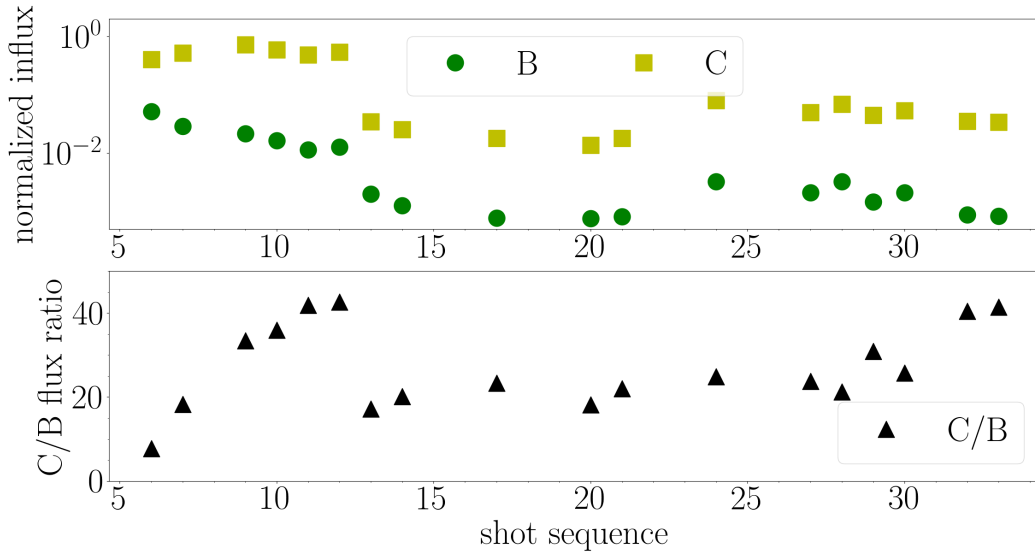


Figure 5.11: a) B and C normalized influx as a function of a discharge number on the first day after boronization. b) Ratio of C to B fluxes for the same operational day of W7-X. Standard magnetic configuration (Sereda et al. [2]).

The temporal evolution of B, C and O normalized influx at the divertor and their concentration in the main plasma over the complete experimental campaign are shown in Figure 5.12a and 5.12b correspondingly. Right after the first boronization O normalized influx at the divertor substantially decreased by a factor of 10. In contrast, the C yield dropped by a factor of 4. After 1000 s of plasma exposure time in different magnetic configurations O and C normalized influx didn't show a significant increase. In contrast, B eroded rather quickly at the strike line location and divertor. The average values obtained with the Langmuir probe were $T_e \approx 51$ eV and $n_e \approx 6.8 \cdot 10^{18} \text{ m}^{-3}$ for the discharges used in Figure 5.12a. With the second and the third boronizations O normalized influx at the divertor dropped even more up to a factor of 100. The reduction of the C emission with each subsequent boronization is not so pronounced.

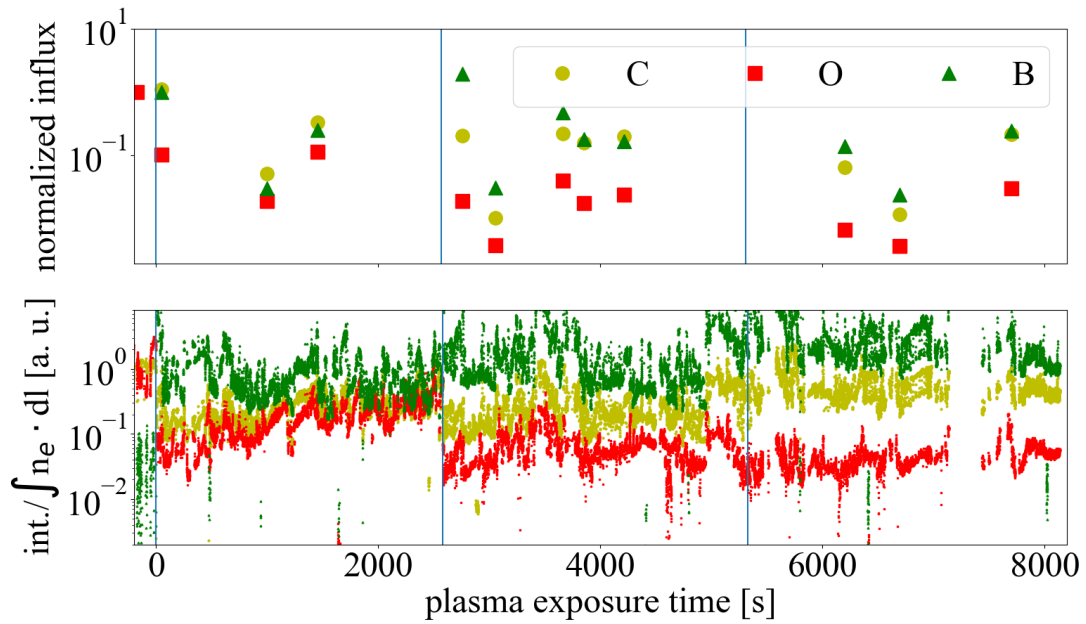


Figure 5.12: Time evolution of the main low Z impurities O and C as well as B: a) normalized influx, b) intensity of OVI, CVI and BV lines normalized to the line integrated density. The values are plotted as a function of the total plasma exposure time in all magnetic configurations normalized by the values before boronization. The vertical blue lines show boronization occurrences (Sereda et al. [2]).

Photon fluxes of CIII (465.4 nm) and OII (441.9 nm) lines at the stainless steel wall show qualitatively the same behaviour as shown in Figure 5.13. The conversion of photon fluxes to impurity fluxes is rather complicated in this case since no diagnostics are available at these locations to provide T_e and n_e .

The results of mass spectrometry complement the spectroscopic data showing that partial pressure of CO and CO₂ decreased by a factor of 8 and 12 correspondingly (Figure 5.14). A reduction in H₂O content was also recorded, approximately by a factor of 2. There was no change in CH₄ pressure in the outgassing phase immediately after the first boronization.

5. Effects of boronization

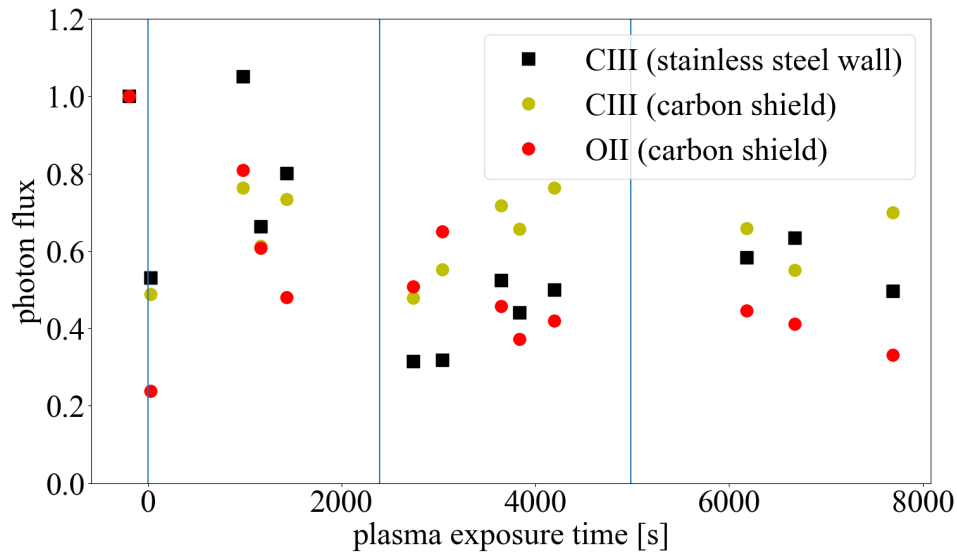


Figure 5.13: Time evolution of CIII (465.4 nm) and OII (441.9 nm) photon flux obtained with the filterscope system normalized to the values before boronization as a function of total plasma exposure time (Sereda et al. [2]).

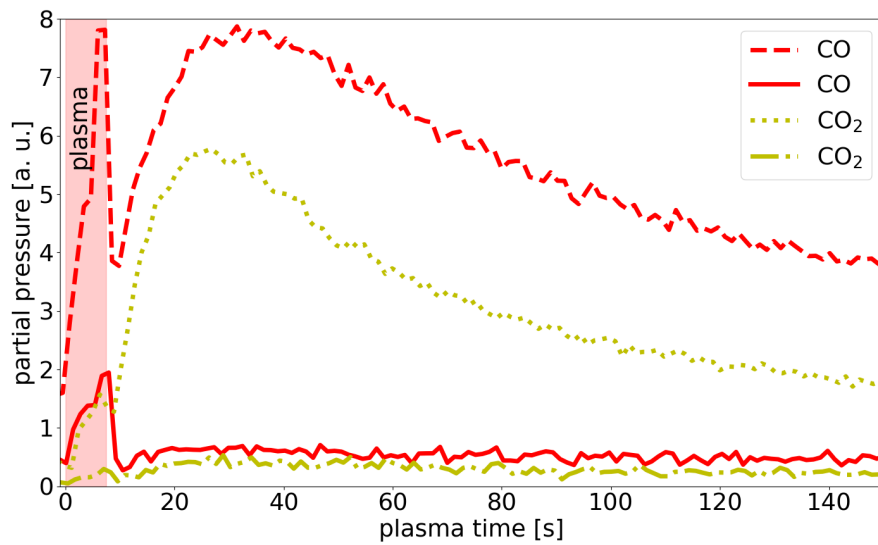


Figure 5.14: Mass spectrometry results for CO and CO₂ before (20180808.021, higher values) and after the first (20180807.011, lower values) boronization (Sereda et al. [2]).

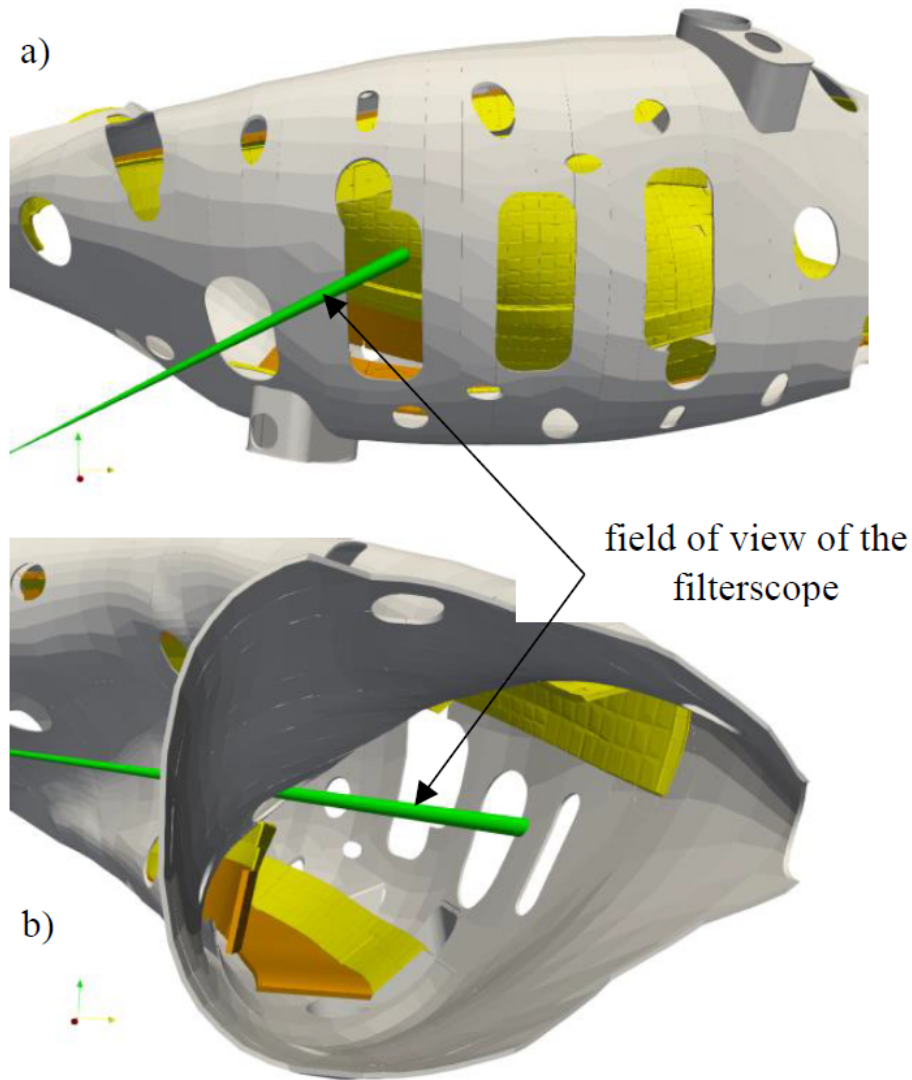


Figure 5.15: Field of view of the used line of sight of the filterscope system at: a) AEK10 port (toroidal angle $\phi = [-4.8^\circ, -10.1^\circ]$) looking at the carbon shield and at b) AEL30 port ($\phi = [126.5^\circ, 130.8^\circ]$) looking at the stainless steel wall (Sereda et al. [2]).

This implies that the main mechanism of C erosion before boronization was via formation of CO and CO₂ at the divertor. After the boronization O levels significantly dropped due to its gettering by B. The main zone of gettering is the recessed PFCs, since B is quickly eroded at the strike line location. Additional mechanisms such as reduced chemical erosion of C by H due to a:B/C-H layer play smaller role and could not be quantified due to undetectable radiation of corresponding molecular bands. With every subsequent boronization O levels were decreasing even further due to the appearance of new B layers and, therefore, free B atoms which getter O via oxides formation.

6

Summary, conclusions and outlook

The experimental campaign OP1.2 of the Wendelstein 7-X stellarator employing the test divertor unit has been successfully concluded. One of the major achievements was the device performance at the high plasma density reaching $1 \cdot 10^{20} \text{ m}^{-3}$ and the high diamagnetic energy $E_{dia} = 510 \text{ kJ}$ together with the low value of $Z_{eff} = 1.2$ for the dedicated set of reference discharges.

Such a high performance has become possible due to significantly reduced main low-Z impurities: oxygen and carbon. This reduction was caused by boronization - plasma-chemical deposition of a boron layer on all plasma-facing components, which has been fully characterized in this work.

In total three boronizations were applied during the OP1.2b experimental campaign. The most descriptive was the first boronization, after which the normalized influx of carbon was decreased by a factor of 4 and the normalized influx of oxygen was decreased by a factor of 10 as measured by the photon influx spectroscopy. The boronization layer was quickly eroded during the first 15 discharges after the first boronization, as suggested by the normalized influx of boron. Nevertheless, carbon and oxygen levels did not significantly increase between the boronizations. Moreover, the normalized influx of oxygen decreased with each subsequent boronization when newly introduced boron atoms were available to getter oxygen. This resulted in the reduction of the normalized influx of oxygen by a factor of 100 after the third boronization as compared to the values before boronization.

In addition to the photon influx spectroscopy performed at the strike line location the XUV spectra showed the same qualitative behaviour of boron, carbon and oxygen in the main plasma. The filterscope system data was used to describe photon fluxes of the CIII and OII lines coming from the graphite shield and only CIII photon flux coming from the stainless steel wall both following previous observation.

Mass spectrometry data was used to describe behaviour of the volatile species CO, CO₂, H₂O and CH₄. The partial pressure of CO and CO₂ dropped by a factor of 8 and 12 correspondingly. The partial pressure of H₂O dropped by a factor of 2. These spectra give additional evidence that the main mechanism of carbon erosion before the boronizations was due to its chemical erosion by oxygen with the formation of CO and CO₂ molecules.

After the experimental campaign a post-mortem analysis of a divertor tile at the re-deposition zone provided concentration profiles of boron, carbon, iron and oxygen.

6. Summary, conclusions and outlook

Both carbon and oxygen show 3 distinctive features on these profiles: 3 peaks for oxygen and 3 drops for carbon. These features are related to the 3 boronizations during OP1.2b and provide an additional evidence of the boronization mechanism by gettering of oxygen by boron. The boron profile contains 3 peaks, but only the last one is clearly stressed. A peak of iron was found at the position corresponding to the period before boronizations which was related to the He-GDC frequently performed before boronization, since due to its mass helium can effectively sputter iron which is then transported to the divertor target. The IR thermography showed an increase of the power flux density onto the divertor target at the strike-line location by $\approx 25\%$.

To enable studying of the boronization effects the AEJ51 endoscope system was used. During OP1.2b mainly the overview spectrometer system was used through the complete campaign. Before and after the campaign it was absolutely calibrated in the Torus hall of W7-X including the complete optical path.

A detailed spectral survey was performed by the overview spectroscopy at the edge plasma and the most suitable atomic and ionic lines have been found for the photon emission spectroscopy. These include spectra of H, B, C, O, N and Ne. Molecular bands of CH, CO, CO₂, BH and their ions could not be detected, possibly due to the not sufficient resolution of the overview spectrometer.

Development of tomographic reconstruction approach was continued and extended by He-beam injection simulations at the divertor plasma.

In the next experimental campaign the Wendelstein 7-X stellarator will be equipped with an actively cooled graphite divertor. For this experimental campaign all 4 endoscopes will be installed allowing tomographic reconstruction of the 2D emission profiles. In addition, the high resolution spectrometers with the rotatable fibre bundles will allow full observation of both vertical and horizontal divertor targets for molecular bands observation.

These extended capabilities will provide needed instrumentation to study the PSI processes and impurity influx into the plasma. Both challenges are important in the view of a long pulse operation of Wendelstein 7-X.

In the second part of the TDU campaign of W7-X different magnetic configurations of W7-X were used. This provided different locations of the strike line on the divertor target. In the standard magnetic configuration the total plasma exposure time was 4809 s, high-mirror 1392 s, low- ι 1180 s and high- ι 1673 s while discharges were switching between the configurations with the longest discharge of ≈ 100 s. Such a regime provided good conditions of erosion of the boron layer and its redeposition in other areas. In contrast, in the future experimental campaigns W7-X is aiming at discharges of up-to 1800 s length in one magnetic configuration. That will lead to quick erosion of the boron layer at the strike line and raises a question about the frequency of boronization application.

References

- [1] J. Winter et al. “Boronization in Textor”. In: *Journal of Nuclear Materials* 162-164 (1989), pp. 713–723. ISSN: 00223115. DOI: 10.1016/0022-3115(89)90352-8.
- [2] S. Sereda et al. “Impact of Boronizations on Impurity Sources and Performance in Wendelstein 7-X”. In: *Nuclear Fusion* 60.8 (2020), p. 086007. ISSN: 0029-5515, 1741-4326. DOI: 10.1088/1741-4326/ab937b.
- [3] O. Neubauer et al. “Endoscopes for Observation of Plasma-Wall Interactions in the Divertor of Wendelstein 7-X”. In: *Fusion Engineering and Design* 146 (2019), pp. 19–22. ISSN: 09203796. DOI: 10.1016/j.fusengdes.2018.11.009.
- [4] E. Wang et al. “Impurity Sources and Fluxes in W7-X: From the Plasma-Facing Components to the Edge Layer”. In: *Physica Scripta* T171 (2020), p. 014040. ISSN: 0031-8949, 1402-4896. DOI: 10.1088/1402-4896/ab4c04.
- [5] Y. Wei et al. “An Ultraviolet-Visible-near Infrared Overview Spectroscopy for Divertor Plasma Diagnosis on Wendelstein 7-X”. In: *AIP Advances* 8.8 (2018), p. 085011. ISSN: 2158-3226. DOI: 10.1063/1.5033371.
- [6] W. Biel. “Status and Outlook of Fusion Research”. In: *Schriften Des Forschungszentrums Jülich, Reihe Energie Und Umwelt, Energy and Environment* 298 (2015), pp. 432–441. URL: <https://juser.fz-juelich.de/record/283670> (visited on 03/23/2020).
- [7] J. D. Lawson. “Some Criteria for a Power Producing Thermonuclear Reactor”. In: *Proceedings of the Physical Society. Section B* 70.1 (1957), pp. 6–10. ISSN: 0370-1301. DOI: 10.1088/0370-1301/70/1/303.
- [8] A. J. Creely et al. “Overview of the SPARC Tokamak”. In: *Journal of Plasma Physics* 86.5 (2020). ISSN: 0022-3778, 1469-7807. DOI: 10.1017/S0022377820001257.
- [9] P. Rodriguez-Fernandez et al. “Predictions of Core Plasma Performance for the SPARC Tokamak”. In: *Journal of Plasma Physics* 86.5 (2020). ISSN: 0022-3778, 1469-7807. DOI: 10.1017/S0022377820001075.
- [10] A. Q. Kuang et al. “Divertor Heat Flux Challenge and Mitigation in SPARC”. In: *Journal of Plasma Physics* 86.5 (2020). ISSN: 0022-3778, 1469-7807. DOI: 10.1017/S0022377820001117.
- [11] *Magnetic Field in Tokamaks*. EUROfusion. URL: https://www.euro-fusion.org/fileadmin/user_upload/Archive/wp-content/uploads/2011/07/7c.jpg (visited on 01/28/2021).
- [12] P. C. Stangeby. “A Tutorial on Some Basic Aspects of Divertor Physics”. In: *Plasma Physics and Controlled Fusion* 42 (12B 2000), B271–B291. ISSN: 0741-3335. DOI: 10.1088/0741-3335/42/12B/321.

REFERENCES

- [13] T. Sunn Pedersen et al. “Confirmation of the Topology of the Wendelstein 7-X Magnetic Field to Better than 1:100,000”. In: *Nature Communications* 7.1 (2016). ISSN: 2041-1723. DOI: 10.1038/ncomms13493.
- [14] L. Spitzer. “The Stellarator Concept”. In: *The Physics of Fluids* 1 (1958), pp. 253–264. DOI: 10.1063/1.1705883.
- [15] P. Grigull et al. “Divertor Operation in Stellarators: Results from W7-AS and Implications for Future Devices”. In: *Fusion Engineering and Design* 66-68 (2003), pp. 49–58. ISSN: 09203796. DOI: 10.1016/S0920-3796(03)00121-2.
- [16] T. Klinger et al. “Overview of First Wendelstein 7-X High-Performance Operation”. In: *Nuclear Fusion* 59.11 (2019), p. 112004. ISSN: 0029-5515, 1741-4326. DOI: 10.1088/1741-4326/ab03a7.
- [17] B. Schweer et al. “Development of an ICRH Antenna System at W7-X for Plasma Heating and Wall Conditioning”. In: *Fusion Engineering and Design* 123 (2017), pp. 303–308. ISSN: 09203796. DOI: 10.1016/j.fusengdes.2017.05.019.
- [18] T. Stange et al. “Advanced Electron Cyclotron Heating and Current Drive Experiments on the Stellarator Wendelstein 7-X”. In: *EPJ Web of Conferences* 157 (2017). Ed. by J. Hillairet, p. 02008. ISSN: 2100-014X. DOI: 10.1051/epjconf/201715702008.
- [19] P. Stangeby. *The Plasma Boundary of Magnetic Fusion Devices*. Plasma Physics. Bristol and Philadelphia: Institute of Physics Pub., 2000. ISBN: 0 7503 0559 2.
- [20] W. Eckstein et al. *Sputtering Data - IPP 9/82 Report*. IPP 9/82. Max-Planck-Institut für Plasmaphysik, 1993, p. 352. URL: <http://hdl.handle.net/11858/00-001M-0000-0027-6326-2> (visited on 02/20/2020).
- [21] B. V. Mech, A. A. Haasz, and J. W. Davis. “Isotopic Effects in Hydrocarbon Formation Due to Low-Energy H⁺/D⁺ Impact on Graphite”. In: *Journal of Nuclear Materials* 255.2 (1998), pp. 153–164. DOI: 10.1016/S0022-3115(98)00035-X.
- [22] J. Winter. “Wall Conditioning in Fusion Devices and Its Influence on Plasma Performance”. In: *Plasma Physics and Controlled Fusion* 38.9 (1996), pp. 1503–1542. ISSN: 0741-3335, 1361-6587. DOI: 10.1088/0741-3335/38/9/001.
- [23] T. Wauters et al. “Wall Conditioning in Fusion Devices with Superconducting Coils”. In: *Plasma Physics and Controlled Fusion* 62.3 (2020), p. 034002. ISSN: 0741-3335, 1361-6587. DOI: 10.1088/1361-6587/ab5ad0.
- [24] A. Spring, R. Brakel, and H. Niedermeyer. “Wall Conditioning for Wendelstein 7-X by Glow Discharge”. In: *Fusion Engineering and Design* 66-68 (2003), pp. 371–375. ISSN: 09203796. DOI: 10.1016/S0920-3796(03)00245-X.
- [25] U. Schneider et al. “Boronization of ASDEX”. In: *Journal of Nuclear Materials* 176-177 (1990), pp. 350–356. ISSN: 00223115. DOI: 10.1016/0022-3115(90)90071-T.
- [26] E. Gauthier et al. “Boronization in Tore Supra”. In: *Journal of Nuclear Materials* 196-198 (1992), pp. 637–641. ISSN: 00223115. DOI: 10.1016/S0022-3115(06)80114-5.
- [27] T. Nakano et al. “Boronization Effects Using Deuterated-Decaborane (B10D14) in JT-60U”. In: *Journal of Nuclear Materials* 313-316 (2003), pp. 149–152. ISSN: 00223115. DOI: 10.1016/S0022-3115(02)01402-2.

- [28] G.L. Jackson et al. “Boronization in DIII-D”. In: *Journal of Nuclear Materials* 196-198 (1992), pp. 236–240. ISSN: 00223115. DOI: 10.1016/S0022-3115(06)80038-3.
- [29] C. Skinner et al. “Effect of Boronization on Ohmic Plasmas in NSTX”. In: *Nuclear Fusion* 42.3 (2002), pp. 329–334. DOI: 10.1088/0029-5515/42/3/313.
- [30] H.F. Dylla et al. “Effects of Boronization of the First Wall in TFTR”. In: *Journal of Nuclear Materials* 176-177 (1990), pp. 337–342. ISSN: 00223115. DOI: 10.1016/0022-3115(90)90069-Y.
- [31] A. Sykes et al. “First Results from MAST”. In: *Nuclear Fusion* 41.10 (2001), pp. 1423–1433. ISSN: 0029-5515. DOI: 10.1088/0029-5515/41/10/310.
- [32] M. Greenwald et al. “H Mode Confinement in Alcator C- Mod”. In: *Nuclear Fusion* 37.9 (1997), p. 793. DOI: 10.1088/0029-5515/37/6/I07.
- [33] Ch. Hollenstein et al. “Cold Boronization in TCA”. In: *Journal of Nuclear Materials* 176-177 (1990), p. 343. DOI: 10.1016/0022-3115(90)90070-4.
- [34] U. Schneider, J. Stadlbauer, and The W7-AS team. “Boronization on Wendelstein 7-AS”. In: *Proceedings of the 17th Symposium on Fusion Technology*. 17th Symposium on Fusion Technology. Vol. 1. Rome, Italy, 1992, p. 376. DOI: 10.1016/B978-0-444-89995-8.50068-0.
- [35] S. Shinohara et al. “First Results of Boronization in REPUTE-1 RFP”. In: *Journal of The Physical Society of Japan* 61.9 (1992), p. 3030. DOI: 10.1143/JPSJ.61.3030.
- [36] A. Refke et al. “Interaction of Energetic Oxygen with Different Boron/Carbon Materials”. In: *Journal of Nuclear Materials* 212-215 (1994), pp. 1255–1259. ISSN: 00223115. DOI: 10.1016/0022-3115(94)91031-6.
- [37] P. Wienhold et al. “Collection of Oxygen in the Scrape-off Layer Depending on Boron Conditioning of TEXTOR”. In: *Journal of Nuclear Materials* 196-198 (1992), pp. 647–652. ISSN: 00223115. DOI: 10.1016/S0022-3115(06)80116-9.
- [38] Y. Liang et al. “Diagnostic Set-up and Modelling for Investigation of Synergy between 3D Edge Physics and Plasma-Wall Interactions on Wendelstein 7-X”. In: *Nuclear Fusion* 57.6 (2017), p. 066049. ISSN: 0029-5515, 1741-4326. DOI: 10.1088/1741-4326/aa6cde.
- [39] P. Drews et al. “Edge Plasma Measurements on the OP 1.2a Divertor Plasmas at W7-X Using the Combined Probe”. In: *Nuclear Materials and Energy* 19 (2019), pp. 179–183. DOI: 10.1016/j.nme.2019.02.012.
- [40] D. Nicolai et al. “A Multi-Purpose Manipulator System for W7-X as User Facility for Plasma Edge Investigation”. In: *Fusion Engineering and Design* 123 (2017), pp. 960–964. ISSN: 09203796. DOI: 10.1016/j.fusengdes.2017.03.013.
- [41] O. Neubauer et al. “Optical Instruments For Local Divertor Observation At Wendelstein 7-X”. In: *Proceedings of 1st EPS Conference on Plasma Diagnostics — PoS (ECPD2015)*. 1st EPS Conference on Plasma Diagnostics. Frascati, Italy: Sissa Medialab, 2016, p. 113. DOI: 10.22323/1.240.0113.
- [42] S.A. Bozhenkov et al. “Service Oriented Architecture for Scientific Analysis at W7-X. An Example of a Field Line Tracer”. In: *Fusion Engineering and Design* 88.11 (2013), pp. 2997–3006. ISSN: 09203796. DOI: 10.1016/j.fusengdes.2013.07.003.
- [43] W. Demtröder. *Laser Spectroscopy*. 4th ed. Springer. ISBN: 978-3-540-73415-4.

REFERENCES

- [44] *AVT Technical Manual*. URL: <https://www.alliedvision.com/en/products/cameras/detail/Pike/F-145/action/pdf.html> (visited on 01/28/2021).
- [45] *Open Computer Vision Library*. URL: <https://opencv.org/> (visited on 01/28/2021).
- [46] *OpenCV: Camera Calibration*. URL: https://docs.opencv.org/2.4/modules/calib3d/doc/camera_calibration_and_3d_reconstruction.html (visited on 01/28/2021).
- [47] A. Daniels. *Field Guide to Infrared Systems, Detectors, and FPAs*. 3rd. 2018. URL: <https://doi.org/10.1117/3.2315935.ch85>.
- [48] F. van den Bergh. “MTF Mapper”. URL: <https://sourceforge.net/projects/mtfmapper/> (visited on 07/15/2020).
- [49] F. van den Bergh. “Deferred Slanted-Edge Analysis: A Unified Approach to Spatial Frequency Response Measurement on Distorted Images and Color Filter Array Subsets”. In: *Journal of the Optical Society of America A* 35.3 (2018), pp. 442–451. DOI: 10.1364/JOSAA.35.000442.
- [50] F. van den Bergh. “Robust Edge-Spread Function Construction Methods to Counter Poor Sample Spacing Uniformity in the Slanted-Edge Method”. In: *Journal of the Optical Society of America A* 36.7 (2019), p. 1126. ISSN: 1084-7529, 1520-8532. DOI: 10.1364/JOSAA.36.001126.
- [51] M. Clever. *Hydrogen Recycling and Transport in the Helical Divertor of TEXTOR*. Schriften Des Forschungszentrums Jülich, Reihe Energie & Umwelt 87. Jülich: Forschungszentrum Jülich, 2010. 172 pp. ISBN: 978-3-89336-673-6.
- [52] R. Laube et al. “Designs of Langmuir Probes for W7-X”. In: *Fusion Engineering and Design* 86.6-8 (2011), pp. 1133–1136. ISSN: 09203796. DOI: 10.1016/j.fusengdes.2010.12.059.
- [53] L. Rudischhauser et al. “The Langmuir Probe System in the Wendelstein 7-X Test Divertor”. In: *Review of Scientific Instruments* 91.6 (2020), p. 063505. ISSN: 0034-6748, 1089-7623. DOI: 10.1063/1.5143013.
- [54] *Wendelstein 7-X Logbook: TDU Probes*. URL: <https://wikis.ipp-hgw.mpg.de/W7X/index.php/File:TDULangmuirProbesLowRes.JPG> (visited on 02/15/2021).
- [55] P. Drews et al. “Edge Plasma Measurements on the OP 1.2a Divertor Plasmas at W7-X Using the Combined Probe”. In: *Nuclear Materials and Energy* 19 (2019), pp. 179–183. ISSN: 23521791. DOI: 10.1016/j.nme.2019.02.012.
- [56] L. Stephey et al. “Spectroscopic Imaging of Limiter Heat and Particle Fluxes and the Resulting Impurity Sources during Wendelstein 7-X Startup Plasmas”. In: *Review of Scientific Instruments* 87.11 (2016), p. 11D606. ISSN: 0034-6748, 1089-7623. DOI: 10.1063/1.4959274.
- [57] R. Colchin et al. “The Filterscope”. In: *Review of Scientific Instruments* 74.3 (2003), pp. 2068–2070. DOI: 10.1063/1.1537038.
- [58] N. H. Brooks et al. “Filterscopes: Spectral Line Monitors for Long-Pulse Plasma Devices”. In: *Review of Scientific Instruments* 79.10 (2008), 10F330. ISSN: 0034-6748, 1089-7623. DOI: 10.1063/1.2957777.

- [59] E. A. Unterberg et al. “HELIOS: A Helium Line-Ratio Spectral-Monitoring Diagnostic Used to Generate High Resolution Profiles near the Ion Cyclotron Resonant Heating Antenna on TEXTOR”. In: *Review of Scientific Instruments* 83.10 (2012), p. 10D722. ISSN: 0034-6748, 1089-7623. DOI: 10.1063/1.4739236.
- [60] *Wendelstein 7-X Internal Wiki: Filterscope*. URL: https://wikis.ipp-hgw.mpg.de/W7X/index.php/QSR02_-_ORNL_Filterscopes (visited on 01/29/2021).
- [61] W. Biel et al. “Design of a High-Efficiency Extreme Ultraviolet Overview Spectrometer System for Plasma Impurity Studies on the Stellarator Experiment Wendelstein 7-X”. In: *Review of Scientific Instruments* 75.10 (2004), pp. 3268–3275. ISSN: 0034-6748, 1089-7623. DOI: 10.1063/1.1784557.
- [62] J. Schacht et al. “The Implementation of the Wendelstein 7-X Control a Data Acquisition Concepts at VUV/XUV Overview Spectrometers HEXOS”. In: *Fusion Engineering and Design* 88.5 (2013), pp. 259–264. ISSN: 09203796. DOI: 10.1016/j.fusengdes.2012.05.015.
- [63] *Wendelstein 7- X Logbook: HEXOS*. URL: <https://w7x-logbook.ipp-hgw.mpg.de/components?id=QSD> (visited on 01/29/2021).
- [64] D. Zhang et al. “Design Criteria of the Bolometer Diagnostic for Steady-State Operation of the W7-X Stellarator”. In: *Review of Scientific Instruments* 81.10 (2010), 10E134. ISSN: 0034-6748, 1089-7623. DOI: 10.1063/1.3483194.
- [65] P. A. Bagryansky et al. “Dispersion Interferometer Based on a CO₂ Laser for TEXTOR and Burning Plasma Experiments”. In: *Review of Scientific Instruments* 77.5 (2006), p. 053501. ISSN: 0034-6748, 1089-7623. DOI: 10.1063/1.2202922.
- [66] K.J. Brunner et al. “Real-Time Dispersion Interferometry for Density Feedback in Fusion Devices”. In: *Journal of Instrumentation* 13.09 (2018), P09002. ISSN: 1748-0221. DOI: 10.1088/1748-0221/13/09/P09002.
- [67] *ADAS*. URL: <https://open.adas.ac.uk/> (visited on 01/28/2021).
- [68] W. Zholobenko et al. “Synthetic Helium Beam Diagnostic and Underlying Atomic Data”. In: *Nuclear Fusion* 58.12 (2018), p. 126006. ISSN: 0029-5515, 1741-4326. DOI: 10.1088/1741-4326/aadda9.
- [69] W. Zholobenko, M. Rack, and D. Reiter. *Development and Evaluation of a Synthetic Helium Beam Diagnostic for Wendelstein 7-X*. Technical Report Jül-4407. Jülich: Forschungszentrum Jülich, 2018, p. 73. URL: <http://hdl.handle.net/2128/17601> (visited on 08/23/2020).
- [70] S. Brezinsek et al. “Impact of Nitrogen Seeding on Carbon Erosion in the JET Divertor”. In: *Journal of Nuclear Materials* 417.1-3 (2011), pp. 624–628. ISSN: 00223115. DOI: 10.1016/j.jnucmat.2010.12.097.
- [71] S. Brezinsek et al. “Identification of Molecular Carbon Sources in the JET Divertor by Means of Emission Spectroscopy”. In: *Journal of Nuclear Materials* 337-339 (2005), pp. 1058–1063. ISSN: 00223115. DOI: 10.1016/j.jnucmat.2004.10.114.
- [72] R.W.B. Pearse and A.G. Gaydon. *The Identification of Molecular Spectra*. 4th ed. London, New York: Chapman and Hall, 1976. 397 pp. ISBN: 0 412 14350 X.
- [73] R. Prakash et al. *Spectroscopic Divertor Characterization and Impurity Influx Measurements in ASDEX Upgrade Tokamak*. 10/31. 2006, p. 37. URL: https://www.researchgate.net/publication/265149698_Spectroscopic_Divertor_Characterization_and_Impurity_Influx_Measurements_in_ASDEX_Upgrade_Tokamak.

REFERENCES

- [74] Y. Wei et al. “Spectroscopic Studies of Fuel Recycling and Impurity Behaviors in the Divertor Region of Wendelstein 7-X”. In: *Plasma Science and Technology* 21.10 (2019), p. 105102. ISSN: 1009-0630. DOI: 10.1088/2058-6272/ab273b.
- [75] D. Irajii et al. “Imaging of Turbulent Structures and Tomographic Reconstruction of TORPEX Plasma Emissivity”. In: *Physics of Plasmas* 17.12 (2010), p. 122304. ISSN: 1070-664X, 1089-7674. DOI: 10.1063/1.3523052.
- [76] A. Huber et al. “Tomographic Reconstruction of 2D Line Radiation Distribution in the JET MkIIIGB Divertor”. In: *Journal of Nuclear Materials* 313-316 (2003), pp. 925–930. ISSN: 00223115. DOI: 10.1016/S0022-3115(02)01478-2.
- [77] P. Denner. “Endoscope Diagnostic for Tomography, Spectroscopy and Thermography on Wendelstein 7-X”. DPG Spring Meeting (Hannover, Germany). Feb. 29, 2016.
- [78] U. Kruezi et al. “Supersonic Helium Beam Diagnostic for Fluctuation Measurements of Electron Temperature and Density at the Tokamak TEXTOR”. In: *Review of Scientific Instruments* 83.6 (2012), p. 065107. ISSN: 0034-6748, 1089-7623. DOI: 10.1063/1.4707150.
- [79] A. Gorjaev et al. “Wall Conditioning at the Wendelstein 7-X Stellarator Operating with a Graphite Divertor”. In: *Physica Scripta* T171 (2020), p. 014063. ISSN: 0031-8949, 1402-4896. DOI: 10.1088/1402-4896/ab60fa.
- [80] T. Wauters et al. “Ion and Electron Cyclotron Wall Conditioning in Stellarator and Tokamak Magnetic Field Configuration on WEGA”. In: RADIOFREQUENCY POWER IN PLASMAS: Proceedings of the 20th Topical Conference. Sorrento, Italy, 2014, pp. 187–190. DOI: 10.1063/1.4864519.
- [81] T. Wauters et al. “Wall Conditioning throughout the First Carbon Divertor Campaign on Wendelstein 7-X”. In: *Nuclear Materials and Energy* 17 (2018), pp. 235–241. ISSN: 23521791. DOI: 10.1016/j.nme.2018.11.004.
- [82] H.-S. Bosch et al. “Final Integration, Commissioning and Start of the Wendelstein 7-X Stellarator Operation”. In: *Nuclear Fusion* 57.11 (2017), p. 116015. ISSN: 0029-5515, 1741-4326. DOI: 10.1088/1741-4326/aa7cbb.
- [83] A. Gorjaev et al. “Development of Glow Discharge and Electron Cyclotron Resonance Heating Conditioning on W7-X”. In: *Nuclear Materials and Energy* 18 (2019), pp. 227–232. ISSN: 23521791. DOI: 10.1016/j.nme.2018.12.010.
- [84] T. Wauters et al. “Wall Conditioning by ECRH Discharges and He-GDC in the Limiter Phase of Wendelstein 7-X”. In: *Nuclear Fusion* 58.6 (2018), p. 066013. ISSN: 0029-5515, 1741-4326. DOI: 10.1088/1741-4326/aab2c9.
- [85] V. Moiseenko et al. “A Scenario of Pulsed Ecrh Wall Conditioning in Hydrogen for the Wendelstein 7-x Helias”. In: *Problems of Atomic Science and Technology* 119 (2019), pp. 37–40. URL: <http://hdl.handle.net/21.11116/0000-0003-91A6-D>.
- [86] G. Fuchert et al. “Increasing the Density in Wendelstein 7-X: Benefits and Limitations”. In: *Nuclear Fusion* 60.3 (2020), p. 036020. ISSN: 0029-5515, 1741-4326. DOI: 10.1088/1741-4326/ab6d40.
- [87] D. Zhang et al. “First Observation of a Stable Highly Dissipative Divertor Plasma Regime on the Wendelstein 7-X Stellarator”. In: *Physical Review Letters* 123.2 (2019), p. 025002. ISSN: 0031-9007, 1079-7114. DOI: 10.1103/PhysRevLett.123.025002. URL: <https://link.aps.org/doi/10.1103/PhysRevLett.123.025002> (visited on 02/28/2020).

- [88] T. Sunn Pedersen et al. “First Divertor Physics Studies in Wendelstein 7-X”. In: *Nuclear Fusion* 59.9 (2019), p. 096014. ISSN: 0029-5515, 1741-4326. DOI: 10.1088/1741-4326/ab280f.
- [89] M. Hubeny et al. “Diagnostic Setup for the Divertor Manipulator at Wendelstein 7-X”. In: *Nuclear Materials and Energy* 18 (2019), pp. 77–81. ISSN: 23521791. DOI: 10.1016/j.nme.2018.11.028.

Statutory declaration

I declare under oath that I have produced my thesis independently and without any undue assistance by third parties under consideration of the 'Principles for the Safeguarding of Good Scientific Practice at Heinrich Heine University Düsseldorf'.

Date/Place: _____ Signature: _____